Theses and Dissertations

August 2013

Growth of ZnO Thin Films on Polar Oxide Surfaces By Atomic Layer Deposition

Kallol Pradhan
University of Wisconsin-Milwaukee

Follow this and additional works at: https://dc.uwm.edu/etd

Part of the Materials Science and Engineering Commons, and the Physics Commons

GROWTH OF ZnO THIN FILMS ON POLAR OXIDE SURFACES BY

ATOMIC LAYER DEPOSITION

by

Kallol Pradhan

A Dissertation Submitted in

Partial Fulfillment of the

Requirements for the Degree of

Doctor of Philosophy

in Physics

at

The University of Wisconsin-Milwaukee

August 2013

ABSTRACT

GROWTH OF ZnO THIN FILMS ON POLAR OXIDE SURFACES BY
ATOMIC LAYER DEPSOITION

by

Kallol Pradhan

The University of Wisconsin-Milwaukee, 2013
Under the Supervision of Professor Paul F. Lyman

Polar heterointerfaces of MgO(111) and the II-VI semiconductor ZnO are of technological interest for transparent conducting electrode applications. Growth and structure of thin films on polar surfaces can be different than on non-polar surfaces due to the large surface energy of polar surfaces. We have grown ZnO on unreconstructed MgO(111)-(1x1)-OH terminated and reconstructed MgO(111)-($\sqrt{3}$x$\sqrt{3}$)R30° polar oxide surfaces using atomic layer deposition. A homemade UHV-interfaced viscous-flow atomic layer deposition (ALD) reactor with *in-situ* quartz crystal monitor was used to grow ZnO thin films on the MgO(111) substrates. Surface morphology studies revealed that the surface roughness increases with ZnO film thickness and that reconstructed MgO(111) is a better substrate for production of smooth ZnO films. Thin-film structural analysis revealed that ZnO thin films are polycrystalline, having the wurtzite structure, with preferential growth along the *c*-axis. ZnO grown on MgO(111)-($\sqrt{3}$x$\sqrt{3}$)R30°

substrates show strong preferential growth along the polar (002) direction. In contrast, growth along the non-polar (100) and (101) directions is also observed when grown on MgO(111)-(1x1) substrates. These observations indicate the crystal orientation during ALD ZnO growth depends not only on temperature but also on the surface terminations and symmetry of the substrates.

We also investigated the growth of ALD ZnO on polar 6H-SiC(0001) substrates and non-polar MgO(100), α-Al$_2$O$_3$(0001) and oxidized Si(100). Our study revealed that, for non-polar substrates, ALD ZnO grows along the non-polar (100) and (101) directions along with the polar (002) direction. Highly *c*-axis-oriented ALD ZnO thin film growth on 6H-SiC(0001) indicates that lattice matched substrates favor growth of high-quality ALD ZnO.

Finally, we investigated ZnO thin film growth on unreconstructed MgO(111)-(1x1)-OH terminated and reconstructed MgO(111)-($\sqrt{3}$x$\sqrt{3}$)R30° polar oxide surfaces using pulsed-laser deposition (PLD). Structural studies revealed that surface termination affects the PLD ZnO growth similar to the way it affected ALD ZnO growth.

TABLE OF CONTENTS

LIST OF FIGURES

LIST OF TABLES

ACKNOWLEDGEMENTS

Chapter 1

Introduction

This chapter outlines the organization of the dissertation. It also describes the motivation for the work undertaken in this dissertation, MgO(111) surface as a polar oxide surface, and a brief description of ZnO and its growth using different deposition methods.

1.1 Motivation

In recent years, there has been enormous interest in ZnO owing to its many superior properties as wide-bandgap semiconductor. With a room-temperature bandgap of ~3.37 eV and large exciton binding energy of 60 meV, this direct-gap material can be expected to form the basis of blue, violet, or UV optoelectronic devices [1-3]. Efforts have been made to grow high-quality ZnO thin films using different growth techniques, viz., molecular beam epitaxy (MBE), pulsed-laser deposition (PLD), metal-organic chemical vapor deposition (MOCVD), sputtering, and atomic layer deposition (ALD). However, producing high-quality ZnO thin films over large substrates uniformly in industry is still very challenging. ZnO, and α-Al$_2$O$_3$ single crystals are commonly used as substrates for epitaxial ZnO growth. However, substrates having a large lattice mismatch exhibit poor crystalline quality in the deposited ZnO thin films. MgO(111) is often used as a buffer layer to produce epitaxial ZnO [4]. However, the fundamental growth mechanism is not fully understood.

The ZnO/MgO interface is also important, as alloying ZnO with MgO can be used to modify the bandgap of the material. In some cases, the bandgap can be tailored by depositing a quasi-alloy material made up of multilayers of ZnO and MgO. This kind of interface is widely used in fabrication of light-emitting diodes (LED) [5].

Polar heterointerfaces of MgO(111) and the II-VI semiconductor ZnO are of technological interest for transparent conducting electrode applications. Growth and structure of thin films on polar surfaces can be different than on non-polar surfaces due to the large surface energy of polar surfaces. In this work, we have grown ZnO on

unreconstructed MgO(111)-(1x1)-OH terminated and reconstructed MgO(111)-(√3x√3)R30° polar oxide surfaces using atomic layer deposition. Growth of ZnO using atomic layer deposition on nonpolar surfaces, viz., MgO(001), α-Al$_2$O$_3$(0001), and a polar 6H-SiC(0001) surface is also investigated. Finally the growth of ZnO on unreconstructed MgO(111)-(1x1)-OH terminated and reconstructed MgO(111)-(√3x√3)R30° polar oxide surfaces using pulsed-laser deposition is examined.

1.2 ZnO

ZnO is II-VI wideband gap semiconductor that commonly occurs in the hexagonal wurtzite crystal structure, where each anion is surrounded by four cations at the corners of the tetrahedron. However, it can also exist in cubic zinc blende and rocksalt crystal structures. A phase change from wurtzite to rocksalt is observed upon pressure above 8 GPa [6]. Figure 1.1 shows the wurtzite structure of ZnO.
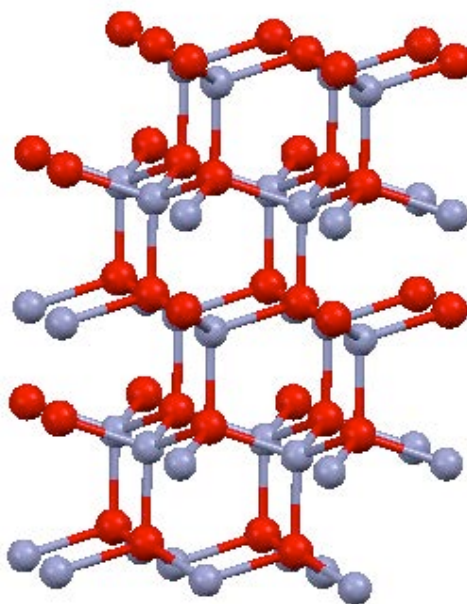
Figure 1.1 Wurtzite hexagonal crystal structure of ZnO. The red balls represent oxygen atoms and the violet balls represent zinc atoms.

ZnO wurtzite structure belongs to P6$_3$mc space group. If cleaved along the *c*-plane it produces the polar (0001) plane.

ZnO has a bandgap of around 3.27 eV and exciton binding energy ~ 60 meV. Due to its large exciton binding energy compared to GaN (~25 meV), it has the potential to replace GaN in optoelectronic applications. One of the other advantages of ZnO over GaN is that large-area ZnO single crystals are readily available. However, it is still very challenging to grow high-quality epitaxial ZnO thin films over different substrates.

The ZnO wurtzite structure has low symmetry and large electromechanical coupling. This results in large piezoelectric constants for ZnO. Large piezoelectric constants are favorable for actuator, transducer, and sensor applications. Polycrystalline ZnO has strong non-linear resistance, making it useful for varistor applications. The non-linear resistance is often attributed to a Schottky barrier formed on grain boundaries of the ZnO grains [7, 8].

Most of the ZnO applications in transparent conductors, piezoelectric devices, and varistors use polycrystalline films on glass substrates. However, single-crystal epitaxial films with low defect density are required for high-performance devices. PLD, MOCVD, and MBE are used frequently to meet these requirements.

In PLD, sapphire has been the most popular choice of substrates, because of the availability of low-cost wafers. Using PLD, Kaidashev and his co-workers were able to produce high-mobility epitaxial ZnO using *c*-plane sapphire [9]. Si, InP, CaF$_2$, and GaAs

are the other commonly used crystalline substrates for ZnO in PLD. However, most of them have a large lattice mismatch with ZnO. The ZnO films grown on them have large grain size separated by grain boundaries [8].

For epitaxial ZnO MBE growth sapphire, GaN, $LiTaO_3$, and MgO are popular choice of substrates. However, most of the growth has been undertaken on sapphire substrates due to its low cost. Although MBE ZnO grown on sapphire has shown promising electrical and optical properties, the crystal quality still need to be improved [3].

The metal-organic chemical vapor deposition (MOCVD) has been preferable choice of industry for production of high quality ZnO over large area substrates and high volume production. Si, GaAs, InP, GaP, Ge, and ZnO substrates were used to grow good quality ZnO using MOCVD. Gorla and his coworkers were able to produce epitaxial ZnO over *r*-plane sapphire [10]. However, most of the cases the MOCVD-grown ZnO exhibit poor surface morphology that is undesirable for light-emitting diode (LED) applications [11].

Recently atomic layer deposition (ALD) has been used to grow high quality ZnO, motivated by the low possible growth temperature, large-area uniformity and capability of producing sharp interfaces. However, ALD ZnO growth is mostly performed over amorphous substrates. ZnO films grown using ALD are mostly polycrystalline. Recently *c*- plane sapphire has been used to grow epitaxial ZnO [12]. To our knowledge, no one has attempted to grow epitaxial ZnO using ALD on polar MgO(111) substrates until now.

1.3 MgO(111) as a polar oxide surface

Oxide surfaces play an important role in catalysis, electronics, corrosion, friction, and lubrication processes. When these oxide crystals are cleaved along certain crystallographic directions, they can produce polar oxide surfaces. In recent years, the polar surfaces of compound semiconductors have been studied extensively. For the growth of III-V and II-VI devices, polar substrates (viz. (100) and (111) surfaces of GaAs and ZnS) are often used [13].

According to classical electrostatic criteria, oxide surfaces are classified into three types, shown in Figure 1.2. Type I surfaces have zero net charge on their individual surface layers and zero dipole moment in their repeat units normal to the surface. Type II surfaces do not have zero charge distribution in their individual surface layers but have zero dipole moment in their repeat unit. Because of the zero dipole moment, these surfaces are stable. Type III or polar surfaces have net charge and non-vanishing dipole moment perpendicular to the surface.
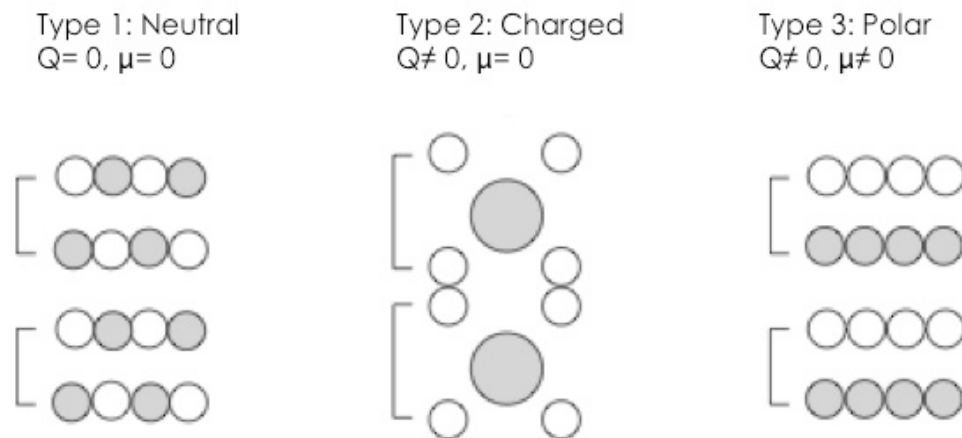
Figure 1.2 Classification of oxide surfaces according to Tasker (From [14]).

Type III polar surfaces have a large surface energy due to these non-vanishing dipole moments throughout all the repeat units of the crystal. Therefore, the polar surfaces are highly unstable. The polar surfaces can stabilize using either of three means, viz., surface reconstruction, adsorption of foreign species, and modification of surface electronic states.

MgO has the rocksalt structure, and, along the (111) direction, alternating layers of Mg^{2+} and O^{2-} ions make the MgO(111) surface a polar surface. Figure 1.3 (b) shows such a surface.

[Caption on next page.]
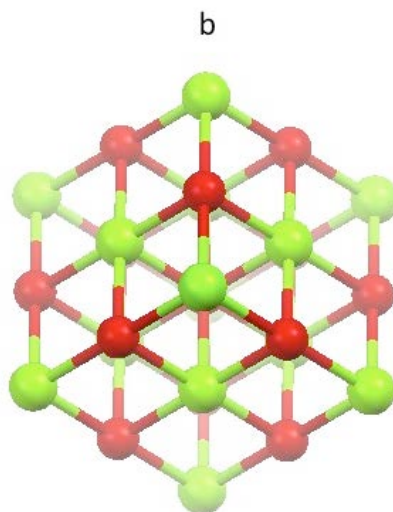
Figure 1.3 (a) MgO bulk unit cell with rock salt structure (b) Top view of MgO(111) bulk.

Three types of surface reconstruction are known for MgO(111) surfaces, viz., ($\sqrt{3}$x$\sqrt{3}$)R30°, p(2x2), and (2$\sqrt{3}$x2$\sqrt{3}$)R30° [15-17]. Gajdardziska-Josifovska and her co-workers have studied the structure of MgO(111)-($\sqrt{3}$x$\sqrt{3}$)R30° reconstructed surface in detail [18]. According to them, the reconstructed surface phase consists of oxygen trimers as building blocks just above the Mg atoms. Recently, Subramanian and co-workers have proposed another model for the MgO(111)-($\sqrt{3}$x$\sqrt{3}$)R30° reconstructed surface. According to them, it is non-stoichiometric, oxygen-rich surface with Mg terminaion and having 2/3 ML Mg vacancies [19].

In contrast, unreconstructed MgO can be stabilized only by adsorption of charged species. There has been evidence of hydroxyl-induced stabilization of MgO(111)-(1x1) surfaces from experiments [20-21].

Our recent surface x-ray diffraction experiment data have suggested that MgO(111)-($\sqrt{3}$x$\sqrt{3}$)R30° might have terminating layer with wurtzite structure. This surface symmetry might foster epitaxial ZnO growth on reconstructed MgO(111) surfaces. On the other hand, OH-terminated MgO(111)-(1x1) surface may serve as a better template for ALD ZnO growth, by minimizing the initial incubation period.

1.4 Organization of Dissertation

- Chapter 2 covers the experimental techniques used to characterize the ZnO thin films grown on polar and non-polar substrates.

- Chapter 3 describes the atomic layer deposition (ALD) techniques in detail. It also discusses the construction of the UHV-interfaced viscous-flow ALD reactor.

- Chapter 4 presents the experimental results of growth of ALD ZnO thin films on polar reconstructed MgO(111)-($\sqrt{3}$x$\sqrt{3}$)R30° and unreconstructed MgO(111)-(1x1) surfaces.

- Chapter 5 presents the experimental results of growth of ALD ZnO thin films on non-polar MgO(100), α-Al$_2$O$_3$(0001), and oxidized Si(100) surfaces. Growth of ALD ZnO on polar SiC(0001) surfaces is also discussed.

- Chapter 6 discusses the growth of ZnO thin films using pulsed-laser deposition (PLD) on polar reconstructed MgO(111)-($\sqrt{3}$x$\sqrt{3}$)R30° and unreconstructed MgO(111)-(1x1) surfaces.

- Chapter 7 has conclusions and outlook of future work.

1.5 References

1. D. M. Bagnall, Y. F. Chen, Z. Zhu, T. Yao, M. Y. Shen, and T. Goto, Appl. Phys. Lett.7**3,** 1038 (1998).

2. T. Gruber, C. Kirchner, R. Kling, F. Reuss, and A. Waag, Appl. Phys. Lett. **84**, 5359 (2004).

3. U. Ozgur, Y. I. Alivov, C. Liu, A. Teke, M. A. Reshchikov, S. Dogan, V. Avrutin, S. J. Cho, H. Morkoc, J. Appl. Phys. **98**, 041301 (2005).

4. M. W. Cho, A. Setiawan, H. J. Ko, S. K. Hong, and T. Yao, Semicond. Sci. Technol. **20**, S13 (2005).

5. J. W. Sun, Y. M. Lu, Y. C. Lui, D. Z. Shen, Z. Z. Zhang, B. H. Li, J. Y. Zhang, B. Yao, and X. W. Fan, J. Phys. D: Appl. Phys. **40**, 6541 (2007).

6. J. Serrano, A. H. Romero, F. J. Manjo´n, R. Lauck, M. Cardona, and A. Rubio, Phys. Rev. B **69**, 094306 (2004).

7. M. A. Alim, S. Li, F. Liu, and P. Cheng, Phys. Stat. Sol. **203**, 410 (2006).

8. A. Janotti, and C. G. Van de Walle, Rep. Prog. Phys. **72**, 126501 (2009).

9. E. M. Kaidashev, M. Lorenz, H. von Wenckstern, A. Rahm, H. C. Semmelhack, K. H. Han, G. Benndorf, C. Bundesmann, H. Hochmuth, and M. Grundmann, Appl. Phys. Lett. **82**, 3901 (2003).

10. C. R. Gorla, N. W. Emanetoglu, S. Liang, W. E. Mayo, Y. Lu, M. Wraback, and H. Shen, Appl. Phys. Lett. **85**, 2595 (1999).

11. Y. S. Choi, D. K. Hwang, B. J. Kwon, J. W. Kang, Y. H. Cho, and S. J. Park, Jpn. J. Appl. Phys. **50**, 105502 (2011).

12. C. S. Ku, H. Y Lee, J. M Huang, C. M. Lin, Mater. Chem. Phys. **120**, 236 (2010).

13. C. Noguera, J. Phys.: Condens. Matter **12**, R367 (2000).

14. P. W. Tasker, J. Phys. C: Solid State Phys. **12**, 4977 (1979).

15. G. W. Watson, E. T. Kelsey, N. H. Leeuw, D. J. Harris, and S. C. Parker, J. Chem. Soc. Faraday Trans. 2 **92,** 433 (1996).

16. A. Pojani, F. Finocchi, J. Goniakowski, and C. Noguera, Surf. Sci. **387,** 354 (1997). D. Wolf, Solid State Ionics. **75,** 3 (1995).

17. M. Gajdardziska-Josifovska, R. Plass, M. A. Schofield, D. R. Giese, and R. Sharma, J. Electron Microsc. **51,** S13 (2002).

18. R. Plass, K. Egan, C. Collazo-Davila, D. Grozea, E. Landree, L. D. Marks, and M. Gajdardziska-Josifovska, Phys. Rev. Lett. **81,** 4891 (1998).

19. A. Subramanian, L. D. Marks, O. Warschkow, and D. E. Ellis, Phys. Rev. Lett. **92,** 026101 (2004).

20. V. K. Lazarov, R. Plass, H. C. Poon, D. K. Saldin, M. Weinert, S. A. Chambers and M. Gajdardziska-Josifovska, Phy. Rev. B **71**, 115434 (2005).

21. H. C. Poon, X. F. Hu, S. E. Chamberlin, D. K. Saldin, and C. J. Hirschmugl. Surf. Sci. **600,** 2505 (2006).

Chapter 2

Experimental Techniques

Abstract

This chapter outlines the theory of various surface science techniques, including low energy electron diffraction (LEED) and x-ray photoelectron spectroscopy (XPS), along with different thin film characterization techniques such as atomic force microscopy (AFM) and x-ray diffraction (XRD). A brief theory behind the quartz crystal microbalance (QCM) used to monitor *in-situ* ALD thin film growth is also discussed. This chapter also discusses the theory of UV-Visible spectroscopy technique used to characterize the optical properties of the ALD-grown thin film transparent conducting oxide.

2.1 Ultra High Vacuum System

In order to study surfaces, most cases require an ultra-high vacuum (UHV) environment. An UHV environment keeps the surfaces clean and allow us to perform most surface analysis techniques like low energy electron diffraction (LEED), reflection high energy electron diffraction (RHEED), x-ray photoelectron spectroscopy (XPS) and Auger electron spectroscopy (AES). These surface techniques either use electrons as a probe or collect electrons emitted from the surface as a result of probing the surface with photons. UHV conditions helps to increase the electron mean free path length significantly, so that electrons emitted from the surfaces can travel to the detector without undergoing any scattering with the residual air molecules present in the vacuum chamber.

We used a commercially available ESCALab Mark II UHV system made by VG Scientific Ltd. for preparing the substrates and performing LEED before thin films were grown on them. The UHV system was pumped by two liquid-nitrogen-cooled diffusion pumps and an ion pump. The diffusion pumps were backed with oil-sealed rotary vane pumps. The base pressure was kept $\sim 1 \times 10^{-10}$ torr. The UHV chamber consists of a sample preparation chamber and an analysis chamber. The sample preparation chamber is equipped with a LEED system and a resistive heating stage for annealing the substrates. The analysis chamber is equipped with a twin anode x-ray source for XPS, a hemispherical analyzer, an ion gun for sputtering, and a resistive heating stage. Ar^{2+} ions generated by the ion gun (Phi 04-161) were used to sputter the substrates to produce

clean surfaces. A schematic of the ESCALab Mark II UHV system is shown in Figure 2.1.
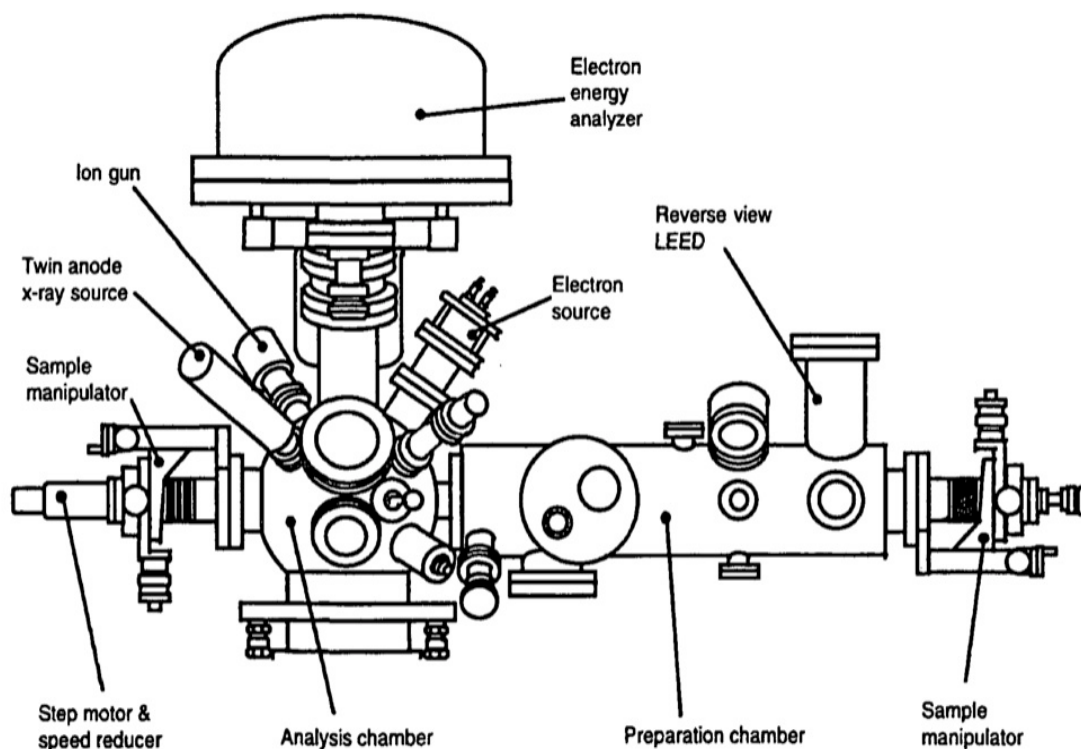
Figure 2.1 Schematic of ESCALab Mark II UHV system (adapted from Ref. [1]).

2.2 X-ray Diffraction

X-ray diffraction (XRD) is an efficient nondestructive analytic technique to identify the crystalline phase and preferred orientations of the films [2,3,4]. In XRD, the crystals are bombarded with monochromatic X-rays with wavelength ($\sim$ 1-10 Å) in the order of interatomic spacing of the atoms. The incoming X-ray photons interact with the electron

densities of the atoms and are scattered in all directions. These scattered X-rays interfere with each other constructively or destructively upon reaching the detector, depending on the phase differences of all the X-rays scattered by the different atoms of the crystal lattice. These interference patterns give information on the atomic structure of the crystals. In Figure 2.2 such an elastic scattering process is shown.
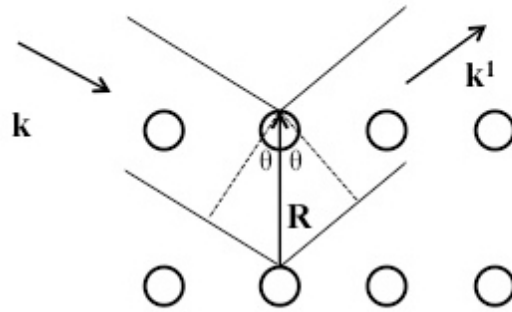
Figure 2.2 Reflections of X-rays from two planes of atoms in a solid.

In Figure 2.2 an incoming X-ray with wave vector k is incident on a crystal lattice with lattice vector R. The lattice vector R is given by,

$$R = n_1 a + n_2 b + n_3 c \qquad\qquad 2.1$$

where (n_1, n_2, n_3) are integers, and (a, b, c) are the basis vectors of the crystal. Upon incidence, the X-ray is scattered with wave vector k^1. Now the wave vector is proportional to the momentum p of the X-ray photon of wavelength λ :

$$k = |k| = 2\pi / \lambda = p / \hbar . \qquad\qquad 2.2$$

In order to have a constructive interference, the scattered waves from two layers of atoms must be in phase or the path difference must be an integer multiple of the wavelength. Thus we get Bragg's Law of diffraction,

$$2R\sin\theta = n\lambda \qquad \text{2.3}$$

where n is any integer. Bragg's Law can also be written in terms of the wave vector as

$$\boldsymbol{R} \bullet \Delta\boldsymbol{k} = 2\pi n \text{ ,} \qquad \text{2.4}$$

where $\Delta\boldsymbol{k} = \boldsymbol{k} - \boldsymbol{k}^1$. $\qquad \text{2.5}$

If **G** is a reciprocal lattice vector, then it can be shown that the constructive interference will only occur when

$$\boldsymbol{G} = \Delta\boldsymbol{k} \text{ .} \qquad \text{2.6}$$

The reciprocal lattice vector is given by

$$\boldsymbol{G} = h\boldsymbol{a}^* + k\boldsymbol{b}^* + l\boldsymbol{c}^* \qquad \text{2.7}$$

where ($\mathbf{a}^*$, $\mathbf{b}^*$, $\mathbf{c}^*$) are the reciprocal basis vectors and h, k, and l are integers. However the intensity and the shape of the X-ray peaks are related to the position of the atoms and how they are arranged inside the crystal.

Most of our X-ray measurements were performed on a SCINTAG 2000 diffractometer in θ-2θ mode. Figure 2.3 represents such an experimental setup. The X-rays are generated in the X-ray vacuum tube by impinging the accelerated electron to a solid metal target (Cu, Mo, or Co). These electrons knock out the corelevel electrons of

the target metal, and, in a decay process, X-rays are emitted. Many of these are K_α and K_β emissions. These X-rays are then collimated through slits and sent to the sample. Once they are diffracted from the sample, the X-rays are collected through a collecting slit at an angle 2θ, where 2θ is the angle between the diffracted and undiffracted X-ray. Finally the X-ray photons are counted in the detector to get the XRD pattern.
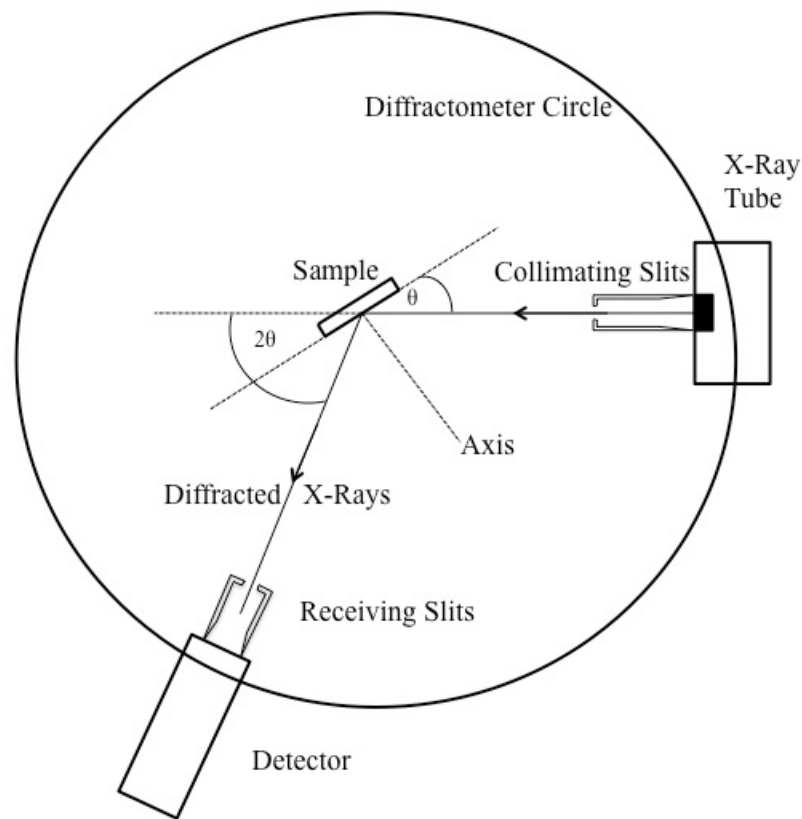
Figure 2.3 Schematic of experimental set-up for XRD measurement.

Other than identifying the crystal phase, XRD can be also be used to find the average crystallite size, stress and strain of thin films. The average crystallite size D of

thin films can be estimated using the Scherrer equation (equation 2.8) from XRD if the crystallite size is not more than 0.1 μm [5] :

$$D = \frac{k\lambda}{B\cos\theta} \; ,$$
2.8

where D = crystallite size in the direction perpendicular to the lattice planes, $k = 0.93$ = Scherrer's constant, λ = wavelength of X-ray

B = full width half maximum (FWHM) in radians, and θ = Bragg angle for the reflection under consideration.

While finding the value of B during crystallite size estimation, it has been corrected for instrumental broadening by assuming the measured FWHM resulted from the sum in quadrature of the intrinsic width B and the instrumental resolution of 1.75 mrad.

2.3 Low Energy Electron Diffraction

Low-energy electron diffraction (LEED) is one of the most important techniques for studying the atomic structure of the crystalline surfaces [6,7,8,9,10]. In LEED, low-energy (20 to 500 eV) electrons are directed normally on the crystal surface. The electrons are scattered back elastically and non-elastically from the well-ordered crystal surface.
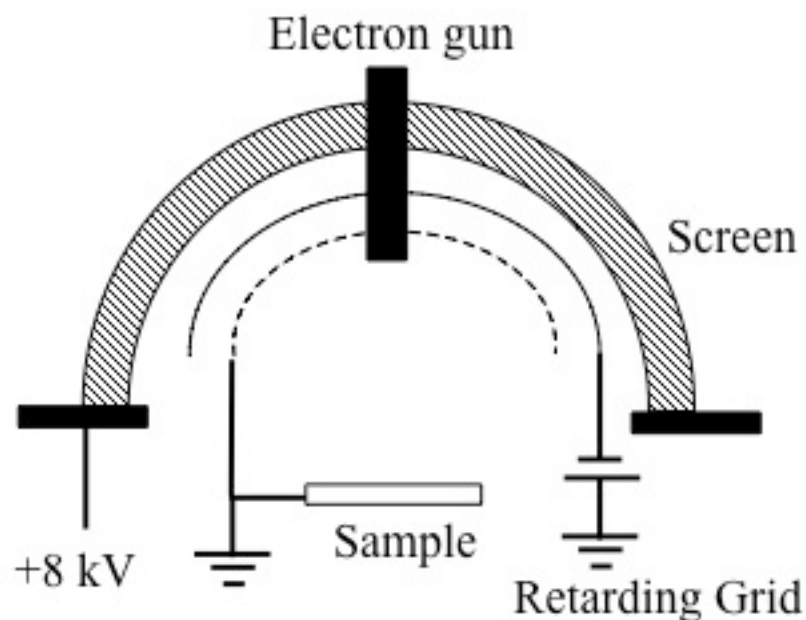
Figure 2.4 Schematic of LEED optics.

A typical LEED experimental set-up is shown in the Figure 2.4. It consists of an electron gun, sample, retarding grid and a hemispherical fluorescent screen. The whole setup is kept in an UHV chamber of pressure of the order of ~10^{10} Torr. The UHV condition allows us to study the clean surface at an atomic level for long time. The electron gun produces a narrow beam of electrons with variable energy. Diffracted beams of electrons, having the same energy as the incident beam, are produced in the backward direction. Apart from these elastically scattered electrons (~ 2-5%), secondary and inelastically scattered electrons (~ 95-98 %) are also produced by the sample. A retarding grid is used to reject these inelastically scattered electrons, allowing only the elastically scattered electrons to pass through. The elastically scattered electrons are accelerated to hit a fluorescent screen, and bright spots appear on the glass window showing the diffraction

pattern. Such a LEED diffraction pattern of a ZnO (000$\bar{1}$) surface is shown in Figure 2.5. The LEED pattern clearly exhibits the hexagonal symmetry of the ZnO Wurtzite structure.
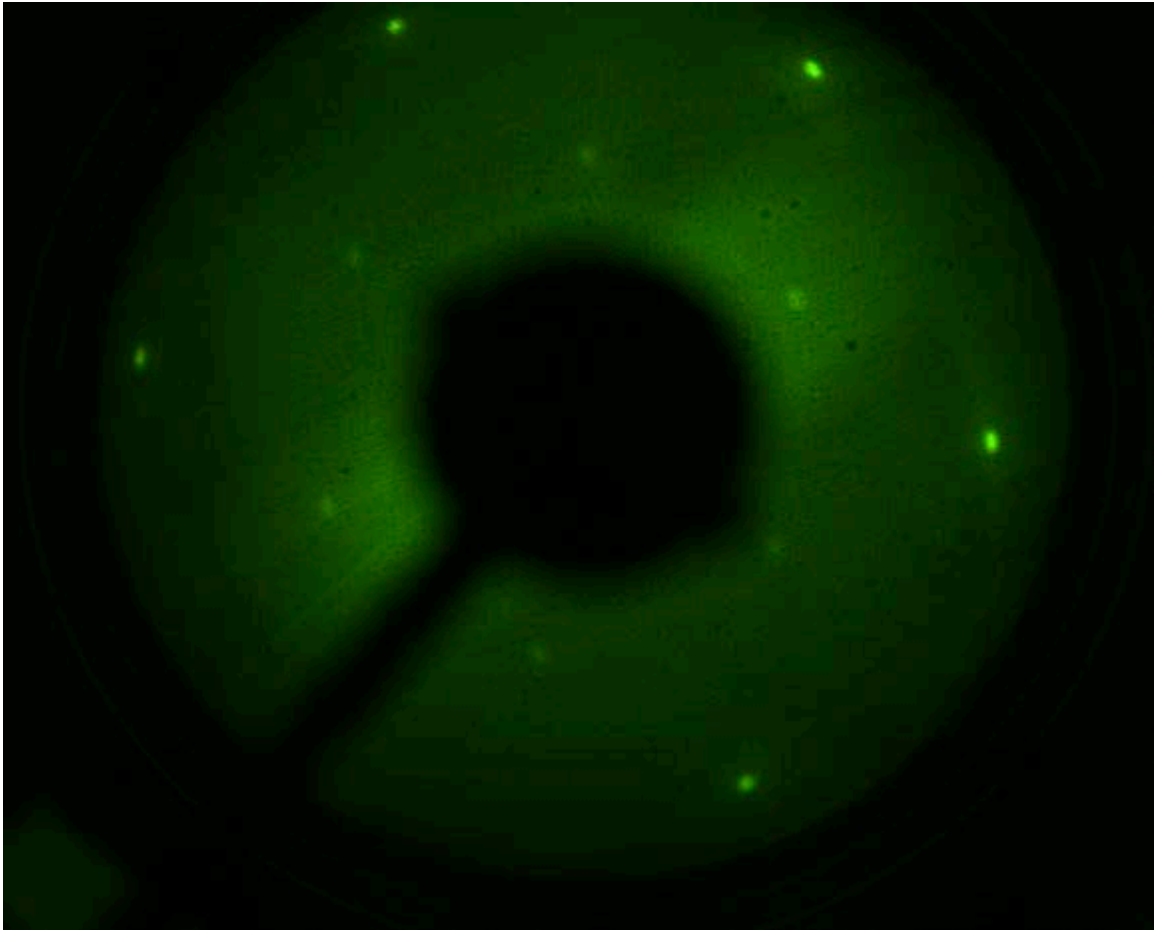
Figure 2.5 LEED pattern of ZnO (000$\bar{1}$) surface at 50 eV.

In order to diffract the electrons elastically from the crystal surface, the electrons should have the same order of wavelength as the lattice constant of the material. The wavelengths of the electrons are given by, the de Broglie's relation [11]

$$\lambda = h / p , \qquad\qquad 2.9$$

where λ is the de Broglie wavelength for the electron, h is Planck's constant, and p is the electron momentum. The momentum is given by

$$p = \sqrt{2mE_K} = \sqrt{2meV}$$
2.10

where m = mass of the electron, E_K = kinetic energy of the electron, e = charge of the electron and V = accelerating potential of the electron.

For example, an electron with energy 20 eV will have the de Broglie wavelength $\sim$ 2.7 Å.

The low energy electrons used in LEED have inelastic mean free path of the order of few atomic layers. This makes the LEED technique extremely surface sensitive.

In order to understand the LEED pattern, one needs to understand the diffraction condition. In two dimensions, Bragg's Law can be written from Equation 2.4,

$$\boldsymbol{a} \cdot \Delta \boldsymbol{k} = 2\pi n \quad , \quad \boldsymbol{b} \cdot \Delta \boldsymbol{k} = 2\pi m$$
2.11

where m and n are any integers and k is the normally incident wave vector on the crystal surface and k^I is the scattered wave vector. The diffraction condition given by Equation 2.11 is only satisfied if the k^I touches the crystal truncation rods. This can be found by constructing the Ewald sphere in reciprocal space. Such an Ewald sphere construction is shown in Figure 2.6. The radius of the Ewald sphere must be equal to the magnitude of incident wave vector to ensure elastic scattering. Whenever the Ewald sphere cuts the crystal truncation rod, the diffraction condition is satisfied and a bright spot is formed. Thus the LEED pattern is the image of reciprocal lattice of the ordered surface.
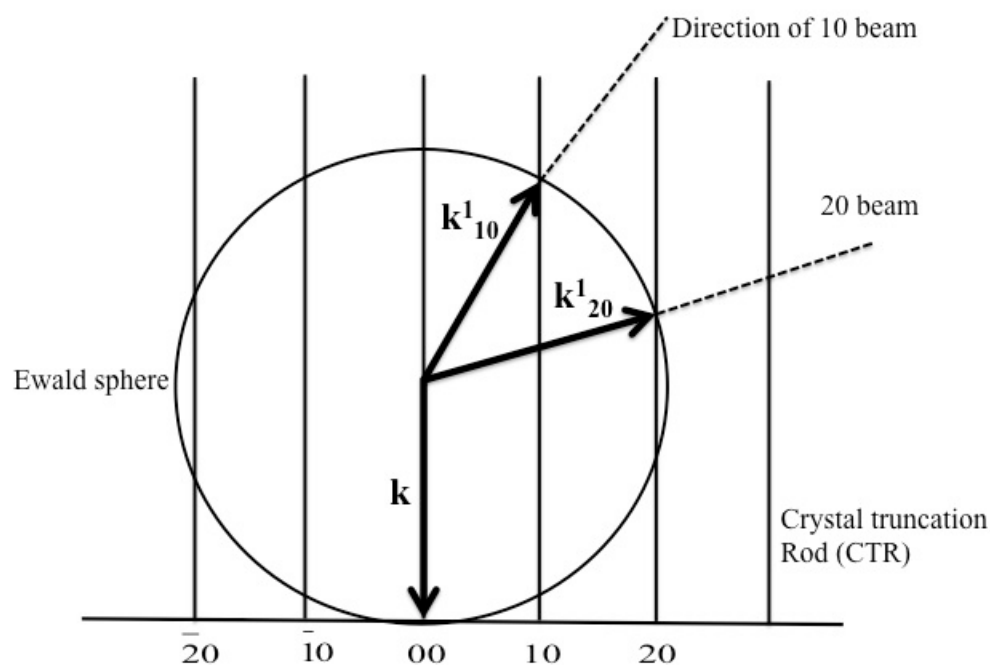
Figure 2.6 Ewald construction for a diffraction from a two dimensional structure for case of normal incidence.

2.4 X-ray photoelectron Spectroscopy

When an X-ray with proper energy is irradiated on a surface of a material, the atoms absorb the X-ray photon energy $\hbar\omega$ completely and photoelectrons are generated. In X-ray photoelectron spectroscopy (XPS), the kinetic energy of the photoelectrons is measured [12,13]. The kinetic energy of the photoelectrons that escape the sample without losing energy is related to the binding energies of the sample atoms, allowing us to identify which elements are present on the surface.
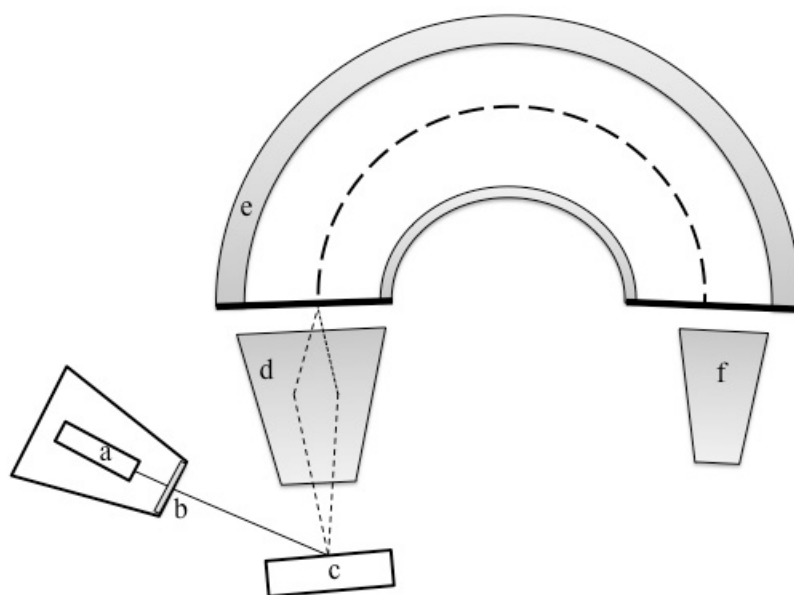
Figure 2.7 Schematic of XPS system. (a) X-ray source (b) Al window (c) sample (d) electron focusing optics (e) concentric hemispherical analyzer (f) channeltron.

A schematic picture of XPS system is shown in Figure 2.7. A XPS experimental setup consists of an X-ray source, electron optics, an energy analyzer and electron detector. A concentric hemispherical energy analyzer was used in this XPS study. Generally in X-ray photoelectron spectroscopy, X-ray photons from an Al K$_\alpha$ or Mg K$_\alpha$ source is used. The core-shell electrons of the sample absorb these X-ray photons and photoelectrons are liberated in the process of photoemission. Emitted photoelectrons are then focused using the electron optics and sent to the energy analyzer. The hemispherical energy analyzer selects a window of kinetic energies and allows the electrons only with these kinetic

energies to pass [14]. Finally the electrons are collected by the channeltron, which counts the number of electrons. A schematic of a photoemission process of an electron from kth level is represented in Figure 2.8. From energy conservation, the kinetic energy of the emitted electron and the incident energy of the primary X-ray photons are related according to:

$$\hbar\omega + E_{tot}^{i} = E_{kin} + E_{tot}^{f}(k) ,$$

2.12

where $\hbar\omega$ = energy of incident photon, E_{tot}^{i} = total energy of the initial state, $E_{tot}^{f}(k)$ = total final energy of the system after ejection of electron from kth level and E_{kin} = kinetic energy of the photoelectron.

The contribution from the recoil energy has been neglected in equation 2.12. If $E_B(k)$ is the binding energy of the photoelectron in the kth level referenced to the local vacuum level, then $E_B(k)$ is defined as

$$E_B(k) = E_{tot}^{f}(k) - E_{tot}^{i} .$$

2.13

From Equation 2.12 and 2.13 we get the photoelectric equation

$$\hbar\omega = E_{kin} + E_B(k) .$$

2.14
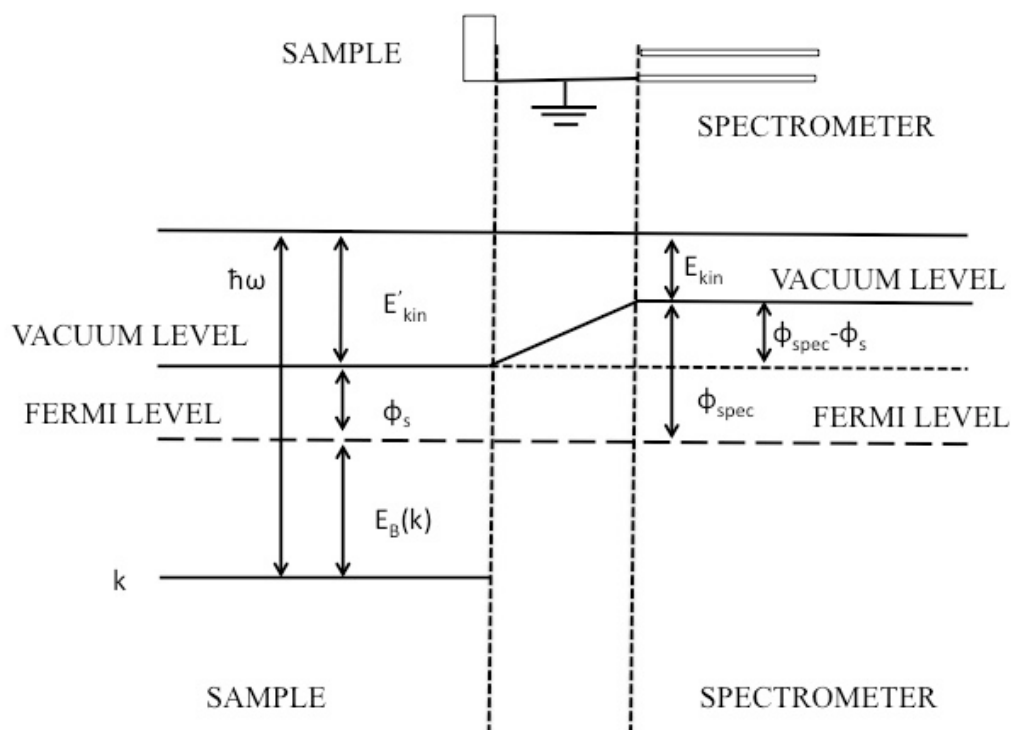
Figure 2.8 Schematic of the relevant energy levels for binding energy measurements in XPS. For a conducting sample, the sample and the spectrometer housing are in electrical contact and thus have same Fermi level of energy.

In the case of a solid sample, an electrical connection is made between the spectrometer and the sample. As both the sample and the spectrometer are in thermodynamic equilibrium, they have same Fermi energy (shown in Figure 2.8). If E'_{kin} is the kinetic energy of the electron at sample surface and E_{kin} is the kinetic energy measured inside the spectrometer analyzer, then E_{kin} is given by

$$E_{kin} = E'_{kin} + (\phi_s - \phi_{spec}) \,, \qquad\qquad 2.15$$

where ϕ_s = sample work function and $\phi_{spec\_}$ = spectrometer work function.

If the binding energy is measured relative to the Fermi level, the photoelectric equation is modified into

$$\hbar\omega = E_{kin} + E_B(k) + \phi_{spec} .$$

<div align="right">2.16</div>

From Equation 2.16 we can clearly see that only binding energies lower than X-ray photon (1486.6 eV for AL K$_\alpha$ and 12.53.6 eV for Mg K$_\alpha$) energies can be examined.

Each elements has its own characteristic XPS spectrum. Such an XPS survey spectrum of Cu has been shown in Figure 2.9. In the spectrum, a number of peaks appear over the background. The background originates from the electrons that lose energy while traveling from the emitted atom to the surface of the sample. The peaks can be grouped into two types. The first type originates from the photoemission of an electron and the second type originates from the X-ray-excited Auger emission. In Figure 2.8, the peaks originating from the emission of photoelectrons from core levels 2*s*, 2*p*$_{1/2}$, 2*p*$_{3/2}$, 3*s*, 3*p*$_{1/2}$, 3*p*$_{3/2}$ and 3*d* can be clearly seen. Auger LMM transition lines are also clearly visible in the range corresponding (on this graph) to binding energies of 560- 580 eV.
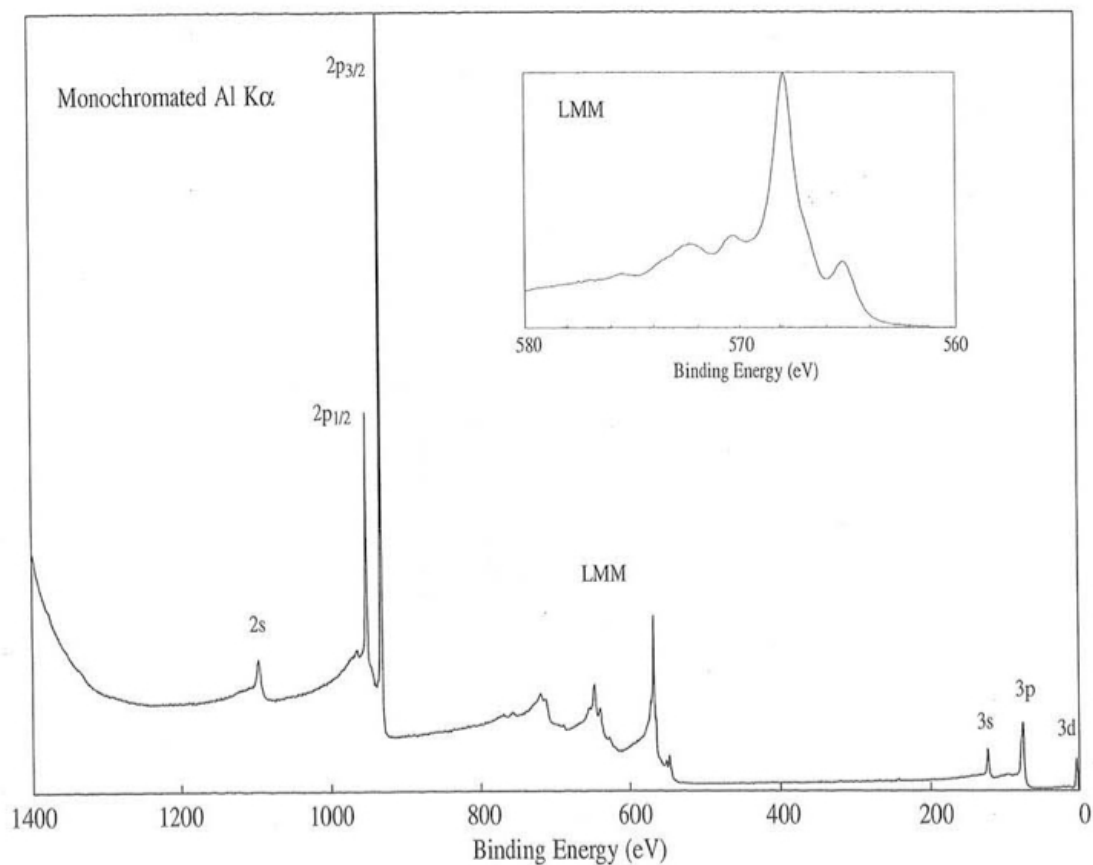
Figure 2.9 The XPS spectrum of a Cu surface excited by Al K_α X-rays (From Ref. [15].)

Photoelectrons and Auger electrons can only travel, on average, a distance called attenuation length λ before they are inelastically scattered. A depth *d*, called escape depth from which the XPS photoelectrons are emitted is given by

$$d = \lambda(E)cos\theta .$$

2.17

where θ is the angle of emission of photoelectrons from the surface normal. The attenuation length λ depends on the emitted electron's kinetic energy. Such dependence is

shown in Figure 2.10. In general the λ is on the order of 1-10 atomic layers. This makes XPS a surface-sensitive technique.
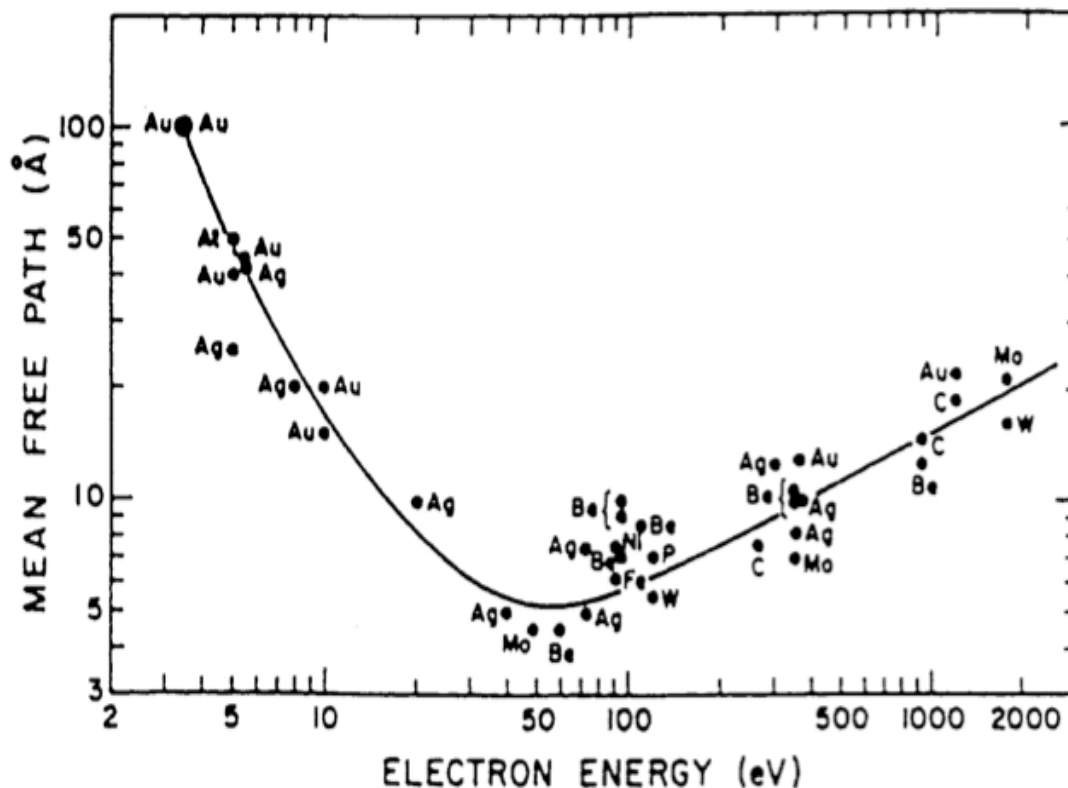
Figure 2.10 A compilation of experimentally determined attenuation length data. The solid line is a parametric fit to give the 'universal curve' of Seah and Dench (1997) (From [16].)

Apart from chemical identification of elements on the surface, XPS is very useful in determining the relative concentrations of the various constituents. This is done by measuring the area of each XPS peak of the different elements detected. For a

homogenous sample, the number of photoelectron (I) per second in a XPS peak is given by

$$I = nf\sigma\theta\lambda yAT \; , \qquad\qquad 2.18$$

where n = number of atoms of the element per unit volume, f = x-ray flux, σ = photoelectric cross section of the atomic orbital of interest, θ = angular efficiency factor of the instrument, y = the efficiency in photoelectric process for formation of photoelectrons, λ = mean free path of the photoelectron in the sample, A = area of the sample from which the photoelectrons are detected and T = detection efficiency for electrons emitted from the sample.

From Equation 2.18 we get

$$n = I / (f\sigma\theta\lambda yAT) \; . \qquad\qquad 2.19$$

The denominator of Equation 2.19 can be represented as S, which is the atomic sensitivity factor. Thus from a strong XPS spectral peak of two different elements, we get

$$\frac{n_1}{n_2} = \frac{\left(\dfrac{I_1}{S_1}\right)}{\left(\dfrac{I_2}{S_2}\right)} \; . \qquad\qquad 2.20$$

From Equation 2.20 we can find the atomic fraction C of any constituent in a sample as

$$C_x = \frac{n_x}{\sum_i n_i} = \frac{I_x / S_x}{\sum_i I_i / S_i} \; . \qquad\qquad 2.21$$

XPS can not only identify and quantify the constituent elements of the sample, but it also allows us to obtain information about their chemical states. The core level XPS peaks will show a shift in binding energies called a chemical shift, depending on the chemical environment of the emitting element. The capability of measuring the chemical states is the reason for which XPS is also known as electron spectroscopy for chemical analysis or ESCA [17, 18].

2.5 Ultraviolet-Visible Spectroscopy

In ultraviolet –visible spectroscopy one measures the absorption spectrum of a solution or solid in near-ultraviolet and visible light. In the case of thin films, the optical constants, viz., the absorption co-efficient and bandgap of the material, can be determined from the absorption or transmission spectrum. Upon shining this UV-visible light on thin films, an electronic transition from valence band to conduction band occurs. Thin films of a semiconductor only absorb light if the incident photons have energy equal to or greater than the bandgap. As a result, the absorption spectra of semiconductor thin films are characterized by a sudden sharp increase in absorption at the bandgap energy.

In the high-absorption region, the absorption co-efficient for direct-bandgap semiconductors varies as,

$$\alpha(\omega) \propto \frac{\sqrt{(\hbar\omega - E_g)}}{\hbar\omega} \, , \qquad\qquad 2.22$$

where $\alpha\ (\omega)$ = the absorption co-efficient of the material at incident wave frequency ω, and E_g = the bandgap of the material [19, 20].

In contrast, the absorption co-efficient for indirect bandgap semiconductors is given by

$$\alpha(\omega) \propto \frac{(\hbar\omega - E_g)^2}{\hbar\omega} \ . \qquad\qquad 2.23$$

The absorption co-efficient $\alpha\ (\omega)$ is determined mainly from scattering losses and fundamental absorption. Near to the bandgap the fundamental absorption is more prominent than the scattering loss. This allows us to write the absorption coefficient as

$$\alpha = \left[\frac{1}{d}\ln(\frac{1}{T})\right] , \qquad\qquad 2.24$$

where d = the thickness of the semiconductor films and T = normalized transmittance of the film [21].

From Equations 2.23 and 2.24 we get

$$\left[\frac{\text{-}\hbar\omega\ln(T)}{d}\right]^2 = K(\hbar\omega - E_g) , \qquad\qquad 2.25$$

where K is a constant. Now if we plot photon energy $\hbar\omega$ over $[\text{-}\hbar\omega ln(T)/d]^2$, we can obtain a Tauc plot [22]. Upon fitting the graph to straight line, we can estimate the bandgap of the thin film material.

Figure 2.11 shows a typical experimental setup for UV-Visible spectroscopy.
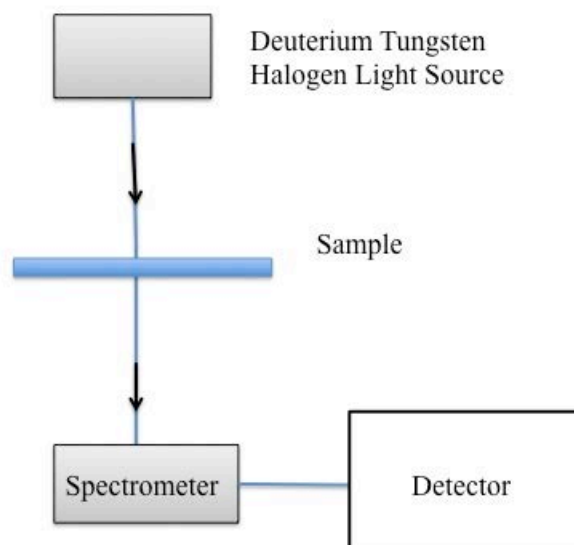
Figure 2.11 Schematic of the experimental setup for UV-Visible spectroscopy.

The UV-Visible spectrometer consists of source, sample, spectrometer and detector. The light source can emit light of wavelength 200-1100 nm. After passing through the sample, the transmitted light is passed through a spectrometer, which disperses the light onto the photodiode detector.

For our experiments we have used an Ocean Optics UBS400 fiber optics spectrometer. Once the spectrum is obtained, it was analyzed using Spectra Suite Spectroscopy software. Figure 2.12 shows such a transmission spectrum for a MgO sample.
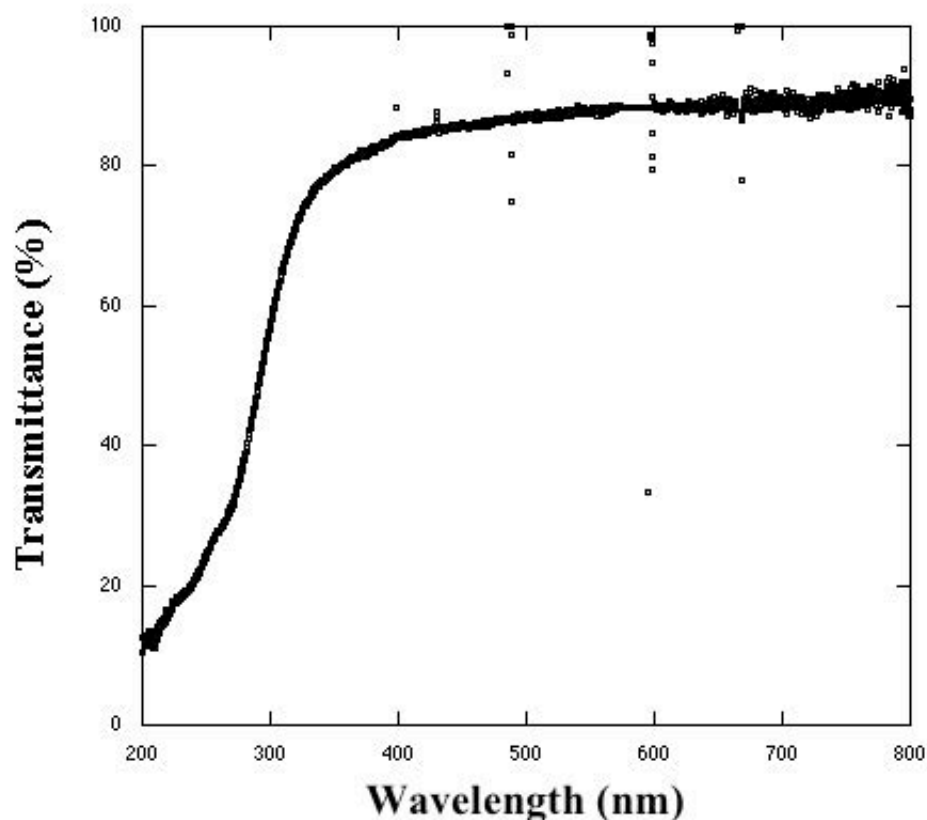
Figure 2.12 Transmission spectrum of MgO substrates.

2.6 Atomic Force Microscopy (AFM)

Atomic force microscopy (AFM) is a powerful technique that allows us to image the surface morphology with atomic-scale resolution. AFM not only allows us to image surface topology but it can also be used to measure average grain size and surface roughness. Unlike scanning tunneling microscopy (STM), it does not require an UHV environment and conducting sample to image the surface. Almost no surface preparation is required for AFM. AFM can also be used in a liquid environment. This attribute of

AFM makes it suitable for imaging soft biomaterials. Instead of measuring the tunneling current, the AFM measures the force between the cantilevered tip and the surface to produce very high-resolution three-dimensional images. In the x-y direction the resolution is ~ 1 to 0.1 nm. In the z direction the resolution can be as low as ~ 0.01 nm.

To image the surface, AFM uses a very sharp cantilever (~50-100 μm) with low spring constant (~ 0.001 to 5 nN/nm), typically made of Si, SiO_2, SiN or SiC. At the end of the cantilever there is a sharp tip (~ 15 μm tip height and ~ 5 nm tip radius). These tips can also be coated with aluminum or gold for conductive-AFM. Metal tips like Ni are also used for studying tribology.

This cantilever moves back and forth over the surface to be imaged. A laser light is constantly reflected from the cantilever to a position sensitive photodiode to monitor the movements of the cantilever tip. A piezoelectric motor is used in a feedback loop to keep the distance between the cantilever tip and surface constant as it scans over the surfaces by raising or lowering the cantilever. The movement of the cantilever tip is then converted into an image of the surface morphology. A typical AFM experimental set-up is shown in Figure 2.13. The resonant frequency of the cantilevers is ~ 100 kHz. External vibrations (~20 Hz) have very small effect (~ 10^{-3} nm in displacements) on the image formation.

The AFM tip interacts with the surfaces through van der Waals force. Depending on how far the AFM tip is from the sample surface, the AFM tip can experience attractive (distance ~ 10 to 90 Å) or repulsive forces (distance < 1 Å). Various scanning modes operate in different regions of the van der Waals force vs. distance curve as shown in Figure 2.14 [23]. There are three general types of AFM imaging modes present, viz.

contact mode, tapping mode, and non-contact mode. The contact mode is classified as a static mode, while the tapping and non-contact modes are classified as dynamic modes.

Contact mode is the most common type of scanning mode. Contact mode is generally useful for obtaining topological information of nanostructures and surfaces with hard surfaces. In contact mode the apex of the tip is in direct contact with the sample surface. The elastic force created due to the bending of the cantilever counterbalances the force acting between the atoms of the tip and surface. The contact mode can be carried out in two different configurations viz. constant height or constant force. In constant-height configuration, the cantilever is kept at a fixed height from the average surface, thus the defection reflects the surface topography. The main advantage of this configuration is, for smooth surfaces, a very high-resolution image can be obtained. However this configuration is not suitable
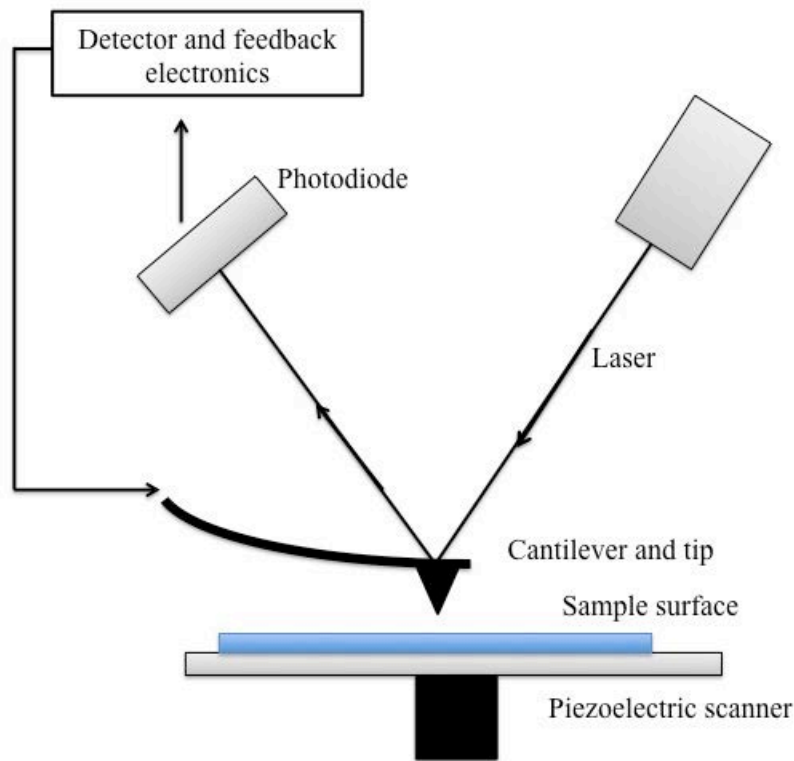
Figure 2.13 Schematic of an AFM imaging setup.

for soft biological samples; as biological samples are delicate, the vertical and shear force can damage the sample or change the shape of the sample.

For the constant-force configuration, the feedback system provides a constant value of cantilever bending. Thus the defection of the cantilever is maintained at a constant value. Change in topography produces a change in deflection. Then the feedback loop changes the applied voltage of the scanner in order to keep the deflection constant. Thus the change in the voltage maps the surface topography. This constant-force scanning mode has the
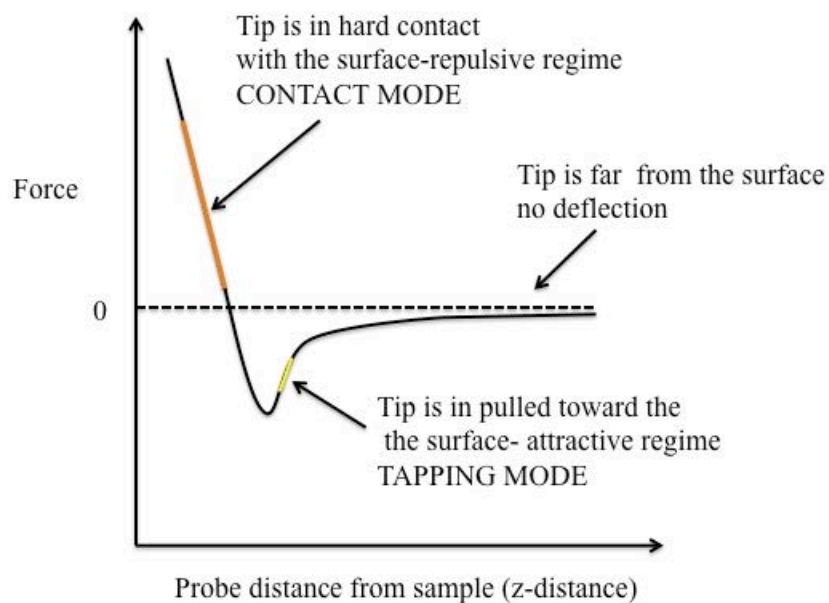
Figure 2.14 Plot of Van der Waals force as function of probe-sample separation (Adapted from Ref [23].)

same disadvantages as the constant-height scanning mode. However other surface characteristics like friction can also be mapped along with the surface topography.

Unlike contact mode, tips make only intermittent contact in tapping mode. In non-contact and tapping mode, the cantilever oscillates near its resonance frequency. The oscillation is excited by a piezo-element attached to the cantilever. The amplitude of the oscillation ranges from 100 to 200 nm. When the tip approaches the surface, the van der

Waals force and dipole-dipole interaction damps the amplitude of the oscillation. The oscillation amplitude is kept at a set point by adjusting the height of the AFM tip by the piezo-electric devices through a feed back control. Thus the height image is obtained from the position of the AFM tip during the scanning.

A typical AFM image (1 μm × 1 μm) of ZnO thin films on a MgO substrate, taken in contact mode using SiC tip, is shown in Figure 2.14.
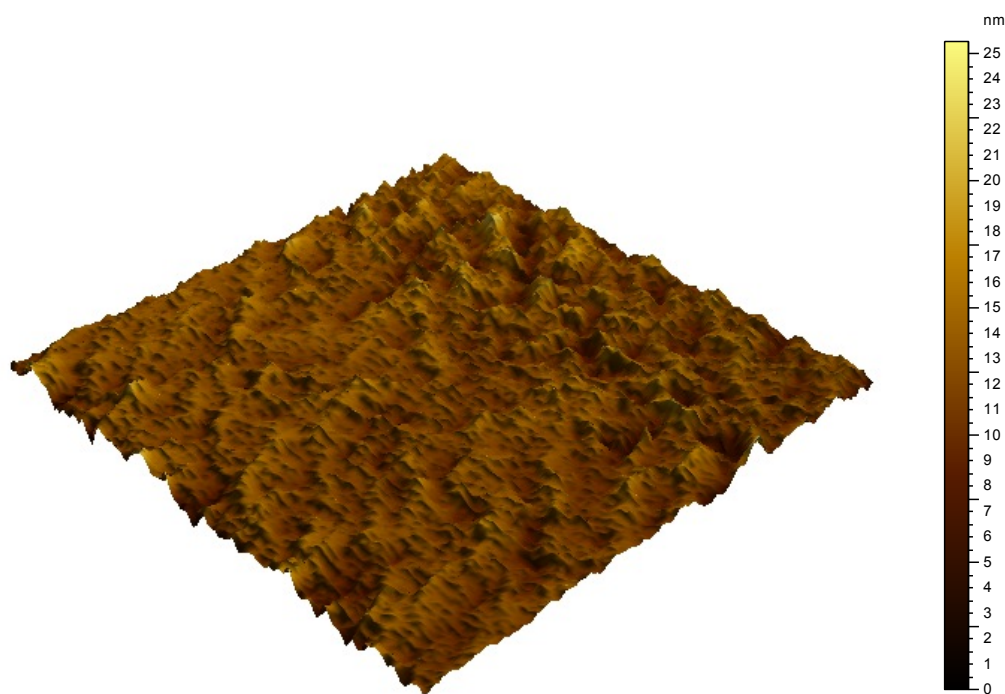
Figure 2.14 AFM image of ZnO thin films on a MgO substrate.

AFM measurements were taken using an Agilent 5420 scanning probe microscope and SiC AFM tip in contact mode (constant-force configuration). Using the AFM scans, surface morphology of the ZnO thin films grown at various conditions were examined.

The roughness of the surfaces may also be calculated from the AFM scans. Root-mean-square (RMS) roughness was calculated on (1 μm $\times$ 1 μm) scans after second-order flattening. RMS roughness value was defined as:

$$RMS = \sqrt{\frac{\sum\limits_{i=1}^{N}(z_i - z_a)^2}{N-1}} \; . \qquad\qquad 2.26$$

In this equation, Z_i = the height of the image at pixel i, Z_a = the average height for the pixels and N = the total number of the pixels.

2.7 Quartz Crystal Microbalance

The quartz crystal microbalance (QCM) technique is commonly used to monitor in-situ film growth during atomic layer deposition. Quartz is a piezoelectric material, which resonates at its fundamental frequency under the influence of an oscillating electric field. The frequency of oscillation decreases when mass is deposited onto the crystal surface. According to Sauerbrey and Lostis [24, 25, 26], the change in resonance frequency of the crystal is linearly proportional to the change in mass deposition.

$$\Delta f \;=\; \frac{-(2 f_0^2 \Delta m)}{A\sqrt{\mu \rho_q}} = K \Delta m \; , \qquad\qquad 2.27$$

where Δf = change in frequency, ρ_q = density of quartz, f_0 = fundamental resonant frequency of unloaded quartz crystal, Δm =mass change, A= surface area, μ = shear modulus of the crystal, and K= Constant.

If the density of the material deposited is ρ_t, the thickness T will be given as:

$$T = \frac{\Delta f}{K\rho_t} \quad . \tag{2.28}$$

In this manner the thickness can be accurately determined by measuring the change in the resonant frequency of the quartz crystal. But Sauerbrey's equation is only valid for very small frequency changes. Lu and Lewis [27, 28] treated the deposited thin film and quartz crystal as a one-dimensional continuous acoustic resonator to give a more accurate thickness measurement equation by simplifying the acoustic impedance matching equation:

$$T = (\frac{N_{AT}\rho_q}{\pi\rho_f f_c Z}) \tan^{-1}(Z \tan[\frac{\pi(f_0 - f_c)}{f_0}]) \quad , \tag{2.29}$$

where N_{AT} = frequency constant for crystal, ρ_f = density of the deposited film,

f_0 = frequency of uncoated quartz crystal, f_c = frequency of coated quartz crystal and Z = acoustic impedance of the quartz crystal/film combination.

The acoustic impedance Z is given by :

$$Z = (\frac{\rho_q \mu_q}{\rho_f \mu_f})^{1/2} \quad , \tag{2.30}$$

where μ_q = shear moduli of quartz and μ_f = shear moduli of the film.

A picture of a polished, gold-plated quartz crystal used in the QCM sensor head is shown in Figure 2.15.
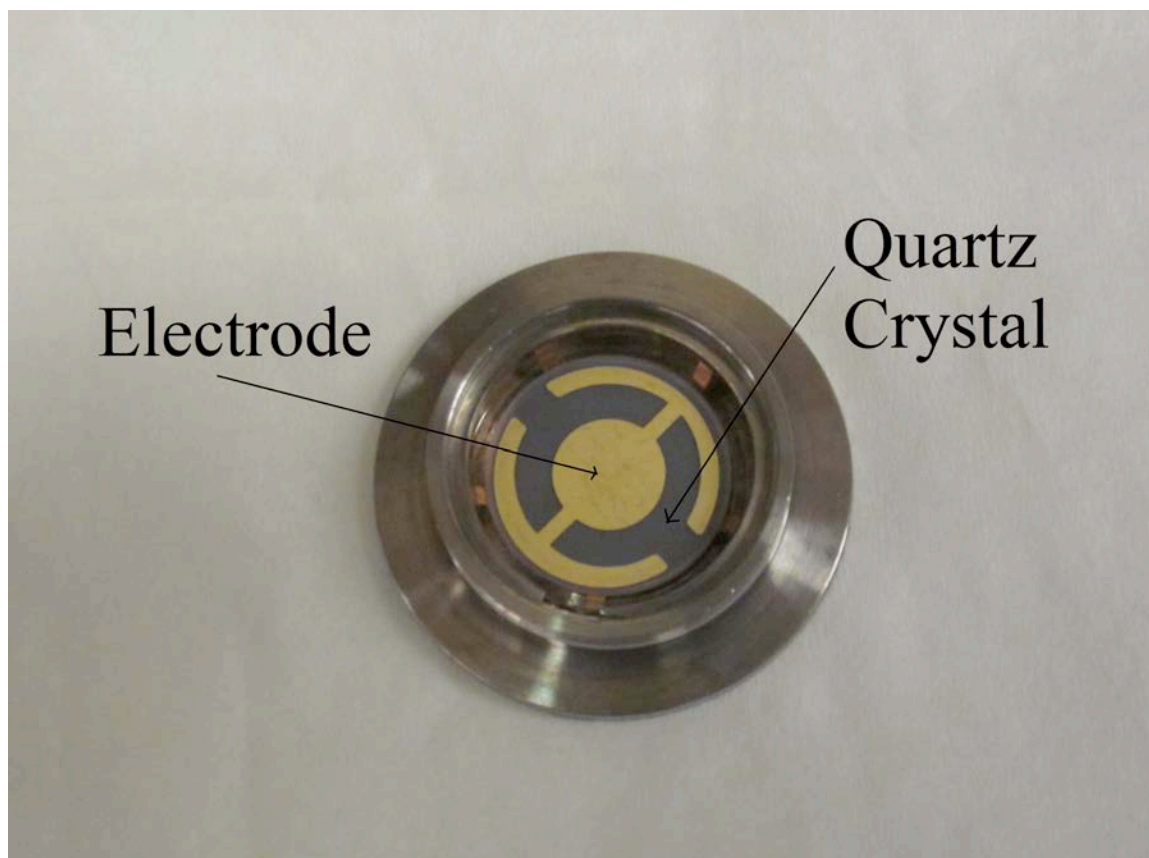
Figure 2.15 Quartz crystal in a sensor head

2.8 References

1. S. Parihar, PhD dissertation, Direct-method analysis of surface alloying using surface X-ray diffraction, 2008, p. 6.

2. L. G. Parratt, Phys. Rev. **95**, 359 (1954).

3. M. Birkholz, *Thin film analysis by X-ray scattering* (WILEY-VCH Verlag GmbH & Co; 2006)

4. Paul F Fewster, Rep. Prog. Phys. **59**, 1339 (1996).

5. B.D Cullity, *Elements of X-ray diffraction* (Addison- Wesley Publishing Company Inc., 1978), p. 102.

6. M. Gierer, M. A. Van Hove, A. I. Goldman, Z. Shen, S. L. Chang, P. J. Pinhero, C. J. Jenks, J. W. Anderegg, C. M. Zhang, and P. A. Thiel, Phys. Rev. B **57**, 7628 (1998).

8. D. K. Saldin, G. R. Harp, B. L. Chen, and B. P. Tonner, Phys. Rev. B **44**, 2480 (1991).

9. J. B. Pendry, *Low energy electron diffraction* (Academic Press, London and New York, 1993).

10. M. A. Van Hove, and S.Y. Tong, *Surface crystallography by LEED* (Springer-Verlag Berlin Heidelberg, New York, 1979).

11. C. Davisson, and L. H. Germer, Nature **119**, 558 (1927).

12. J. W. Watts, *An introduction to surface analysis by electron spectroscopy* (Oxford University Press, London, 1990).

13. L. C. Feldman, J. W. Mayer, *Fundamentals of surface and thin film analysis* (North-Holland, New York, 1986).

14. D.P. Woodruff, and T. A. Delchar, *Modern techniques of surface science* (Cambridge University Press, 1994), p. 586.

15. J. F. Moulder, W.F. Stickle, P. E. Sobol, and K. D. Bomben, *Handbook of photoelectron spectroscopy* (Perkin-Elmer Corporation, Physical Electronic Division, 1992), p. 86.

16. M. Prutton, *Introduction to surface physics* (Oxford Science Publications, 2002). p. 24.

17. M. Higashiwaki, S. Chowdhury, B. L. Swenson, and U. K. Mishra, Appl. Phys. Lett. **97**, 222104 (2010).

18. M. C. Biesinger, L. W. M. Lau, A. R. Gerson, and R. St. C. Smart, Appl. Surf. Sci. **257**, 887 (2010).

19. M. Balkanski, and R. F. Wallis, *Semiconductor Physics and applications* (Oxford University Press, 2000). p. 240.

20. R. A. Van Leeuwen, C. J. Hung, D. R. Kammler, and J. A. Switzer, J. Phys. Chem. **99**, 15247 (1995).

21. F. K. Shan, and Y. S. Yu, Thin Solid Films **435**, 174 (2003).

22. J. Tauc, R. Grigorov, and A. Vancu, Phys. Status Solidi **15**, 627 (1966).

23. W. R. Bowen, and N. Hilal, *Atomic force microscopy in process engineering* (Elsevier Science 2009). p.5.

24. G. Sauerbrey, Zeitschrift für Physik **155**, 206 (1959).

25. P. Lotis, Rev. Opt. **38**, 1 (1959).

26. C. Lu, A.W. Czanderna, *Methods and phenomena, Vol. 7: Applications of piezoelectric quartz crystal microbalances* (Elsevier Science, Amsterdam 1984). p. 393.

27. J. G. Miller, and D. I. Bolef, J. Appl. Phys. **39**, 5815 (1968).

28. C. Lu, and O. Lewis, J. Appl. Phys. **43**, 4385 (1972).

Chapter 3

Atomic Layer Deposition and UHV-interfaced viscous-flow reactor

Abstract

This chapter reviews the fundamentals of atomic layer deposition (ALD), along with its advantages and disadvantages as a thin film growth technique. The second part of the chapter gives a detailed description of the instrumentation of our UHV-interfaced viscous-flow reactor with quartz crystal microbalance, which was developed for thin film growth by atomic layer deposition. This chapter also describes how our viscous-flow reactor was implemented for ZnO ALD.

3.1 Introduction

Atomic Layer Deposition (ALD) is a technique for depositing thin films one atomic layer at a time. ALD was developed and introduced with the name of Atomic Layer Epitaxy (ALE) in the late 1970s by Suntola and his Finnish co-workers [1-4]. The Finnish group was motivated to use ALD for production of thin-film electro luminescence displays (TFEL), where thin films with uniform thickness, high dielectric strength and chemical stability over large areas are required [5-10]. In Figure 3.1 a cross-section of such thin film electro luminescence device has been shown.
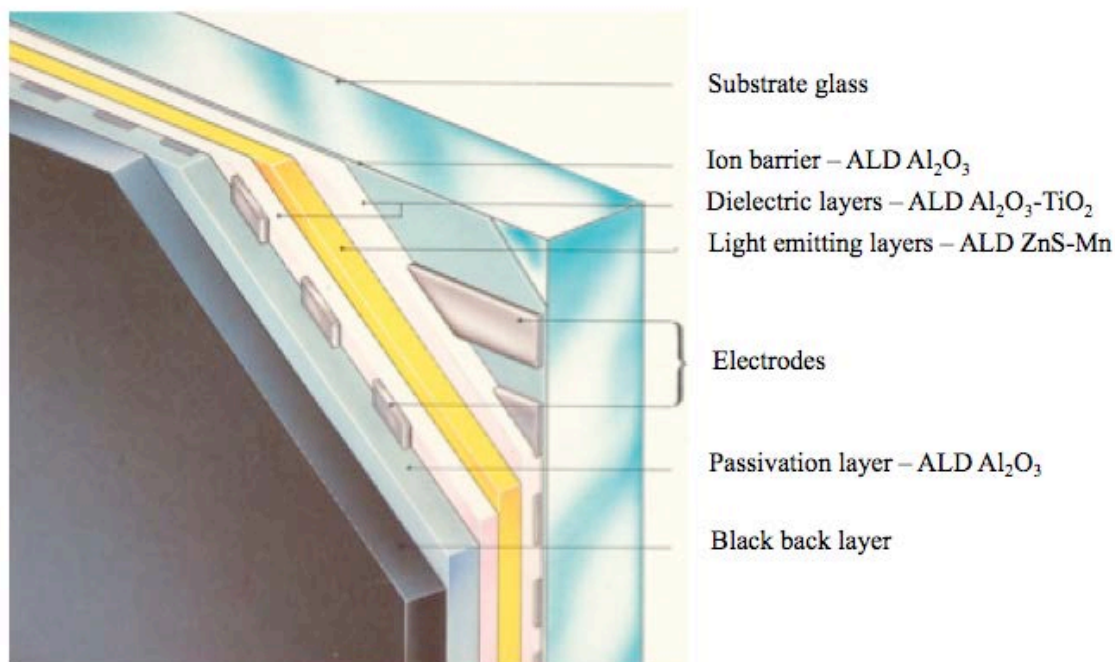
Figure 3.1 Structure of an ALD TFEL display (Adopted from Ref. [11]).

After successful development of the ALD process in TFEL production, growth of III-V semiconductor compounds using ALD became an active interest, as it had potential impact on the commercial manufacture of integrated circuits. Also, with continuous shrinkage of device dimension and increase of the aspect ratio in silicon-based

microelectronic devices, ALD became a potential substitute for the conventional chemical vapor deposition (CVD) or physical vapor deposition (PVD). Since the mid 1990s, ALD has slowly and steadily found many application areas in the fields of solar cells, passivation of surfaces, gas sensors, batteries, microelectronics, nanostructures, optics, magnetic heads, fuel cells, self-assembled monolayers, and biomedical applications among many other applications [12-30]. At present ALD is the only thin film technology that can uniformly coat large surfaces with atomic level precision and conformal coverage for thicknesses less than 50 nm.

3.2 Basic principle of Atomic Layer Deposition (ALD)

Atomic Layer Deposition is a chemical gas phase thin film deposition technique with precision of atomic layer control. ALD utilizes two binary, self-limiting chemical reactions sequentially to grow thin films layer by layer. As a result of exposing the surfaces to two distinct chemicals alternatively during ALD, it coats surfaces with uniform, smooth, conformal and pinhole-free films. The unique character of ALD is that each chemical is introduced in the reactor one at a time, and it exploits a self-limiting reaction on the surfaces to form a monolayer [31,32]. In chemical vapor deposition (CVD), in contrast, both chemicals are exposed to the surfaces at the same time.

A typical ALD cycle consists of four different steps and these four steps are repeated in a cyclic manner to grow thin films to the desired thickness. These four steps are:

(i) Exposure of the first precursor

(ii) Purge or evacuation of the excess precursor with inert gas

(iii) Exposure of the second precursor

(iv) Purge or evacuation of the excess precursor with inert gas
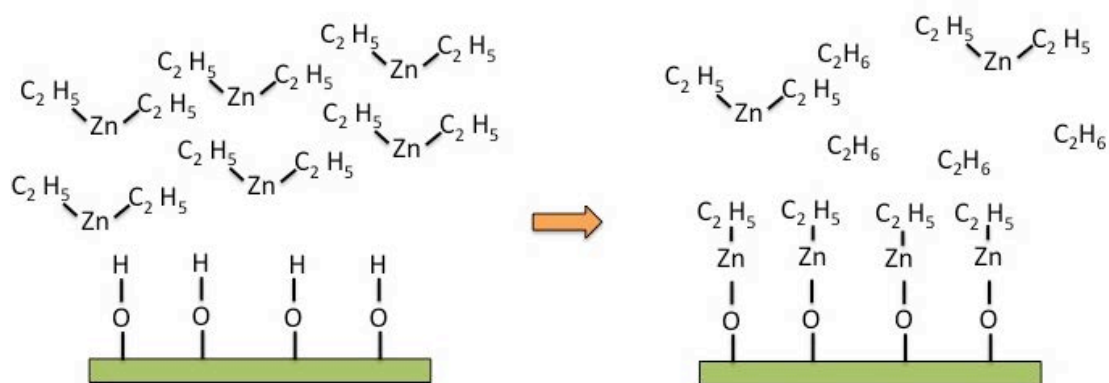
STEP 1
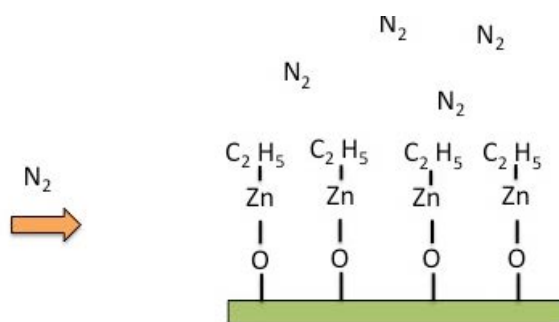
STEP 2

[Caption on next page.]

STEP 3

STEP 4
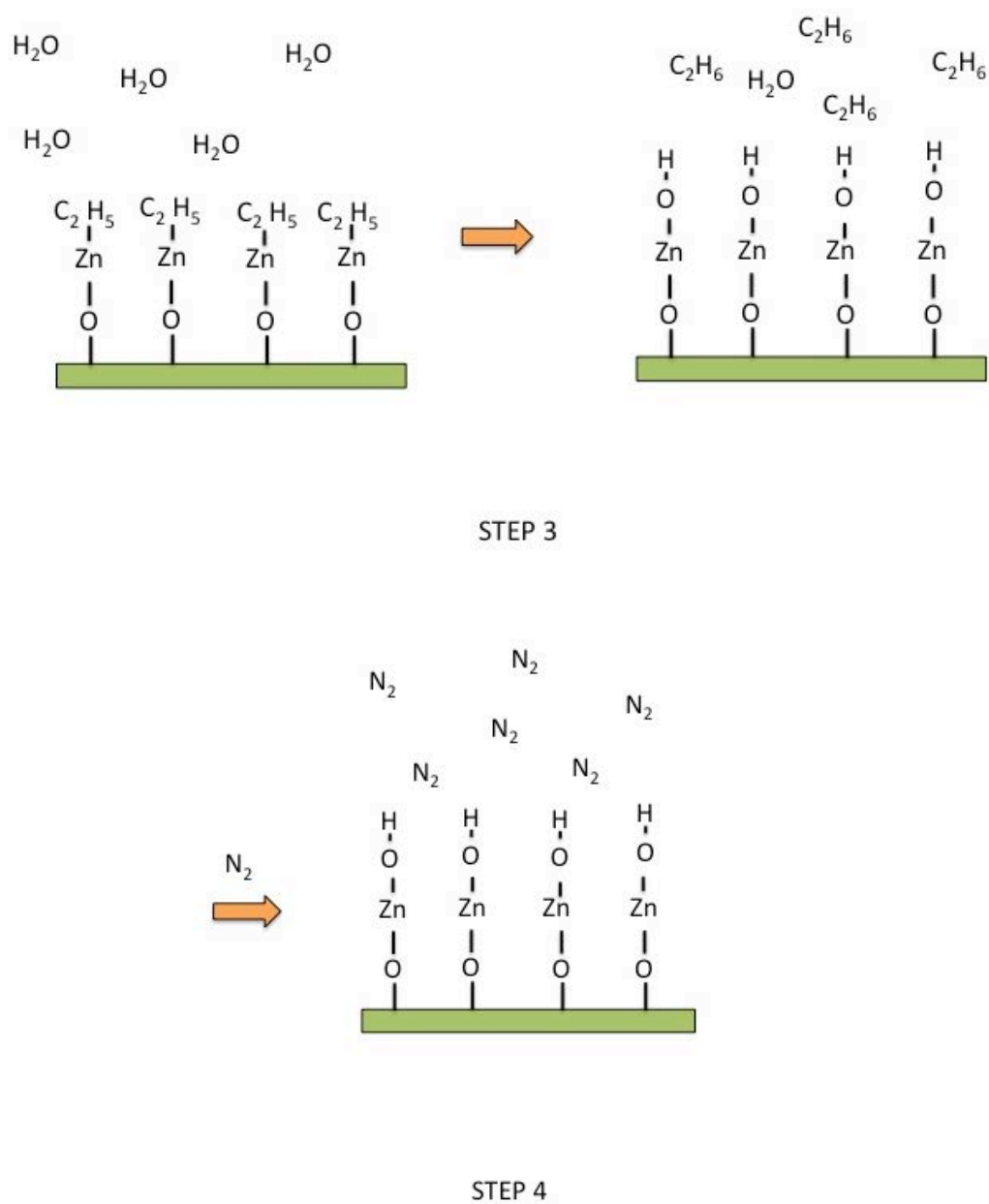
Figure 3.2 Schematic of an ALD cycle. a) Exposure of first precursor. b) Purging with

inert gas. c) Exposure of second precursor. d) Purging with inert gas.

A schematic of an ALD cycle of ZnO growth using di-ethyl Zinc (DEZ) and water is illustrated in Figure 3.2. In the first step, the metallorganic precursor DEZ is exposed to a surface terminated with hydroxyl groups. The DEZ reacts with the hydroxyl groups and forms $O-Zn-C_2H_5$ ligands on the surface, with ethane (C_2H_6) as a byproduct. The metallorganic precursor DEZ keeps reacting with the surface, until there are no available surface sites. Once all of the surface sites react, the surface saturates, and DEZ stops reacting. This is called a self-limiting reaction. In the second step, the ALD reactor is purged with an inert gas such as nitrogen or argon. This inert gas purges any byproduct of the first reaction and the unreacted first precursor DEZ from the reactor. In the third step, the second precursor, water, is introduced. The water undergoes similar self-limiting exchange reaction to form $O-Zn-OH$ ligands on the surface, with ethane (C_2H_6) as byproduct. The water reacts with the surfaces until the surface saturates. These two self-limiting reactions in step 1 and 3 result in the formation of one monolayer of ZnO film. Also the surface reverts back to its original state, with a hydroxyl termination. In the fourth step, the excess unreacted water and byproduct ethane is purged away with an inert gas. Next, these four steps are repeated several times to grow the binary compound ZnO layer by layer [32].

It is important to ensure that the precursor dose is large enough to complete the reaction and cover the surfaces. Also it is important to purge the reactor long enough so that all the excess precursor and the byproducts are evacuated from the chamber. This eliminates the possibility of CVD kind of gas phase reaction.

If the initial surface is not terminated with the proper functional group (here hydroxyl) to initiate the self-limiting reaction, the first precursor is chemisorbed on the

surface and initiates the film growth. The amount of film growth depends on the number of chemisorption sites on the surface. Often, for oxides, the surface get hydroxyl-terminated after exposure of water. Also, hydroxyl coverage is dependent on temperature. For metal-oxide films, exposure of the surface to water or another oxidizing precursor before starting the growth is a common practice. This increases the number of reaction sites (here hydroxyl group) to initiate the reaction with second precursor.

3.3 Advantages of Atomic Layer Deposition (ALD)

The self-limiting nature of chemical reactions during alternate pulsing used to grow films using the ALD process enables ALD to enjoy several advantages over the other thin film growth techniques.

(i) Accurate thickness control

(ii) Conformal coating

(iii) Large area uniformity

(iv) Reproducibility

(v) Capability to produce sharp interfaces, superlattice and multilayer structures

(vi) Atomic level control of chemical composition

(vii) Pinhole-free, low defect density, high quality thin films at low temperature

(viii) Easy scale-up and large batch capabilities

(ix) Low-temperature deposition allows deposition even on biomaterials

(x) Processing temperature window is often wide

(xi) Uncontrolled vaporization rate of solid precursor is not a problem in ALD

Because of these advantages, when the substrates are large, complex shaped or porous and the coating has to be uniform, conformal, thin (< 100 nm), accurate, or of high quality, ALD is preferable over other thin film techniques.

3.4 Disadvantages of Atomic Layer Deposition (ALD)

Even though ALD has several advantages over other thin film deposition techniques, it has some limitations, too.

(i) ALD is a very slow process. The average growth rate is ~ 1 to 5 nm min^{-1}. (This limitation can be compensated by large batch processing and optimizing the ALD cycle time.) Also, when extremely thin films (< 30 nm) are necessary, this slowness is potentially a benefit.

(ii) The other main limitation is cost effectiveness and that good ALD processes for many pure elements (e.g Au, Mg, Zn), nitrides (e.g Si_3N_4, BN) are not developed fully.

(iii) Area-selective atomic layer deposition is still not developed for all materials.

(iv) ALD does not alway grow thin films in a layer-by-layer manner to produce a full monolayer per cycle. A fraction of a monolayer can instead be deposited in each ALD cycle. This feature can be attributed to the limited number of reactive surface sites and steric hindrance of the ligand groups.

(v) ALD also does not always produce atomically smooth surfaces. For polycrystalline films, nucleation and grain growth generally causes much rough surfaces in comparison, epitaxial and amorphous films produced by ALD are considerably smoother.

A relative comparison of ALD, chemical vapor deposition (CVD), physical vapor deposition (PVD) and molecular beam epitaxy (MBE) is listed in Table 3.1.

Table 3.1 A Comparison of different deposition techniques.

	ALD	CVD	PLD (Pulsed-laser Deposition)	MBE (Molecular Beam Epitaxy)
Deposition rate	poor	excellent	good	acceptable
Step coverage	excellent	varies	poor	poor
Density	excellent	excellent	good	excellent
Defects	acceptable	acceptable	fair	excellent
Thickness uniformity	excellent	excellent	fair	acceptable
Sharp interfaces	excellent	varies	varies	excellent
Material availability	acceptable	acceptable	fair	excellent

3.5 Growth per cycle of Atomic Layer Deposition (ALD)

Growth of thin films per ALD cycle is measured in terms of thickness per ALD cycle or mass deposited per ALD cycle. Growth per cycle in ALD depends strongly on temperature. It also depends on length of precursor exposure time (unless saturation is achieved), and can also depend on purge time.

3.5.1 Dependence of growth per cycle on temperature (ALD Window)

The most important parameter to achieve good ALD growth is to find the ALD temperature window, where a self-limiting exchange reaction can occur. Usually ALD is a low-temperature growth technique, and most of the ALD reactions require less than 500°C. The temperature dependence of the growth rate is illustrated in Figure 3.3. At low temperature, low-vapor-pressure precursors can condense and give rise to a higher growth rate. Also at low temperature, the reaction rate is so slow that the reaction may not complete to form a full monolayer. This is because, in that temperature region, the activation energy is not high enough to expedite the reaction. This can substantially decrease the growth rate at lower temperatures. At too high temperatures, the precursors can desorb or decompose on the surfaces. If the precursor decomposes, the growth rate will be increased. When the precursor desorbs from the surfaces before reacting with the second precursor, the growth rate will decrease. In between these two temperature regions, the growth rate is nearly independent of the temperature. This temperature region is called the ALD temperature window [31,32]. In the ALD temperature window, one full monolayer of film is grown in each ALD cycle.
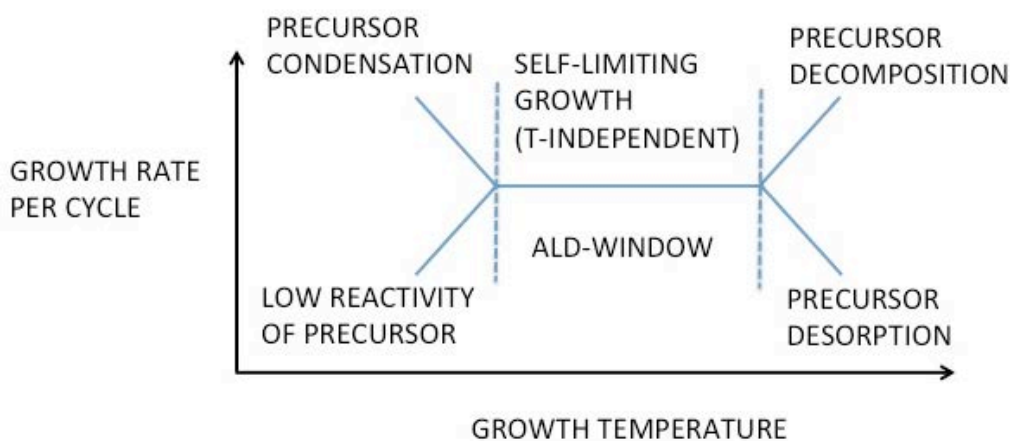
Figure 3.3 Various growth rates vs. temperature and ALD process window.

3.5.2 Dependence of growth per cycle on pulse time

The effect of the precursor pulse time on the growth rate can be studied by varying the precursor pulse duration while keeping all other ALD growth parameters constant. A schematic of such typical dependence of growth per cycle with increasing precursor pulse time is shown in Figure 3.4. From the figure, it can be observed that there is no growth at very low precursor pulse times. This is called the initial delay, in ALD growth [32]. After that, there is a sudden increase in growth rate, followed by a slow increase to become saturated. The initial delay is observed because very few precursor molecules arrive to the substrate at this small precursor exposure time; most of the precursor is consumed upstream to coat the surfaces of the reactor before it reaches the substrate. Once sufficient numbers of the precursor molecule reach the substrate, they react with the surface reaction sites rapidly to give a large growth rate. Upon increasing

the precursor pulse time, the growth rate saturates to give one monolayer growth rate per cycle. How fast the growth rate reaches the saturation level depends on how reactive the precursors are and what is the growth temperature. At lower temperature, a longer precursor pulse is required to reach the saturation level. On further increase of precursor pulse time the growth rate does not increase. This is because of the self-limiting nature of the chemical exchange reaction occurring on the surfaces of the substrates. Once all the reaction sites have been exhausted, no further reaction takes place even with an increase in the precursor pulse time.
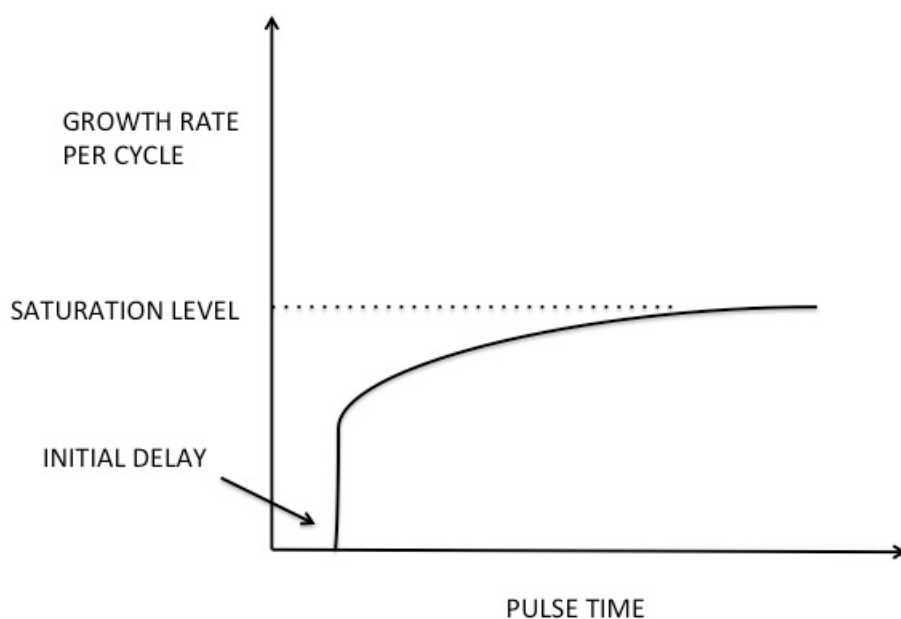
Figure 3.4 Growth rate per cycle vs. precursor pulse time keeping all other growth parameters constant.

3.5.3 Dependence of growth per cycle on purge time

A long purge time is desirable in ALD cycles. This ensures the two precursors are completely evacuated from the reactor chamber and no CVD-like gas phase reaction occurs. Ideally, the growth rate should not change with purge time of the inert gas, but very long purge times can allow the precursor molecules to desorb from the surfaces, leading to a decrease in growth rate.

3.6 Precursors for Atomic Layer Deposition

The choice of proper precursors is very important for successful growth of thin films in ALD. The ALD precursors should meet following requirements [33]:

i) Volatility: The vapor pressure of the precursors should be high enough to transport it to the precursor delivery system for the ALD reactor. Usually, the ALD precursors are introduced in the reactor using an inert carrier gas like nitrogen or argon. The minimum vapor pressure requirement is ~ 0.1 Torr at maximum source temperature. If the precursor is used to coat very large surfaces, higher vapor pressure precursors are preferred. Most ALD precursors are in form of gas or liquid, but solid precursors are also used frequently.

ii) Thermally stable: The ALD precursor should be thermally stable. It should not decompose thermally within the ALD temperature window. Decomposition will destroy the self-limiting growth and also can cause contamination of the film. The ALD precursors should not condense on the substrates within the ALD temperature window. Most low-vapor-pressure precursors are heated to increase the vapor pressure. The

precursor delivery lines are also heated for low-vapor-pressure precursors to prevent them from condensing inside the precursor delivery lines.

iii) Reactivity: for a successful ALD process, highly reactive precursors are favored. Highly reactive precursors react aggressively and surface saturation is reached quickly. These factors promote shorter ALD cycle times and higher throughput. Highly reactive precursors also complete the reactions fast.

iv) Unreactive, volatile byproducts, which are easy to evacuate and dispose of.

v) No etching of films or the substrates on reaction.

vi) Highest purity of the precursor can be chemically achieved easily.

vii) Inexpensive.

viii) Easy to synthesize and handle.

ix) Environmental friendly and non toxic.

x) High growth rate.

Using proper ALD precursors one can easily grow a variety of materials, such as metals, elemental semiconductors, III-V semiconductors, oxides, nitrides, sulfides, II-VI compounds, ternary oxides and fluorides. These ALD precursors are also used to create mixed, nanolaminate and multilayer materials that do not exist in nature. Some of the technologically important materials are listed in the Table 3.2.

Most cases of ALD involve one metal precursor and one non-metal precursor to deposit binary materials. For metal precursors, alkyl compounds, halides, alkoxides, β-diketonates complexes, cyclopentadienyl compounds, carboxylates, acetamidinates, hydrides, and silylamides are often used. For non-metal precursors, water, ozone,

ammonia, hydrogen sulfide, hydrogen peroxide, alcohols, and oxygen radicals or plasmas are frequently used.

Most recently, the use of organic polymers as precursors has created a new kind of deposition technique called molecular layer deposition (MLD). The use of both conventional ALD precursors and MLD precursors has created a way to deposit new hybrid organic-inorganic materials.

In conclusion, ALD can deposit a wide variety of materials that can be used as insulators, diffusion barriers, transparent conducting oxides, non-volatile or flash type memory, DRAM capacitors, metallization layers, photo-catalysts, MEMS, and in optical communications. Although ALD can deposit diverse materials, development of new ALD precursors for multiferroic materials, phase-change materials, spintronics materials, and new metals are still very challenging. Table 3.2 lists some of the materials widely deposited by ALD.

Table 3.2 Different thin-film material deposited by ALD.

II-VI Compounds	ZnS, ZnS:M(M= Mn,Tb), ZnSe, ZnTe, CdTe, BaS,CdS, SrS HgTe, $ZnS_{1-x}Se$, $Hg_{1-x}Cd_xTe$
III-VI Compounds	GaAs, AlAs, GaP, InP, InAs, $Ga_xIn_{1-x}As$,
Nitrides (semiconductor)	AlN, GaN, InN, SiN_x
Nitrides (metallic)	TiN, TaN, NbN
Oxides (Dielectrics)	Al_2O_3, SiO_2, HfO_2, CeO_2, Nb_2O_5, ZrO_2, $SrTiO_3$, Y_2O_3

Oxides (Transparent Conducting Oxides)	ZnO, ZnO:Al, In_2O_3, In_2O_3: Sn, In_2O_3:F, In_2O_3:Sb, NiO
Fluorides	ZnF_2, SrF_2, CaF_2
Metals	Cu, W, Ta, Pt, Ni, Co, Al, Fe, Mn
Other	$LaCoO_3$, SiC, $YBa_2Cu_3O_{7-x}$, $LaNiO_3$, Si, Ge

3.7 ALD reactors

For successful ALD growth one needs an efficient ALD reactor along with the proper choice of precursors. The ALD process can be performed over wide range of pressures from atmospheric to ultrahigh vacuum (UHV). Depending on the operating pressure, ALD reactors can be classified as flow-type or molecular flow type reactors. The flow-type reactor resembles a conventional CVD-type reactor, whereas the molecular-flow type reactor resembles a molecular beam epitaxy (MBE) chamber. Both have their advantages and disadvantages. Flow-type reactors are often used in large-scale production. Purging during ALD is much faster in flow-type reactors than evacuation in the molecular-flow type ALD reactor.

3.7.1 Molecular flow type ALD reactor

Molecular-flow-type ALD reactors operate under ultrahigh vacuum (UHV) conditions. This kind of reactor pumps away the unreacted precursor and reaction products in between the two precursor exposures, and thereby avoid the intermixing of the two precursors during the ALD cycles. Generally, the molecular-flow type reactor has much slower deposition rates than the flow-type ALD reactor, because the molecular-flow type reactors need longer exposure and evacuation times. These long cycle times hurt the throughput of the reactor. One of the advantages of using UHV while depositing film by ALD is that one can use many *in-situ* surface analysis techniques like low energy electron diffraction (LEED), X-ray photoelectron spectroscopy (XPS), reflection high energy electron diffraction (RHEED), and Auger electron spectroscopy (AES). This wide variety of *in-situ* analytic techniques can be used to investigate the thin film growth, or the chemistry of each ALD half-reaction.

3.7.2 Flow type ALD reactor

The flow-type ALD reactor works at pressures ranging from 1 to 10 Torr. The flow-type reactors are designed to minimize the exposure and purging time and thereby maximize the precursor utilization and throughput. Thus flow-type reactors are useful for batch production. There are different flow geometries that can be used in flow-type ALD reactors, as shown in Figure 3.5 [22,34].
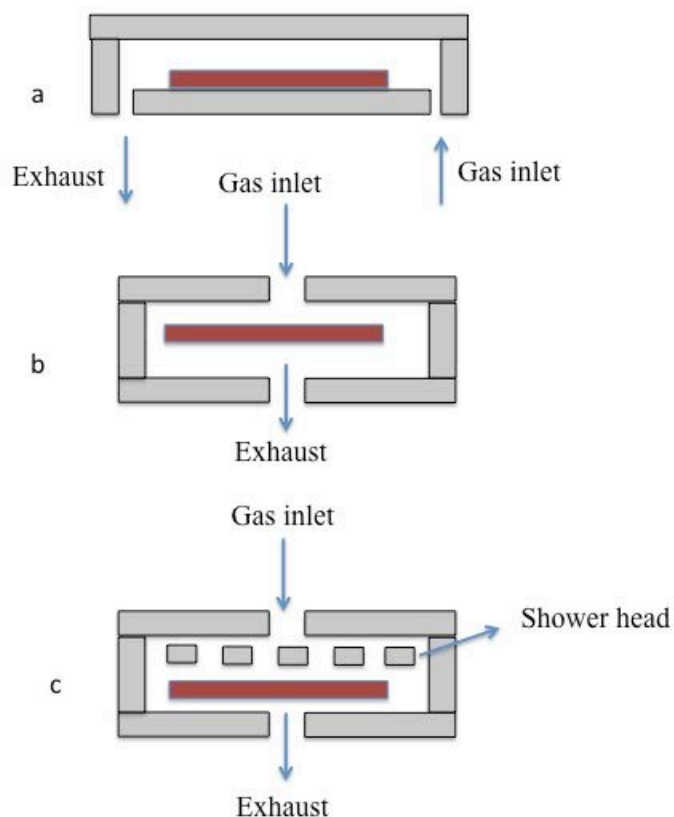
Figure 3.5 Different types of ALD reactors. (a) cross-flow type; (b) single injector type; (c) shower-head type ALD reactor.

In order to grow ZnO thin films using ALD, we have designed and constructed a viscous-flow ALD reactor. The design is heavily based on that of Elam, Groner, and George [35]. In our installation, this reactor is attached to an existing UHV surface-analysis chamber.

3.8 UHV-interfaced viscous-flow ALD reactor with *in-situ* quartz crystal microbalance

We have designed and constructed a viscous-flow ALD reactor with *in-situ* quartz crystal microbalance (QCM). *In-situ* QCM enables us to monitor the growth rate during ALD in real time. The viscous-flow ALD reactor has six major components:

i)   Flow-tube or the reaction chamber

ii) Carrier gas supply and precursor sources

iii) Precursor gas switching

iv) Heating of reaction chamber

v)   Vacuum pumps and exhaust system

vi) Quartz crystal microbalance

3.8.1 Flow-tube or the reaction chamber

Figure 3.6 shows the schematic of the viscous-flow ALD reactor. The flow tube is made from a stainless steel tube with an outer diameter of 2.5 inches. One end of this tube is connected with a 4-1/2 inch spherical square vacuum chamber (from Kimball Physics Inc.) consisting of two 4-1/2 inch Conflat (CF) ports and four 2-3/4 inch CF

ports. Other end of the reactor tube is connected to a 2-3/4 inch six-way cross
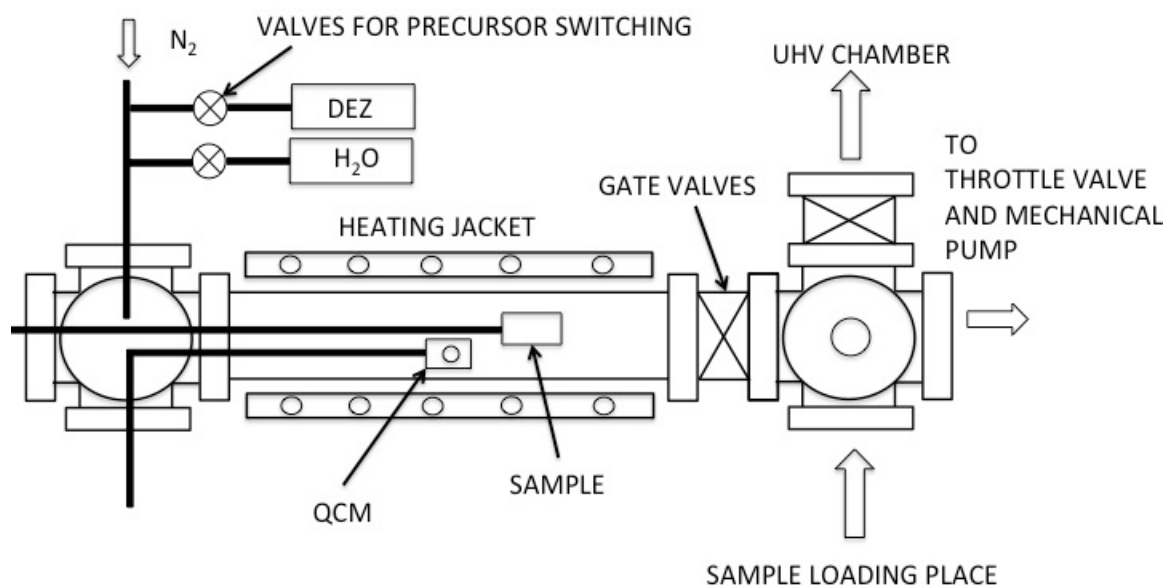
Figure 3.6 Schematic of viscous-flow ALD reactor.

through a gate valve. One side of the six-way cross is occupied by a linear motion

feedthrough (MDC 661018). The linear motion feedthrough has been modified to hold a

sample holder. The holder is shown in Figure 3.7. Another port was used to connect to

another gate valve which is connected with an UHV chamber, which has RHEED and

MBE facilities. A third port was connected with a cryo sorption pump (from Varian). The

cryo sorption pump is used to achieve miliTorr pressure before the sample is transferred

to the attached UHV-chamber.

The sample is introduced to the reactor chamber through the fourth port. Once the sample is placed on the top of the linear feedthrough, the sample is moved up and a sample transfer rod is used to bring the sample from that holder to the thin-film deposition zone. The sample transfer rod is ~ 70 inches (2m) long. The sample transfer rod is interfaced to the reactor through one of the 4-1/2 inch CF ports of the spherical square vacuum chamber. The sliding seal of the transfer rod is differentially pumped so that it does not introduce air to the ALD reactor chamber.
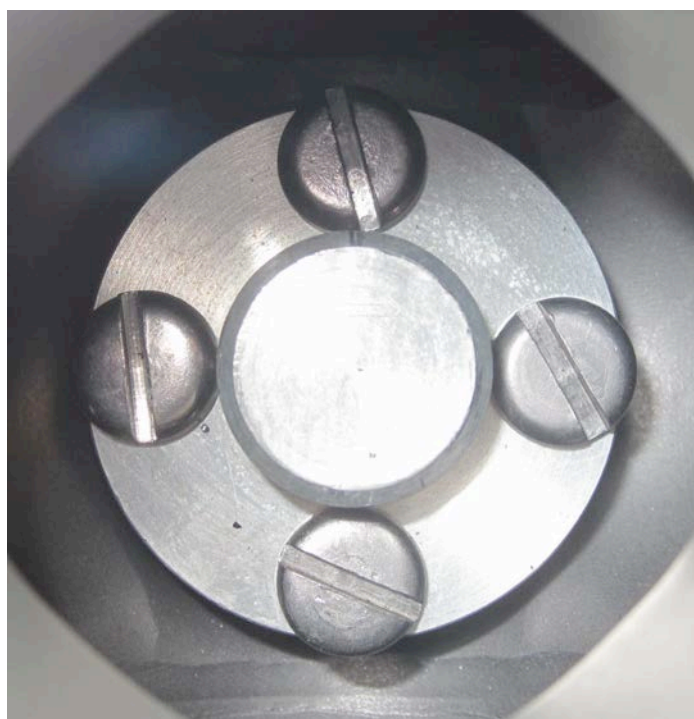
Figure 3.7 Sample Mount.

3.8.2 Carrier gas supply and precursor sources

The ultra-high purity nitrogen (99.999% Praxair Inc.) is supplied to three mass flow controllers (MFC). An MKS 247 power supply and readout provides power and sets

the desired flow rate for these MFCs. Before entering the MFCs, the carrier gas was purified using an Aeronex GateKeeper inert gas purifier. This filter reduces particulate, oxygen, water, and hydrocarbon contamination in the carrier gas to the ppm level. The ALD reactor has three independent precursor delivery lines. Three different precursors can be delivered to the ALD reactor via ultra high purity nitrogen carrier gas. For ZnO ALD, liquid dietheyl zinc (DEZ) (96%) from Strem Chemical Inc. and Fisher Scientific deionized ultra filtered water were used. The liquid precursors have much higher vapor pressures (water~ 22 torr, DEZ ~18 torr) at room temperature than the reactor operating pressure of 1 torr. Accordingly, the precursors were dosed directly from the precursor delivery bottles, which were kept at room temperature. The precursors were freeze-pumped and thawed a few times after they were attached to the ALD reactor to remove any residual gas present in the precursor delivery bottle.

3.8.3 Precursor gas switching

To achieve ALD, the precursors were dosed alternatively to the carrier gas before entering the ALD reactor. Alternate pulsing of precursors was achieved using pneumatically actuated solenoid valves, which were installed between the precursor source and the reaction chamber. Figure 3.8 represents a schematic of solenoid valves used for gas switching of DEZ. Similar arrangements were made for the water precursor channel. Both in water and DEZ precursor channels, 1/4 inch VCR connections were used throughout, making the channels modular and easy to re-configure.

Two pneumatically actuated Swagelok diaphragm valves were used to perform the gas switching. Pneumatic actuation was achieved using two Mac Series 34 solenoid

valves. Further downstream, an inline gas filter Wafergard F Mini from Mykrolis was used to trap any particles (less than 0.03 particles/liter) during precursor dosing process. A manually controlled Swagelok BM Series needle valve was attached further downstream to establish sonic flow of precursor through needle valve and to adjust the amplitude of the precursor pressure pulse. At the end of the precursor line, a Swagelok shut-off valve was installed. After the shut-off valve 1/4 inch stainless tube line was used to connect the precursor channel to one of the remaining ports of the spherical square vacuum chamber.
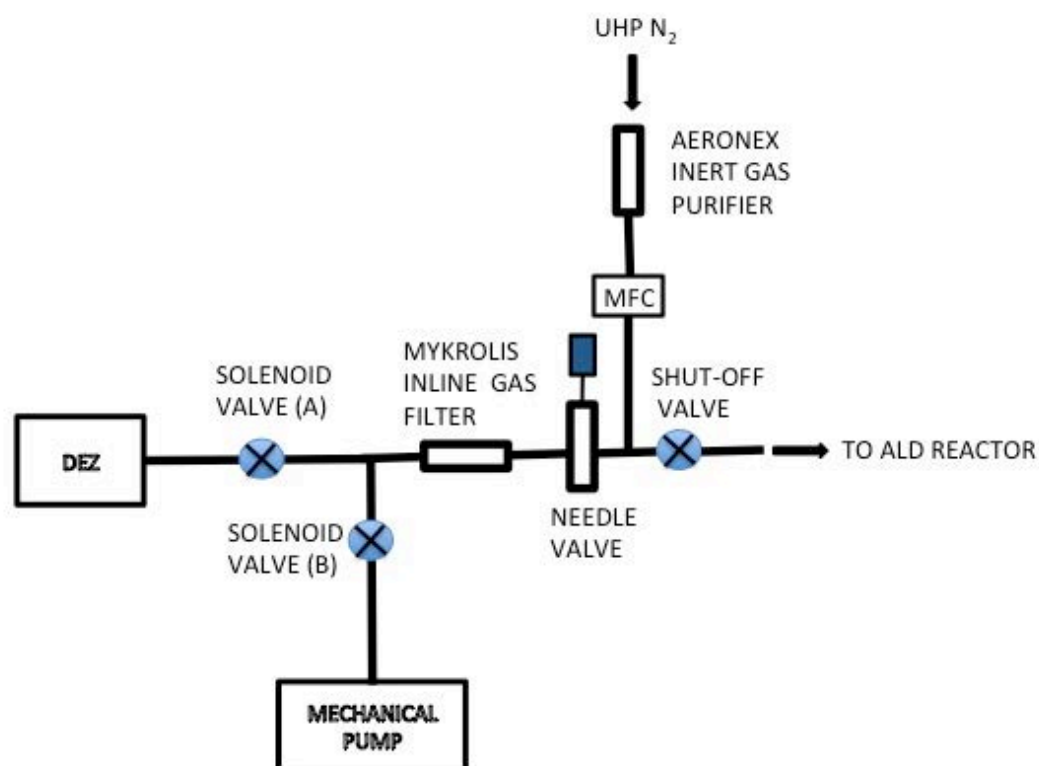
Figure 3.8 Precursor channel with gas switching valves

To achieve precursor gas switching, the valves A and B in the Figure 3.8 were turned on and off alternatively. When valve A is open and B is closed, the DEZ is dosed in the ALD chamber. This is called exposure mode. When valve A is closed and B is open, only ultra high pure nitrogen is flowing in the ALD chamber. This is called the purge mode. In the purge mode some nitrogen gas flows from MFC to the pump. This nitrogen flow not only purges the DEZ line but also creates a diffusion barrier for any DEZ leaks from valve A. One DEZ exposure mode and one purge mode makes up a half cycle. Similarly in the water precursor channel, another two solenoid valves open and close alternatively to make up another half cycle. This half cycle consists of water exposure followed by a purge. A full cycle is achieved in this manner by opening and closing the solenoid valves in a timely fashion. Figure 3.9 shows a schematic of such ALD cycles. A digital and analog NI DAQ 6221 board interfaced with a personal computer was used to control the opening, closing, and the duration of the time these solenoid valves will remain open and closed. These in turn control the exposure times and purge times in an ALD cycle.
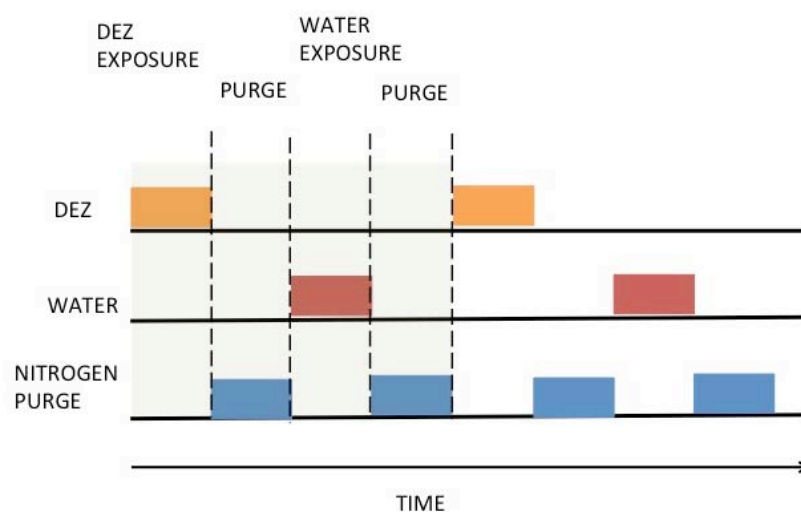
Figure 3.9 Precursor gas switching process

A program written in LabView was employed to control the NI DAQ 6211 board.

3.8.4 Heating of the reaction chamber

The flow-tube of the reactor was covered by a heating jacket, which heats the tube wall resistively. Samples inside this flow tube were heated by radiation and convection from the hot walls. The temperature of the reactor wall was controlled with a CAL 9300 proportional, integral, differential (PID) temperature controller. The reactor temperature can be maintained in the temperature range 50-400 °C. A chromel-alumel thermocouple was attached just below the substrate holder to monitor the ALD growth temperature.

3.8.5 Vacuum pumps and exhaust system

An Alcatel 2015C2 rotary vane mechanical pump was used to evacuate the reactor. The pump oil was flushed with nitrogen gas to eliminate the reactive gas contamination to the pump oil. An oil recovery kit from Alcatel Adixen OME 25HP was also installed in the exhaust of Alcatel pump. A bubbler with water was used in the exhaust stream to reduce the amount of reactant gas in the exhaust. Another mechanical pump Pfeiffer DUO 004B was used to pump the precursor channels and the differentially pumped region of the sample transfer rod. Both mechanical pumps were equipped with stainless-steel wool traps to prevent oil back-streaming.

A throttle valve and a 2 Torr Baratron capacitance manometer (MKS 626A) were installed upstream of the Alcatel 2015C2 rotary vane mechanical pump. The pressure transducer (MKS 626A) measures the pressure of the ALD chamber. It is connected with a pressure controller (MKS 651C). The function of the pressure controller is to vary the

effective pumping speed by changing the conductance of the throttle valve, thereby achieving and maintain the desired pressure.

3.8.6 Quartz crystal microbalance

The viscous-flow ALD reactor was equipped with an in-situ quartz crystal microbalance (QCM). The quartz crystal microbalance (QCM) technique is widely used to measure line-of-sight deposition on the front face of the quartz crystal. A potential problem arises in our ALD application. In absence of any countermeasure, the reactant gases would deposit films on both surfaces of the quartz and prevent accurate mass measurements. To prevent the mass deposition on both faces of the quartz crystal, we have modified the QCM housing to allow us to purge nitrogen over the back side of the quartz crystal. The schematic of the modification is shown in Figure 3.10. The QCM sensor was attached to bakeable Sigma 932-000 sensor head. The water-cooling line of the sensor head was drilled with two 2 mm diameter holes to flow nitrogen on the back surface of the QCM. We purged ~ 20 sccm nitrogen through the modified QCM during the ALD thin film growth. This allowed us to monitor the ALD growth in real time without depositing any material at the back surface of the QCM. Gold-plated, polished 6 MHz quartz crystals from Sigma instruments (Sigma 934-000) were used to overcome the surface roughness effect, as an unpolished QCM sensor has higher surface area than polished QCM sensor. This increased surface area will cause higher mass measurements than expected during ALD growth.   Figure 3.11 shows our modified QCM.
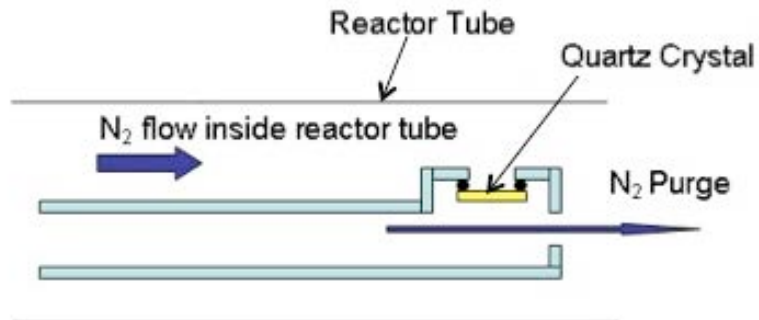
Figure 3.10 Schematic of modified QCM.
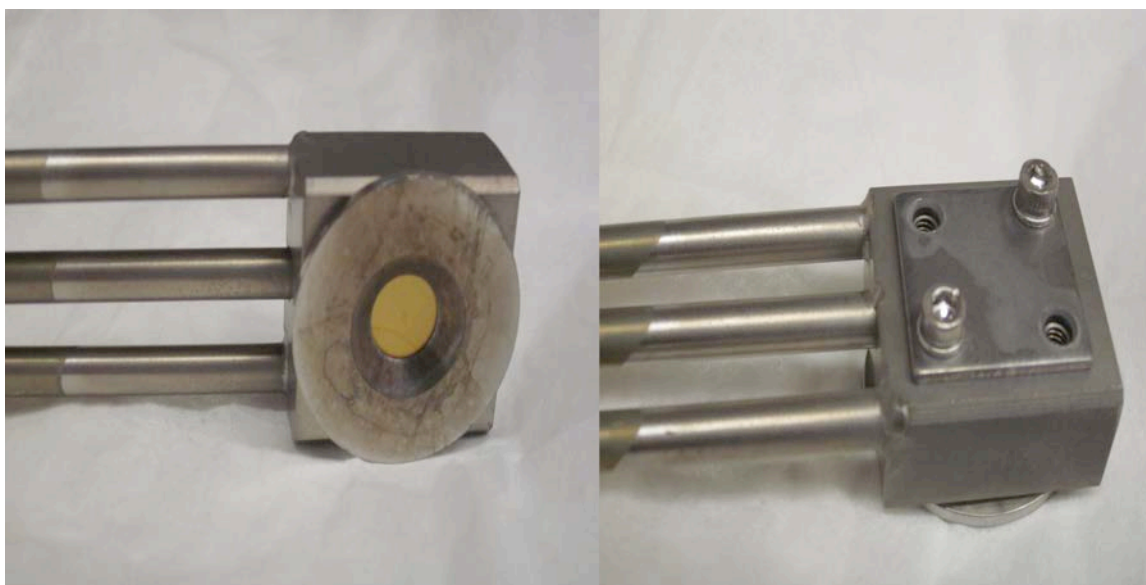
Figure 3.11 Modified QCM to flow nitrogen at the back surface on QCM.

The signal from the QCM sensor was measured with a Sigma SQM 160 thin film deposition monitor. The deposition monitor can measure thickness with a resolution of ~0.037 Å and 8 measurements per sec. A buffer layer of ZnO was deposited on the

polished gold surfaces by several hundreds of ZnO ALD cycles before any measurements were made. This eliminates the possible complications that might arise from the nucleation and growth of ZnO on the gold surface.

Figure 3.12 shows the effect of temperature on QCM frequency measurements. QCM measurements are very sensitive to temperature variation. Small temperature variations can cause an apparent mass change due to large temperature co-efficient (~50Hz/°C at 177°C for AT-cut quartz crystal) of the quartz crystal [36]. Moreover, the temperature co-efficient increases with the cubic power of the deposition temperature. The ALD reactor was kept at the growth temperature for more than 8 hours at 1 Torr to allow the QCM reach thermal equilibrium before any measurements were made. Frequencies were monitored constantly during this heating process untill the frequency shift due to temperature ceased. AT-cut quartz crystals were used to minimize the temperature-induced apparent mass changes.
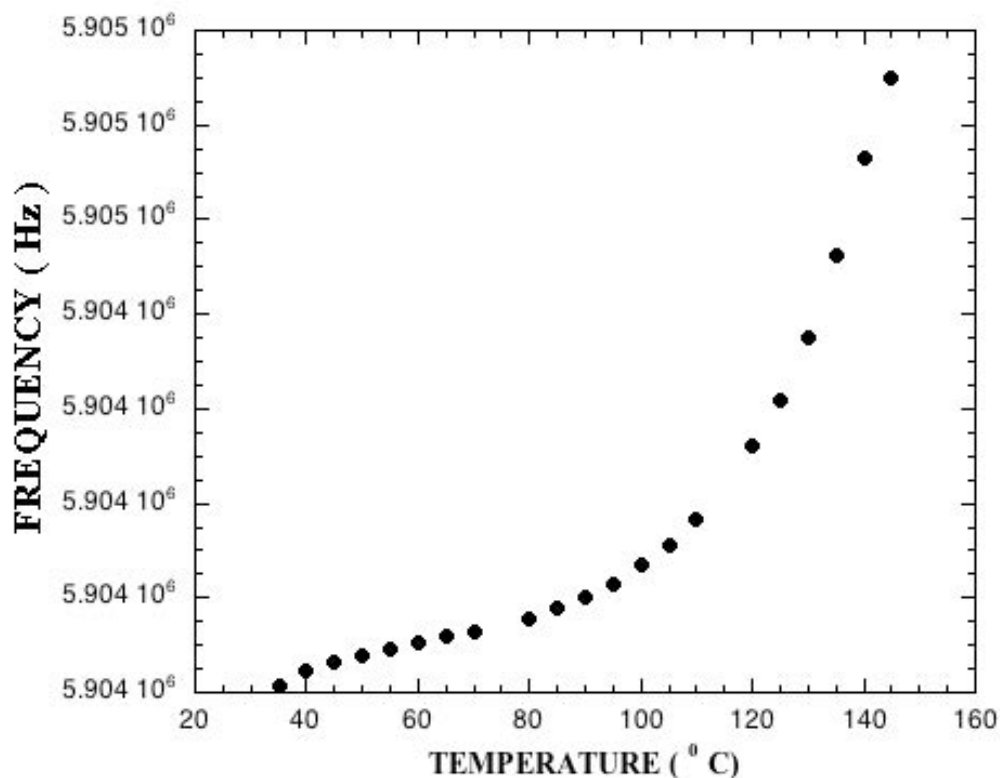
Figure 3.12 Frequency of the QCM vs. temperature.

As the temperature was raised slowly from 35 °C to 150 °C, the resonant frequency of the QCM also changes and thereby causes apparent change in mass. To ensure there is no apparent mass change induced due to temperature variation, the PID temperature controller was used to keep the reactor temperature constant (±0.05 °C) during the ALD thin film growth process. The temperature of the reactor was constantly monitored during ALD growth, using the thermocouple attached to the substrate holder.

3.9 Implementation of viscous-flow condition

In order to ensure the viscous-flow condition in the ALD reactor, the Knudsen number (Kn) has to be less than 0.01. The Knudsen number is defined as Kn= λ/D, where

λ is the mean free path of the gas molecules and D is the diameter of the tube. The mean free path λ is defined by:

$$\lambda = \frac{kT}{(2^{1/2}\sigma P)} \; ,$$

3.1

where k = Boltzmann's constant, T = Temperature, P = Pressure of the reactor tube, and σ = Collision cross section. For nitrogen gas, to ensure viscous-flow at 177 °C, P > 0.13 Torr. To ensure the sonic flow condition during introduction of precursor in the carrier gas:

$$P_p < 0.53 P_V \; ,$$

3.2

where P_p = Pressure at the downstream end of the needle valve and P_V = Vapor pressure of the precursor before entering the needle valve.

Neglecting the conductance we can write $P_p \sim P$. The water vapor pressure is ~20 Torr and DEZ vapor pressure is ~ 18 Torr. For P < 9.5 Torr both water and DEZ will satisfy the sonic flow condition according to Equation 3.2. Therefore, in order to achieve the viscous-flow condition in the ALD reactor and sonic flow condition for the precursor simultaneously, the P should be :

$$0.13 \text{ Torr} < P < 9.5 \text{ Torr}$$

3.3

For ZnO ALD growth using water and DEZ, the flow tube pressure was kept at 1 Torr using a throttle valve and MKS pressure controller. The precursor pressure pulses were

kept at 0.1 Torr using the needle valves. Figure 3.13 shows the picture of the UHV-interfaced viscous-flow ALD reactor with *in-situ* QCM.

Figure 3.13 Viscous-flow UHV-interfaced ALD reactor with *in-situ* QCM.

3.10 References

1. T. Suntola, A. J. Pakkla, and S. G. Lindfors, U.S. Patent No. 4, 389, 973 (1983).

2. T. Suntola, and J. Antson, U.S. Patent No. 4,058,430 (1977).

3. T. Suntola, J. Antson, A. J. Pakkla, and S. G. Lindfors, Soc. Information. Display Digest. **11**, 108 (1980).

4. T. Suntola, A. J. Pakkla, and S. G. Lindfors, U.S. Patent No. 4,413,022 (1983).

5. T. Suntola, Thin Solid Films **216**, 84 (1992).

6. T. Suntola, Matter. Sci. Rep. **4**, 216 (1989).

8. T. Suntola, and J. Hyvärinen, Annual Review of Material Science **15**, 177 (1985).

9. G. Stuyven, P. D. Visschchere, K. Neyts, and A. Hikavvy, Jpn. J. Appl. Phys. **41**, 5702 (2002).

10. P. D. Rack, and P. H. Holloway, Matter. Sci. Eng. **R21**, 171 (1998).

11. < www.sci.fi/~suntola/ald.presentations.html >.

12. M. L. Green, E. P. Gusev, R. Degraeve, and E. L. Garfunkel, J. Appl. Phys. **90**, 2057 (2001).

13. J. W. Klaus, and S. M. George, Surf. Sci. **447**, 81 (2000).

14. J. W. Klaus, O. Sneh, and S. M. George, Science **278**, 1934 (1997)

15. M. Ritala, T. Asikainen, and M. Leskelä, Electrochem. Solid-State Lett. **1**, 156 (1998).

16. R. Matero, M. Ritala, M. Leskelä, T. Salo, J. Aromaa, and O. Forsen, J. Phys. IV **9**, 493 (1999).

17. S. Zaitsu, T. Jitsuno, M. Nakatsuka, T. Yamanaka, and S. Motokoshi, Appl. Phys. Lett. **80**, 2442 (2002).

18. F. H. Fabreguette, R. A. Wind, and S. M. George, Appl. Phys. Lett. **88**, 013116 (2006).

19. J. J. Wang, X. Deng, R. Varghese, A. Nikolov, P. Sciortino, F. Liu, and, L. Chen, Optics Lett. **30**, 1864 (2005).

20. J. S. King, E. Graugnard, and C. J. Summers, Appl. Phys. Lett. **88**, 081109 (2006).

21. J. W. Elam, D. Routkevitch, and S. M. George, J. Electrochem. Soc. **150**, G339 (2003).

22. J. A. Delft, D. Garcia-Alonso, and W. M .M. Kessels, Semicond. Sci. Technol. **27**, 074002 (2012).

23. X. Du, Y. Du, and S. M. George, J. Phys. Chem. A **112**, 9211 (2008).

24. X. Meng, X. Yang, and X. Sun, Adv. Matter **24**, 3589 (2012).

25. M. Leskelä, and M. Ritala, J. Phys. IV **9**, Pr8-837 (1999).

26. T. M. Mayer, J. W. Elam, S. M. George, P. G. Kotula and R. S. Goeke, Appl. Phys. Lett. **82**, 2883 (2003).

27. A. Paranjpe, S. Gopinath, T. Omstead, and R. Bubber, J. Electrochem. Soc. **148**, G465 (2001).

28. M. Cassir, A. Ringuedé, and L. Niinistö, J. Mater. Chem. **20**, 8987 (2010).

29. K. Park, Y. Lee, K. T. Im, J. Y. Lee, and S. Lim, Thin Solid Film **518**, 4126 (2010).

30. R. J. Narayan, S. P. Adiga, M. J. Pellin, L. A. Curtiss, S. Stafslien, B. Chisholm, N. A. Monteiro-Riviere, R. L. Brigmon, and J. W. Elam, Materials Today **13**, 60 (2010).

31. S.M. George, Chem. Rev. **110**, 111 (2010).

32. J. W. Elam, and S. M. George, Chem. Mater. **15**, 1020 (2003).

33. T. Suntola, Handbook of Crystal Growth 3, Thin Films and Epitaxy, Part B: Growth Mechanisms and Dynamics, Chapter 14, Elsevier Science Publishers B.V. (1994).

34. E. Granneman, P. Fischer, D. Pierreux, H. Terhorst, and P. Zagwijn, Surface & Coatings Technology **201**, 8899 (2007).

35. J. W. Elam, M. D. Groner, and S. M. George, Rev. Sci Instrum. **73,** 2981 (2002).

36. J. W. Elam, and M. J. Pellin, Anal. Chem. **77**, 3531 (2005).

Chapter 4

Growth of ZnO thin films on polar (√3×√3)R30° reconstructed and unreconstructed MgO(111) surfaces by atomic layer deposition

Abstract

This chapter outlines how ZnO thin films were grown on polar (√3×√3)R30° reconstructed and unreconstructed MgO(111) surfaces using the viscous-flow atomic layer deposition reactor, which was described in Chapter 3. Growth studies of ALD ZnO thin films by *in-situ* QCM, structural studies from XRD, chemical composition studies by XPS, and optical properties studies by UV-Visible spectroscopy are also discussed in detail.

4.1 Introduction

ZnO thin films have recently attracted a large amount of attention due to optoelectronic device, laser diode, and UV-light emitting diodes applications [1-3]. However, lack of p-type ZnO has fueled research in the field of ZnO-based heterostructures. ZnO/Si, ZnO/GaN, ZnO/SiC are a few of the most promising heterostructures for LED device application [4-7]. The epitaxial growth on Si is nearly impossible due to the large lattice mismatch between Si and ZnO (~15%). Efforts have been made to grow high-quality ZnO thin films using pulsed laser deposition, thermal evaporation, sputtering, electrochemical deposition, molecular beam epitaxy, metal organic chemical vapor deposition and most recently using novel atomic layer deposition [8-20]. Recently MgO(111) buffer layers were used to improve the epitaxy of ZnO thin films [21]. However, the fundamental growth mechanism is not fully understood. Growth of ZnO on MgO single crystals has never been investigated with atomic layer deposition.

ZnO and MgO have a moderate lattice mismatch (~8.4%). Because of this, a compressive stress is produced during ZnO growth. For MgO substrates, this stress is much less than the higher lattice mismatch substrate (e.g. Si). This also helps to reduce the dislocation defect density of the ZnO films grown over MgO(111). The MgO(111) surface has hexagonal symmetry, so ZnO, which has wurtzite structure, can grow epitaxially on this surface. We have grown ZnO on polar MgO(111) surfaces using atomic layer deposition. In atomic layer deposition, the thin film growth occurs in layer-by-layer mode within the ALD temperature window. We are interested to know whether ZnO grows epitaxially on MgO(111) single crystals in atomic layer deposition.

Initial surface termination plays an important role during thin film growth using ALD. If the initial starting substrate is not OH-terminated, an incubation period is reported in ALD film growth [22]. We have grown ZnO films on two different MgO(111) surfaces, viz., MgO(111)-(1x1) and ($\sqrt{3}\times\sqrt{3}$)R30° reconstructed. Both surfaces have different termination. The MgO(111)-(1x1) is believed to be OH-terminated while the ($\sqrt{3}\times\sqrt{3}$)R30° reconstructed surface is believed to be cyclic ozone terminated or Mg-terminated [23-27]. Here we have investigated how ZnO grows on these two different surfaces by atomic layer deposition.

4.2 Preparation of MgO(111) substrates

Two double-sided-polished MgO(111) (10x10x1 mm^3) single crystals with purity of 99.99% were obtained from Crys Tec. The crystals were sonically cleaned for 15 min in a bath of acetone and then another 15 min in methanol. Finally, the crystals were rinsed with methanol and dried by flowing nitrogen. Following the cleaning, two MgO(111) crystals were placed face to face and placed in between two MgO(100) samples for protection. These stacked MgO crystals were placed in an alumina crucible. The crucible was then loaded into a tube furnace. This geometry allows the polar faces of the MgO(111) substrates to remain in quasi-equilibrium with their vapor while annealing inside the tube furnace. MgO(111) crystals were annealed at 600°C for 12 hours in air to obtain (1x1)-OH terminated surfaces [28]. The MgO(111)-($\sqrt{3}$x$\sqrt{3}$)R30° reconstructed surfaces were produced by annealing at 1000°C for 36 hours in air [29].

4.3 LEED Results

After annealing, low energy electron diffraction (LEED) analysis in a VG Mk. II ESCALab ultrahigh vacuum (UHV) chamber was performed. Figure 4.1(a) shows the typical LEED pattern for unreconstructed MgO(111)-(1x1) and Figure 4.1(b) shows its schematic.
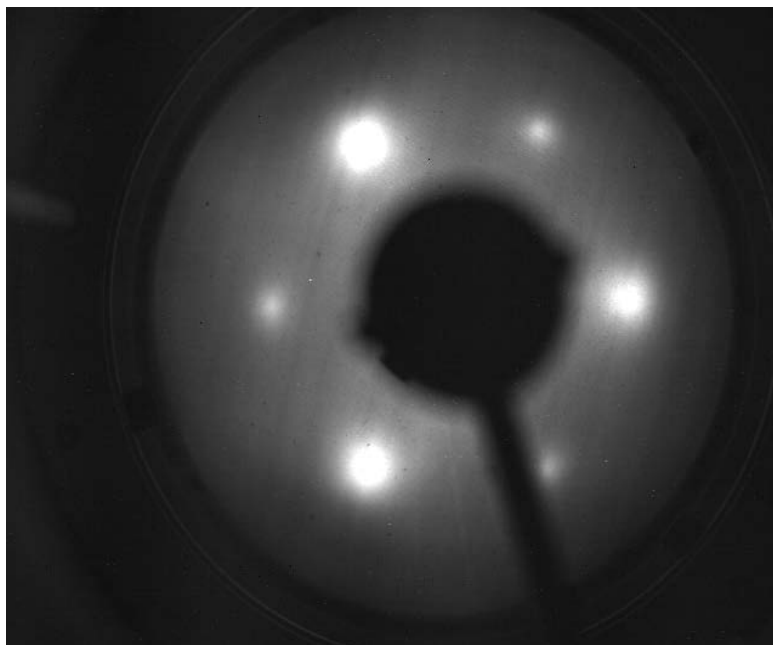
Figure 4.1 (a) LEED pattern of a MgO(111)-(1x1) surface at 100 eV.
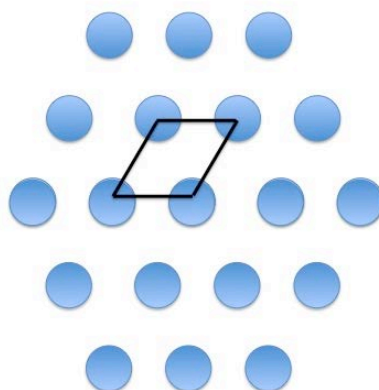
Figure 4.1 (b) Schematic diagram of LEED pattern for MgO(111)-(1x1) surfaces
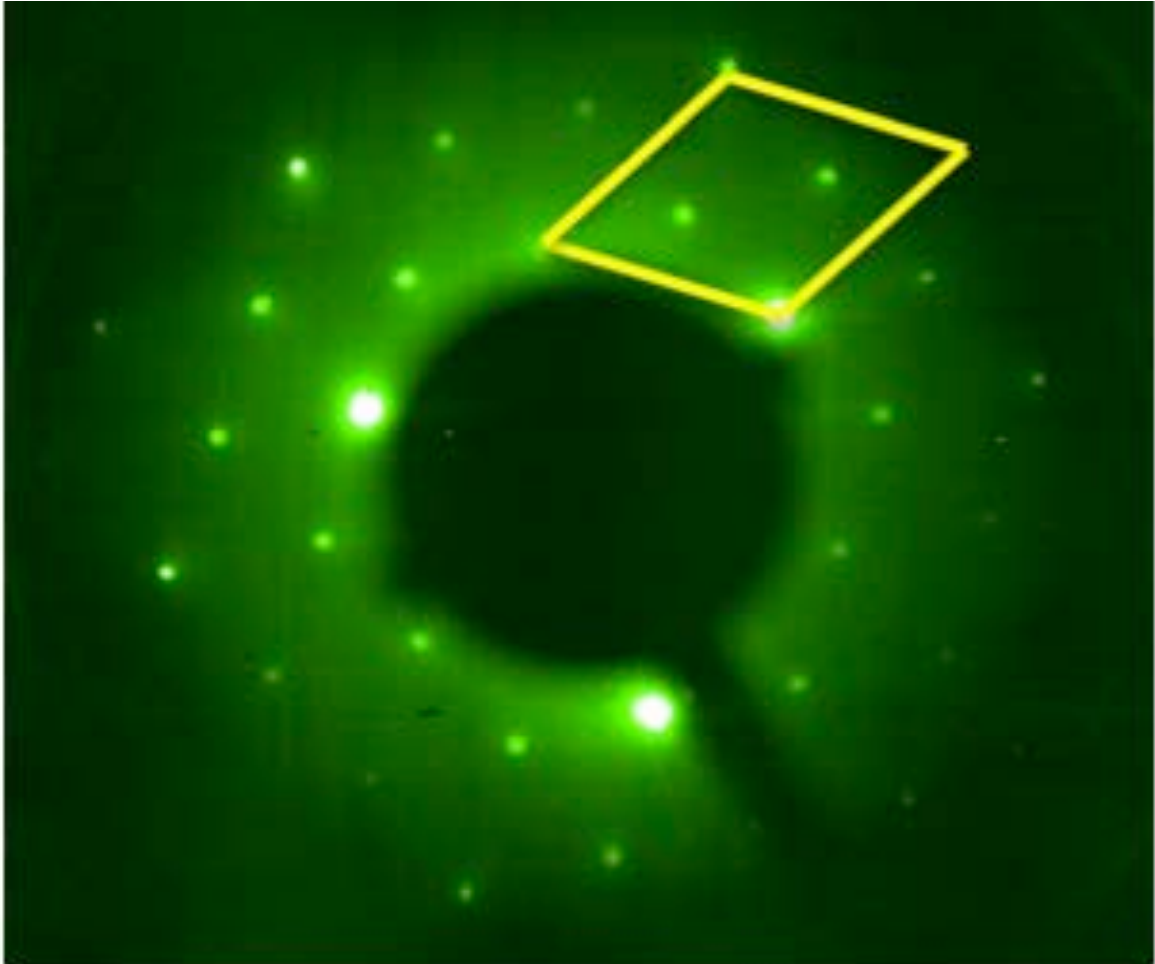
Figure 4.2 (a) LEED pattern of reconstructed MgO(111)-(√3x√3)R30° at 118 eV. The brightest spots arise from the substrate, and the other spots are due to the (√3x√3)R30° reconstruction. A (1x1) unit cell is outlined for reference.

The bright spots correspond to the pattern of electrons diffracted elastically at the surface; the reconstruction results in appearance of new spots in addition to those due to the substrate. In Figure 4.2 (a), a schematic (1x1) unit cell identifies the bright substrate

spots and somewhat dimmer superstructure spots arising from the MgO(111)-(√3x√3)R30° reconstruction.
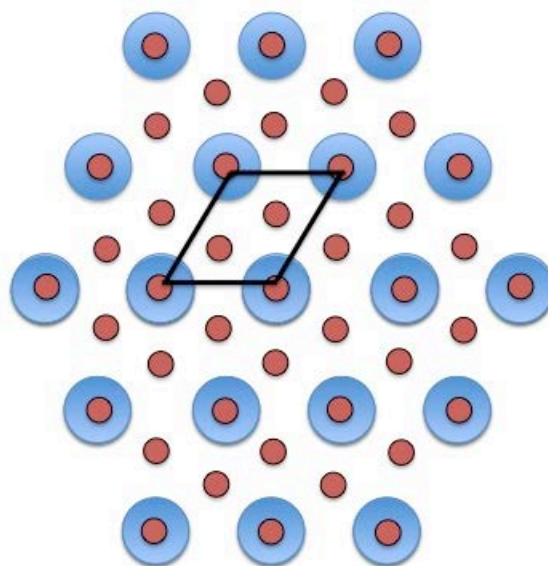
Figure 4.2 (b) Schematic of LEED pattern for the MgO (111)-(√3x√3)R30° surface reconstruction. Blue dots represent the bulk periodicity and black represent the surface contribution.

4.4 *In-situ* QCM results of ALD ZnO growth

Diethyl zinc (DEZ) (96%) from Strem Chemical Inc. and deionized ultra filtered water from Fisher Scientific were exposed alternately to achieve ZnO ALD. The ALD

cycle is expressed as $t_1+t_2+t_3+t_4$ where t_1 is DEZ exposure time, t_2 is nitrogen purge time, t_3 is water exposure time, and t_4 is nitrogen purge time. Once the MgO(111) substrates were loaded into the ALD reactor, ZnO ALD thin films were grown by alternating exposure of DEZ and H_2O for different temperatures and cycle times. *In-situ* QCM measurements were performed during the film growth. During ALD film growth, the back surface of the QCM sensor was purged with ~ 20 sccm UHP nitrogen to prevent any ZnO film growth on it.

Using *in-situ* QCM, we have observed a linear step-like ZnO ALD growth. Figure 4.3 shows such a linear growth for typical growth conditions. For this ZnO growth, 130° C temperature and 4-10-4-10s ALD cycle times were employed. From linear regression of this QCM data and assuming the ZnO bulk density 5.61 g/cm^3, we found the average growth per cycle is ~2.3 Å. Figure 4.4 shows a few such typical cycles. From this graph, it can be inferred that almost all the mass is deposited during the DEZ pulse, with little mass change upon exposure to H_2O. This result is also in agreement with already published results [30-33].
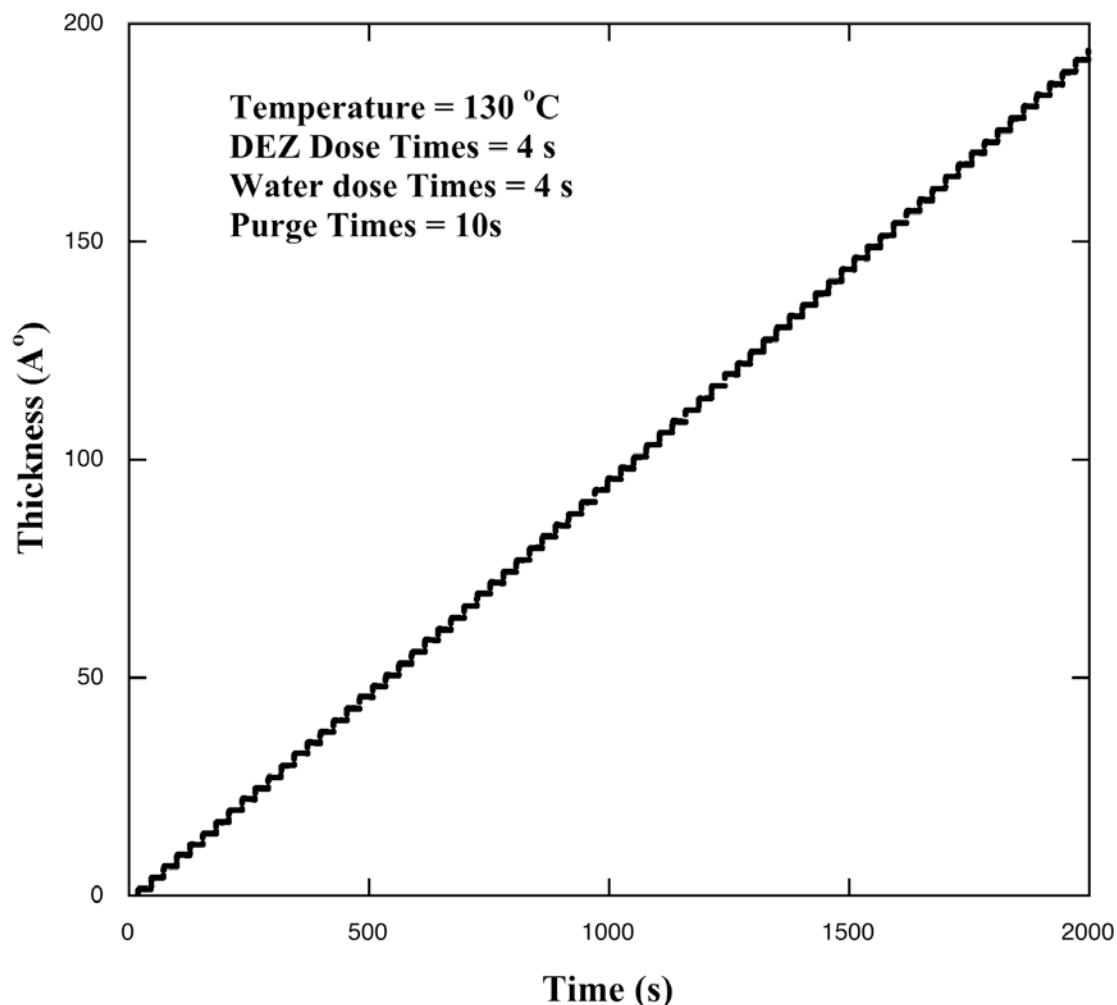
Figure 4.3 QCM thickness measurements vs. time during ZnO ALD growth.

ALD is characterized by self-limiting chemical reactions. This property of ALD was investigated by using *in-situ* QCM by keeping the water pulse duration constant and changing DEZ pulse duration. Figure 4.5 shows the effect of ZnO growth rate at 130°C with ALD cycle x+5+2+5 s, where x is the DEZ pulse duration. We found the growth per cycle reaches saturation for DEZ pulse durations greater than 2 s, and little to no growth was observed for exposure less than 1s. Similarly the influence of water pulse time is

shown in Figure 4.6 In these experiments, the temperature was kept at 130°C and the ALD cycle time was $3+5+x+5$ s, where x is the water pulse duration. This graph is very similar to DEZ pulse duration vs. growth rate. A water exposure of 1 s duration was needed to reach saturation. For the initial 100 cycles, the growth rate was observed to be ~1.7 Å /cycle. Eventually, the growth rate increased to 2.3 Å/cycle. The initial growth rate can be attributed to the nucleation period for ZnO ALD growth on gold plated QCM. The later growth rate of 2.3 Å/cycle is concordant with previously published work [30-33].
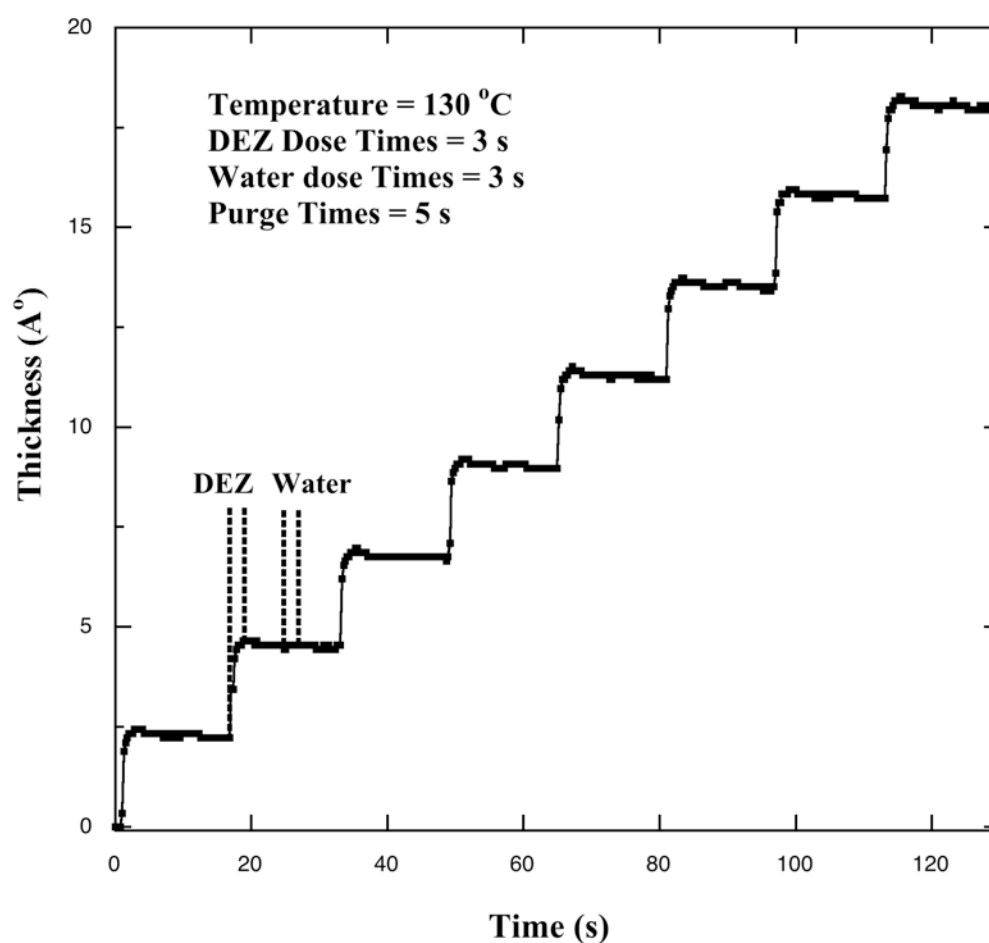
Figure 4.4 Typical single-cycle QCM thickness measurements vs. time during ALD ZnO growth.
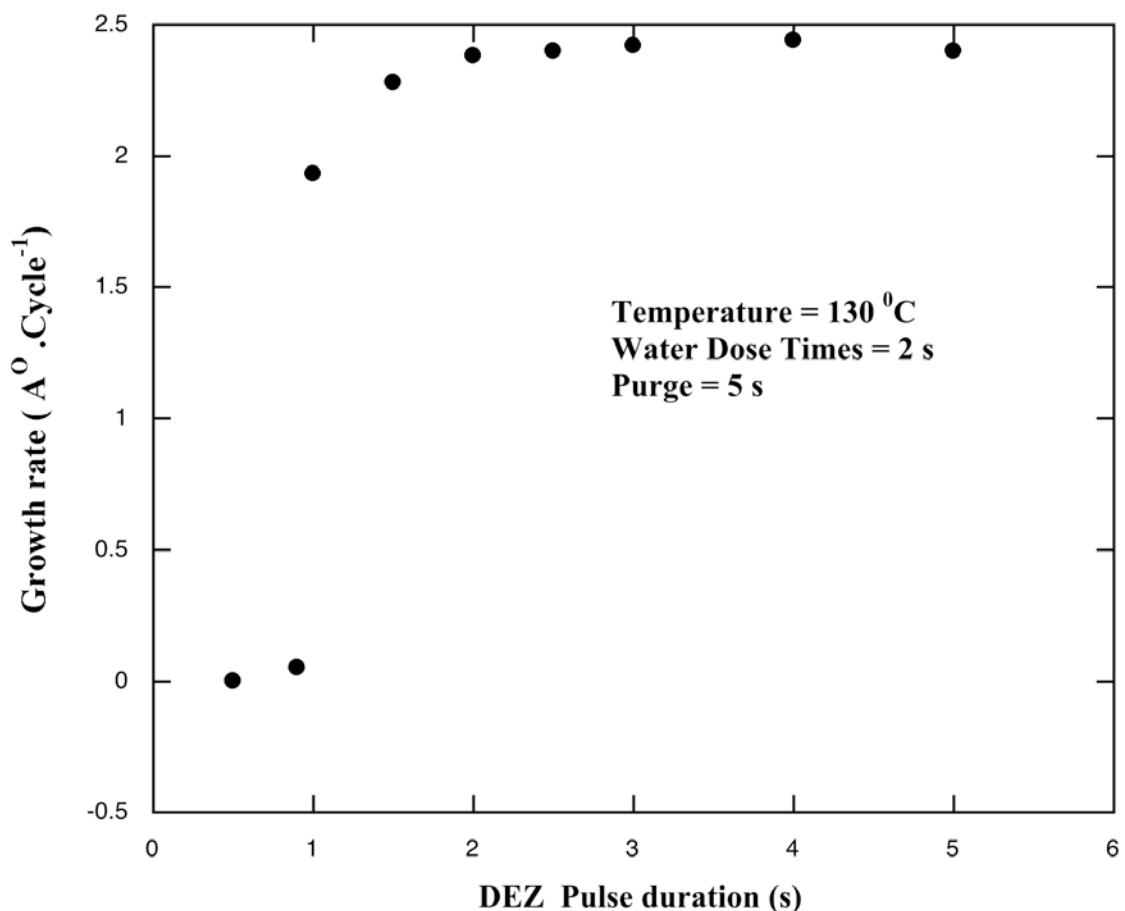
Figure 4.5 Growth rate of ZnO as function of DEZ pulse cycle time.

We also investigated the dependence of the average growth rate per cycle of ZnO ALD on reaction temperature, as shown in Figure 4.7. There is a temperature "window" in which ALD growth shows near-ideal behavior. At lower temperatures, insufficient thermal energy is available for the reactions to proceed. At higher temperatures, adsorbed molecules and/or the previously deposited film constituents may decompose. In the

present case, we found a window from about 130 to 170°C where good, self-limited ZnO

growth may take place [17, 30-33].
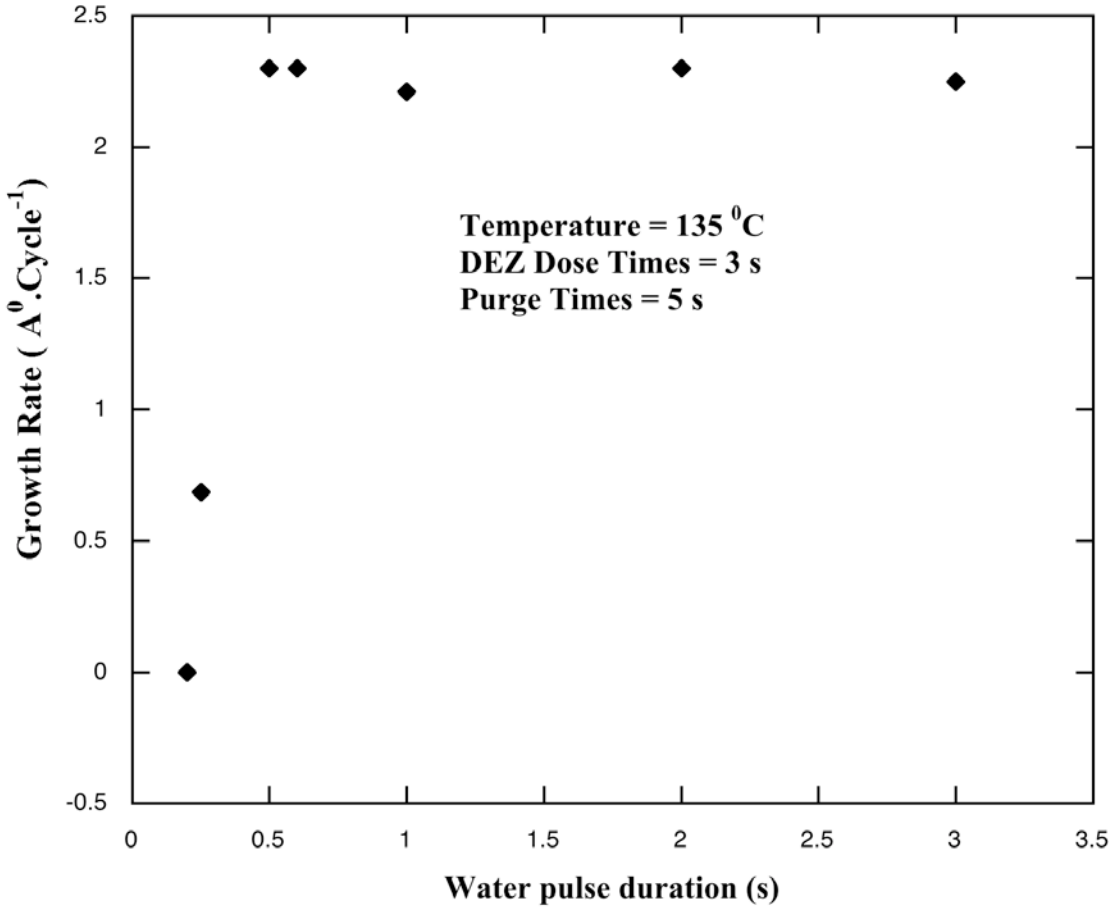
Figure 4.6 Growth rate of ZnO as function of water pulse cycle time.
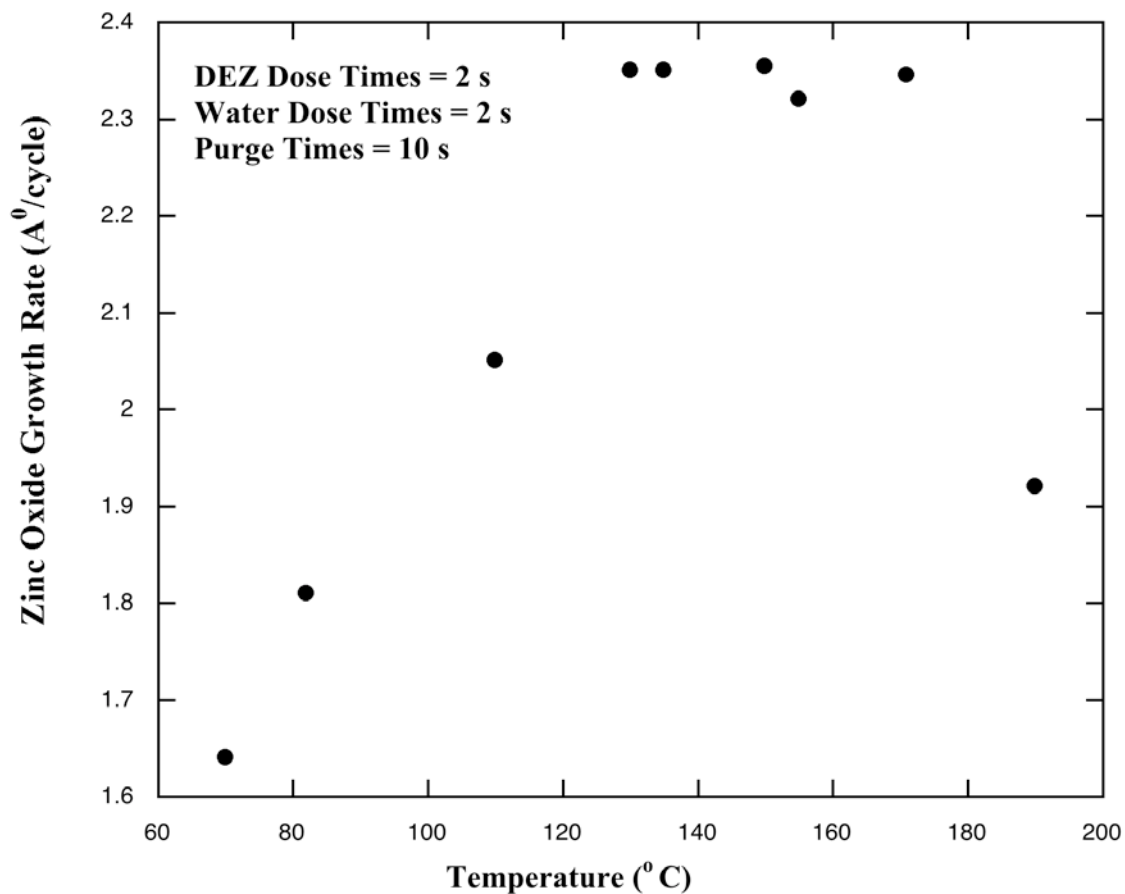
Figure 4.7 Dependence of growth rate per cycle of ZnO films as function of ALD growth temperature.

4.5 AFM analysis of polar MgO(111) substrates and ZnO films

AFM studies were performed on polar MgO(111) surfaces to observe how the surface morphology evolves with time while annealing. It is very important to know the initial surface morphology before ALD ZnO films were grown over the substrates. All AFM measurements were performed in contact mode using SiC AFM tip. Figure 4.8 represents the morphological evolution of MgO(111) surfaces after annealing at 1000°C.

Figure 4.8 (a) shows the as-received surface where scratches from mechanical polishing are clearly visible. The RMS roughness of the as-received samples was ~ 2 nm.
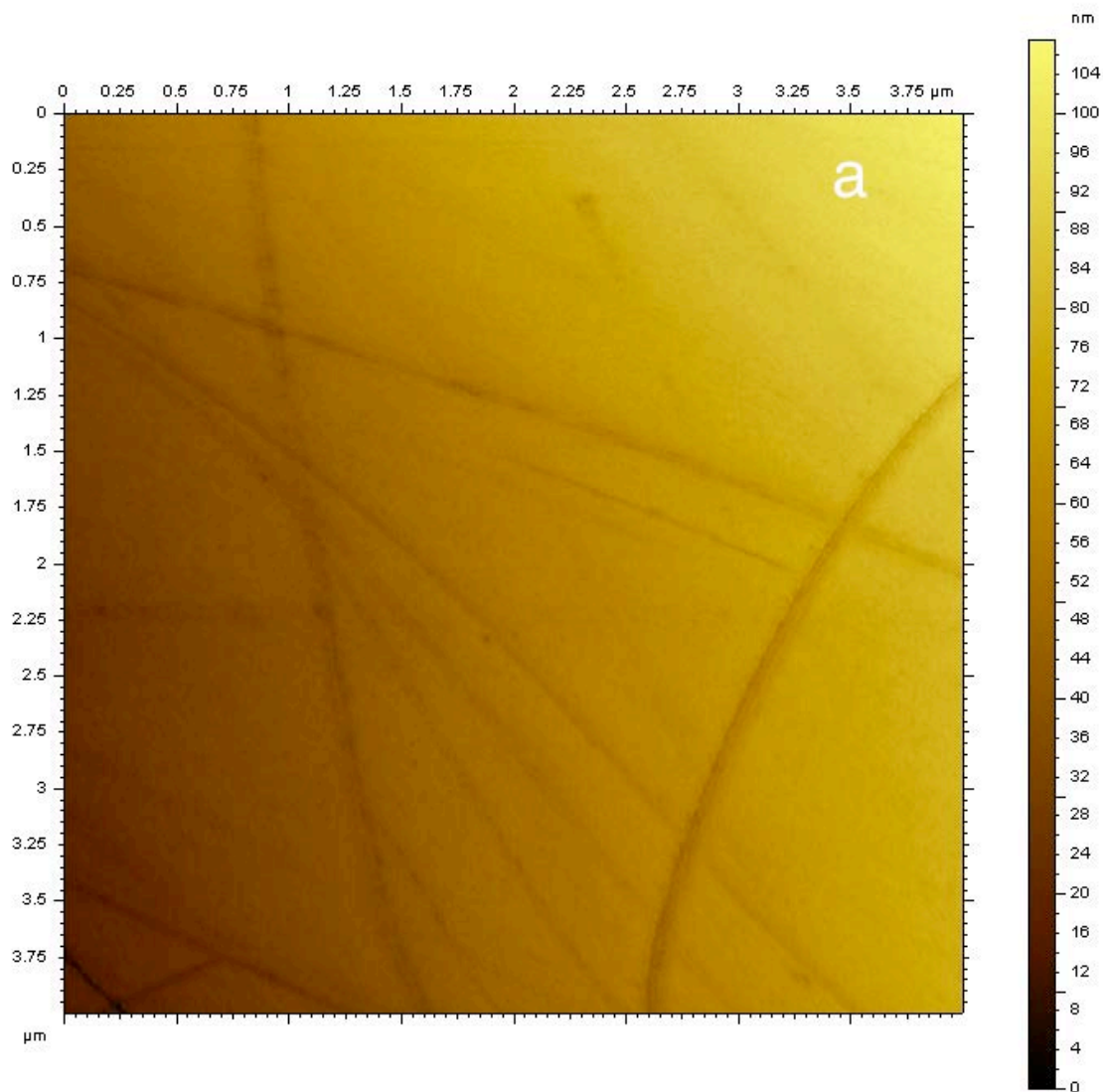
Figure 4.8 (a) as-received MgO(111) surface.

After 10 hours of annealing, the surface has become very rough, with RMS roughness of 20 nm [Figure 4.8 (b)]. The surface roughness can be attributed to mass transport on the surface at this higher temperature.
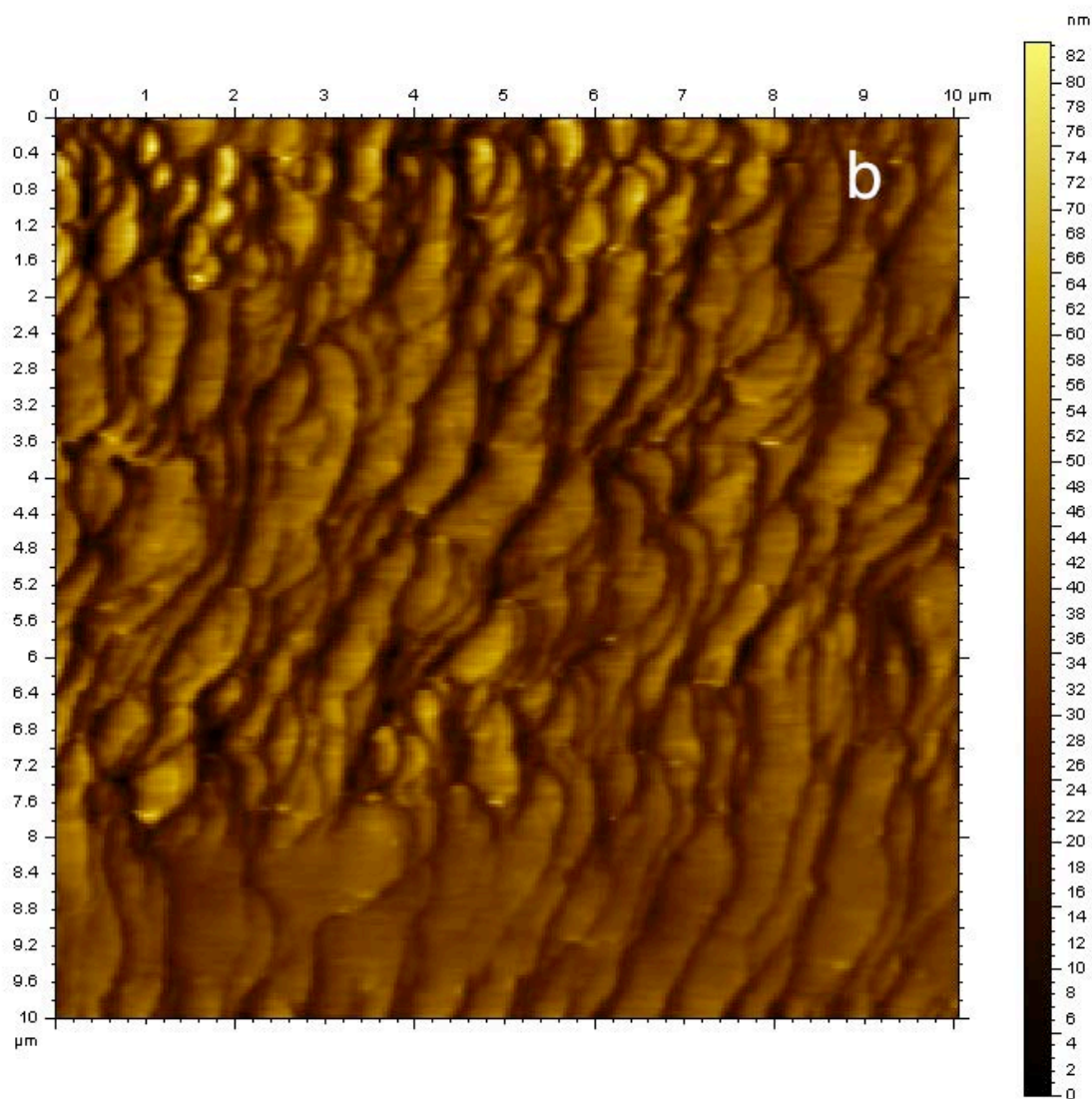
Figure 4.8 (b) AFM image of MgO(111) substrate after annealing at 1000°C for 10 hours.

Upon annealing for 36 hours, nearly perfect atomically flat 60° triangular terraces were observed [Figure 4.8 (c)]. In the rocksalt structure, the step edges bordering a (111) triangular terrace will be terminated with the same atomic species. Therefore, if the lowest-energy step edge is terminated with, say, O, then all the step edges of a triangular terrace will share that O termination. This observation can explain why triangular terraces are favored. The RMS roughness of this surface is found to be 0.9 nm and the step heights of the terraces are ~ 0.5 nm.
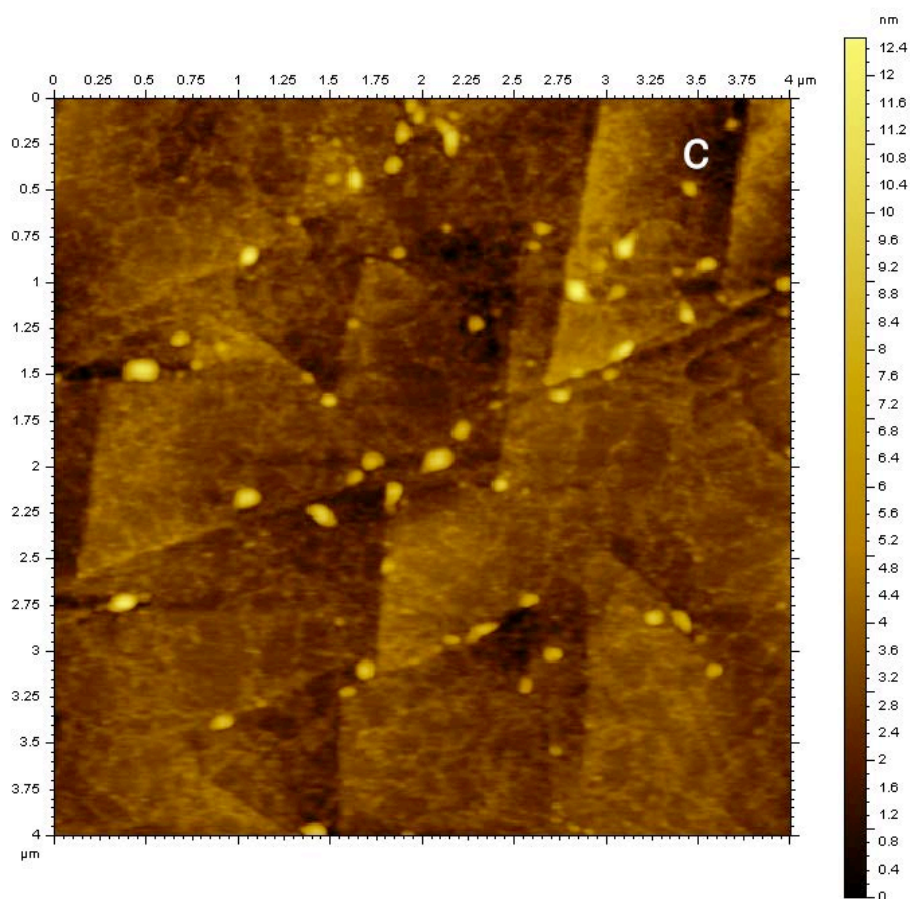
Figure 4.8 (c) AFM image of reconstructed MgO(111)-($\sqrt{3}$x$\sqrt{3}$)R30° after annealing at 1000°C for 36 hours.
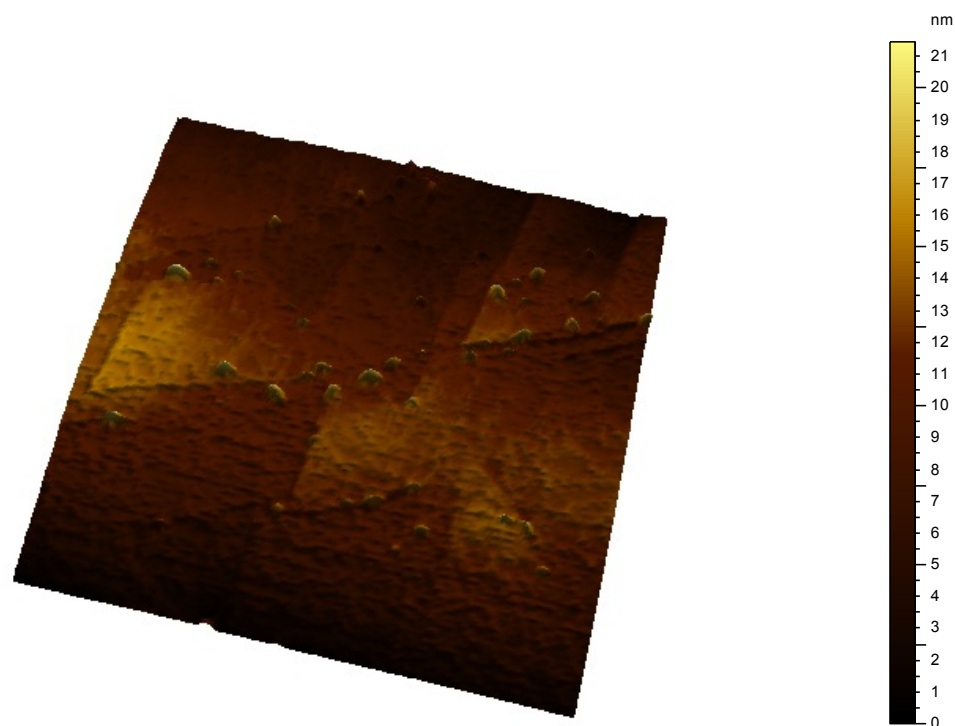
Figure 4.8 (d) Three-dimensional AFM image of reconstructed MgO(111)-($\sqrt{3}$x$\sqrt{3}$)R30°
after annealing at 1000°C for 36 hours. Triangular terraces are clearly visible in the
image.

The MgO(111)-(1x1) surfaces were made by annealing at 600°C for 12 hours. The
RMS roughness of such surfaces was found to be 2 nm. Figure 4.9 shows an AFM image
of such surfaces. The AFM studies shows the reconstructed MgO(111) is a little smoother
than the unreconstructed MgO(111) surfaces.
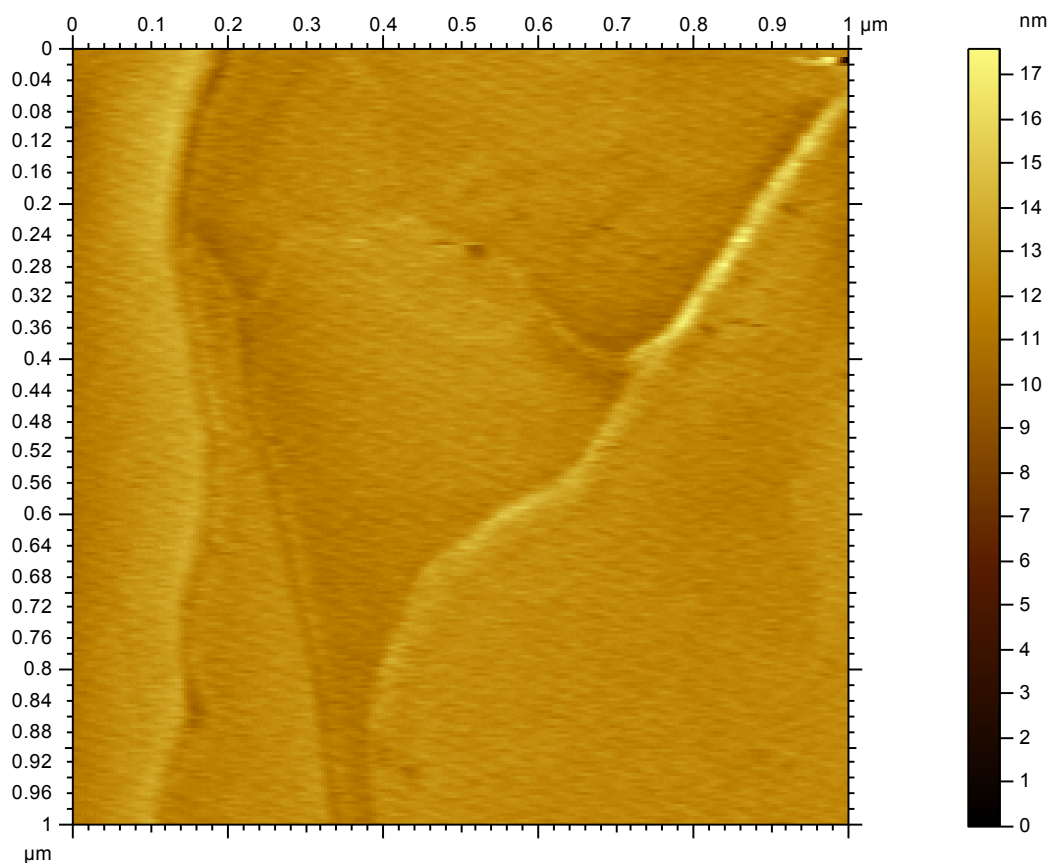
Figure 4.9 AFM image of MgO(111)-(1x1) substrate after annealing at $600°C$ for 12 hours.

After preparing the unreconstructed MgO(111)-(1x1) and reconstructed MgO(111)-($\sqrt{3}$x$\sqrt{3}$)R30° surfaces, substrates were loaded into the ALD reactor for ZnO thin films growth over them. After growth, AFM was used in contact mode to find the surface roughness and morphology of ALD ZnO thin films grown on MgO(111)-($\sqrt{3}$x$\sqrt{3}$)R30° and MgO(111)-(1x1) as a function of ALD cycles. AFM scans for different thicknesses of ZnO thin film were made on same substrate by stopping the ALD growth. Figure 4.10 shows a 1 μm x 1 μm AFM scan of ZnO films of different thicknesses grown

at 130°C on MgO(111)-(1x1) with ALD cycle time 3+5+3+5 s. Figure 4.11 shows similar scans for ZnO grown on reconstructed MgO(111)-($\sqrt{3}$x$\sqrt{3}$)R30° substrates. Polycrystalline ZnO with grain size of 30-80 nm was observed in the AFM scans.
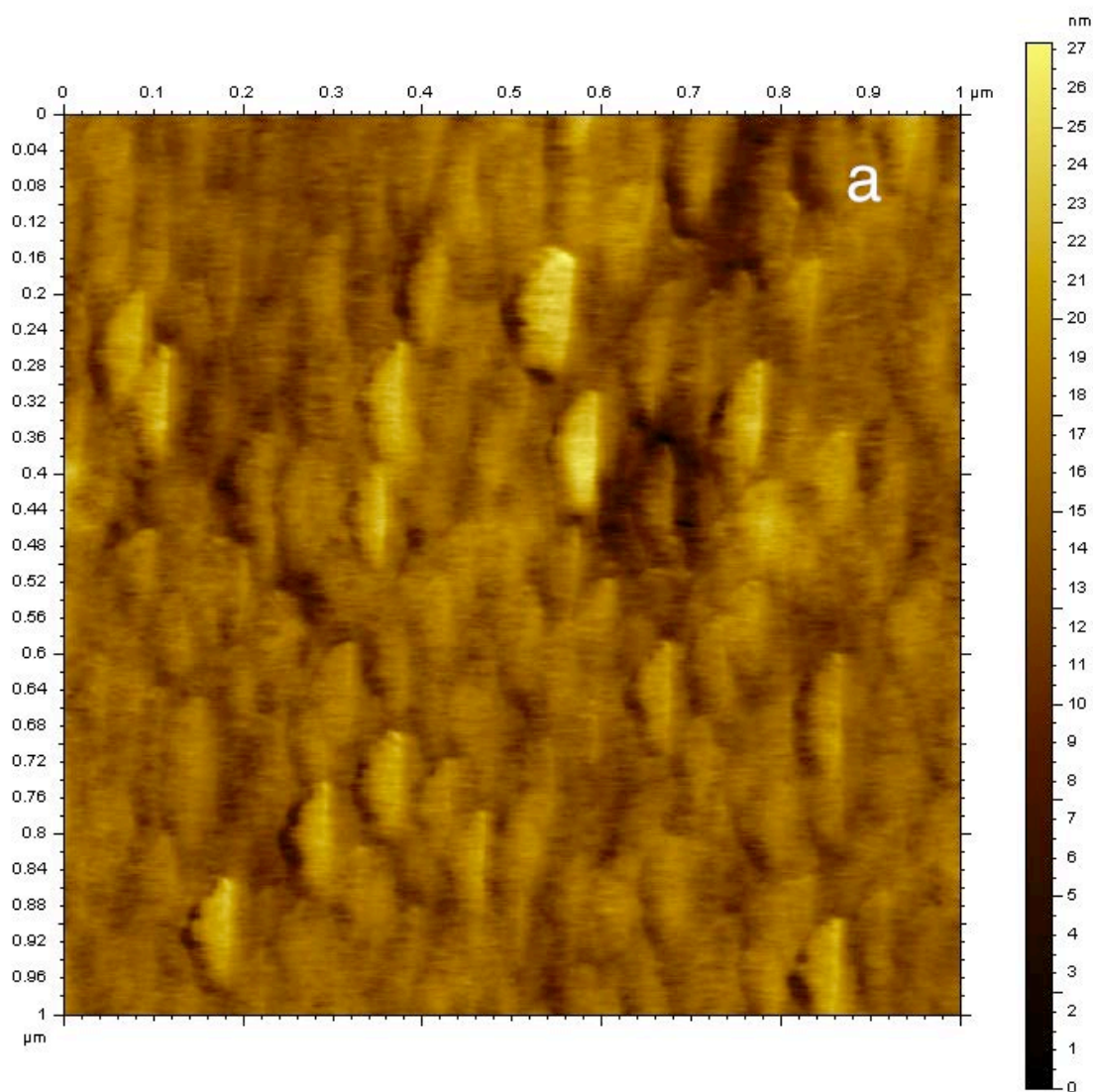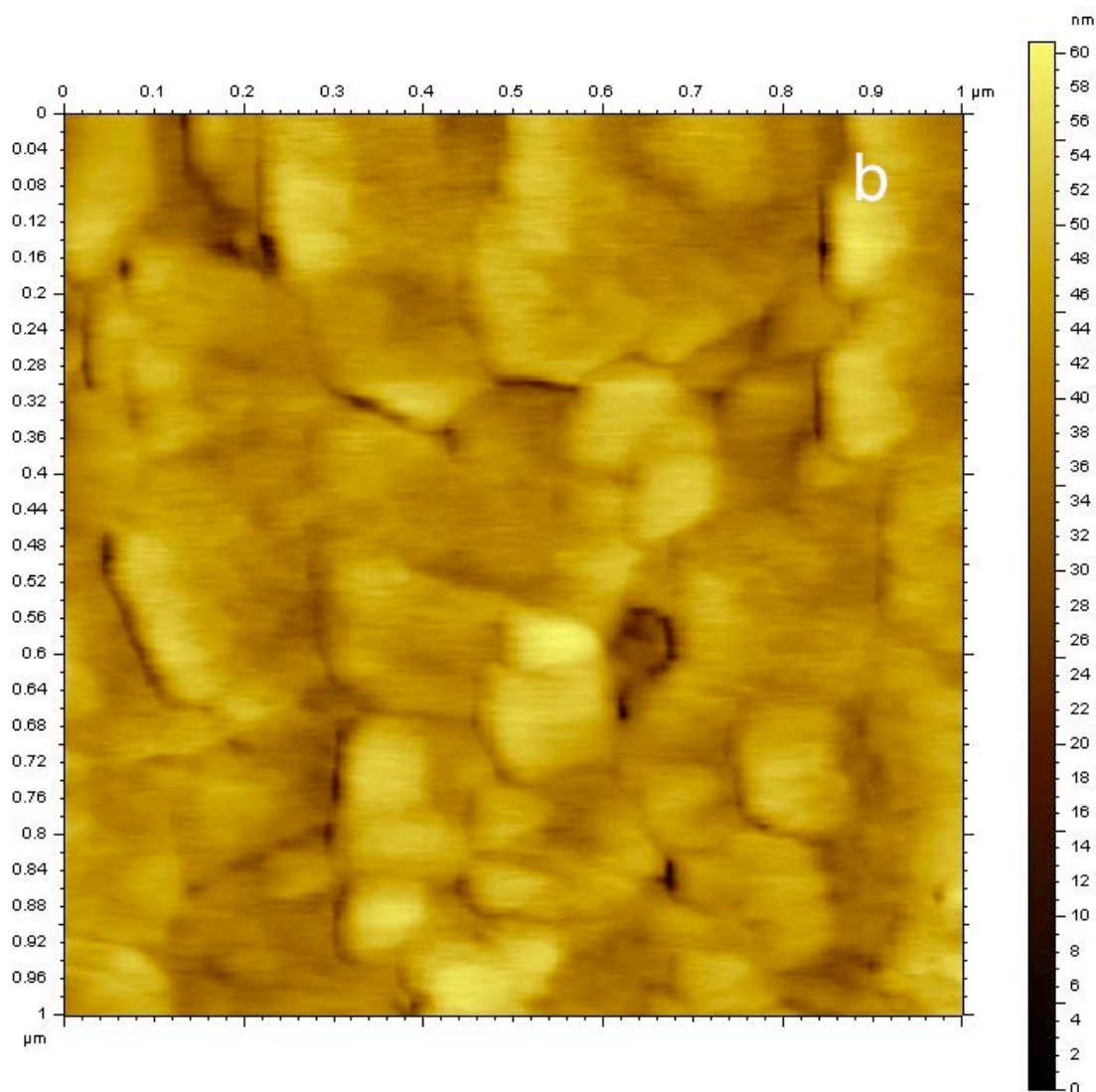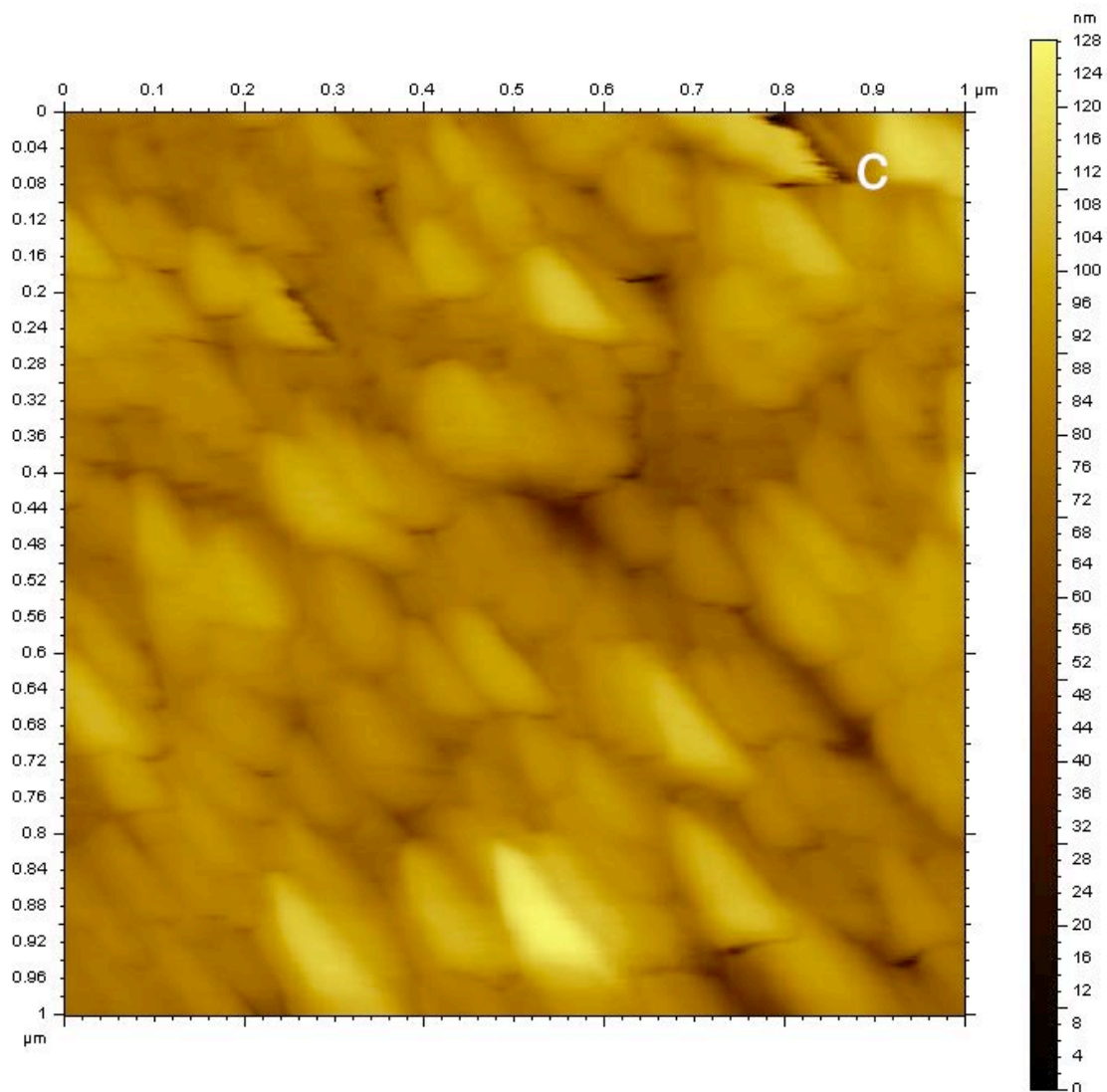
Figure 4.10 Height image of AFM scans (1 μm x 1 μm) of ALD ZnO films grown on unreconstructed MgO(111)-(1x1) substrates at 130°C for (a) 200 cycles, (b) 400 cycles, (c) 1000 cycles.
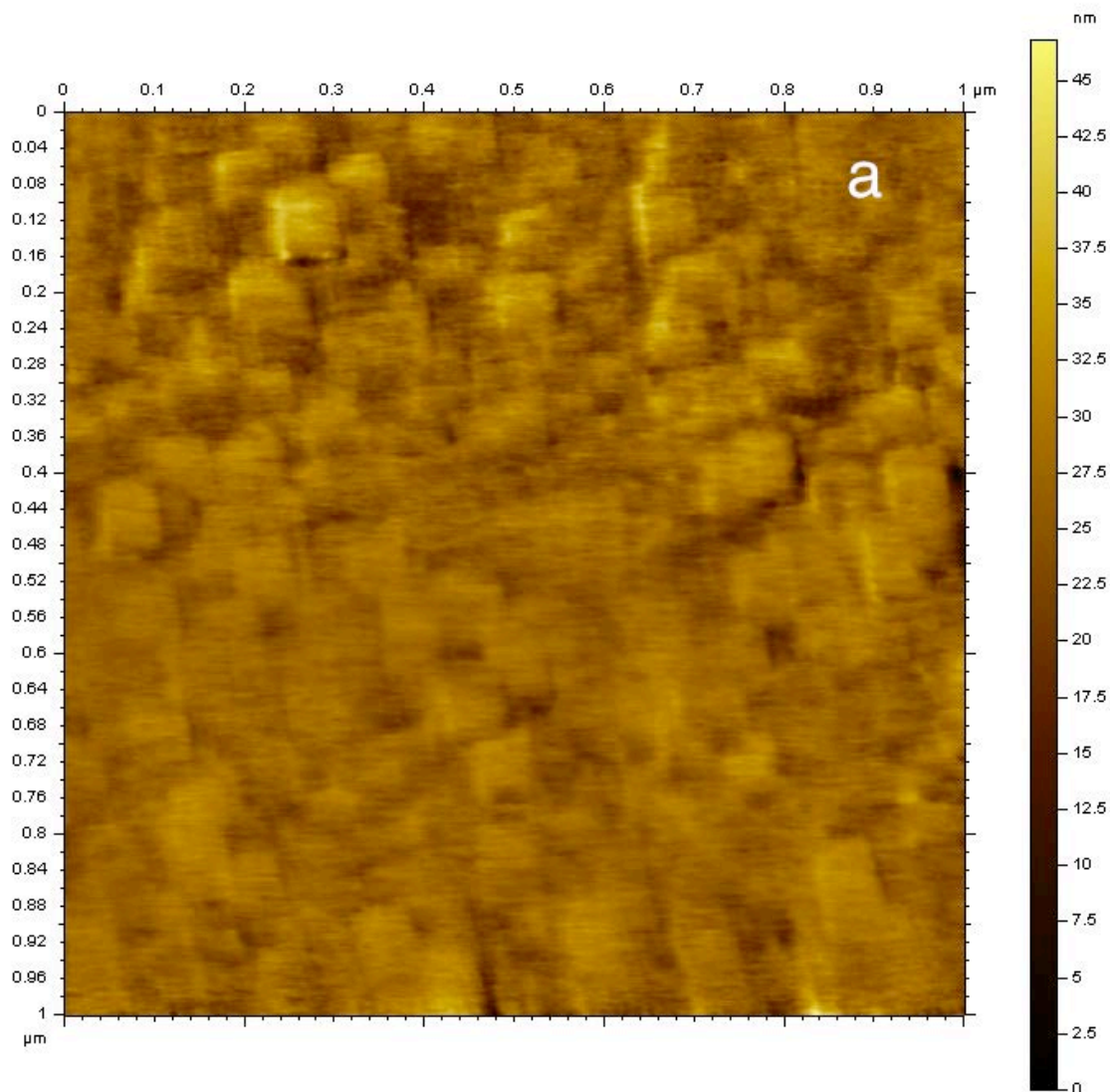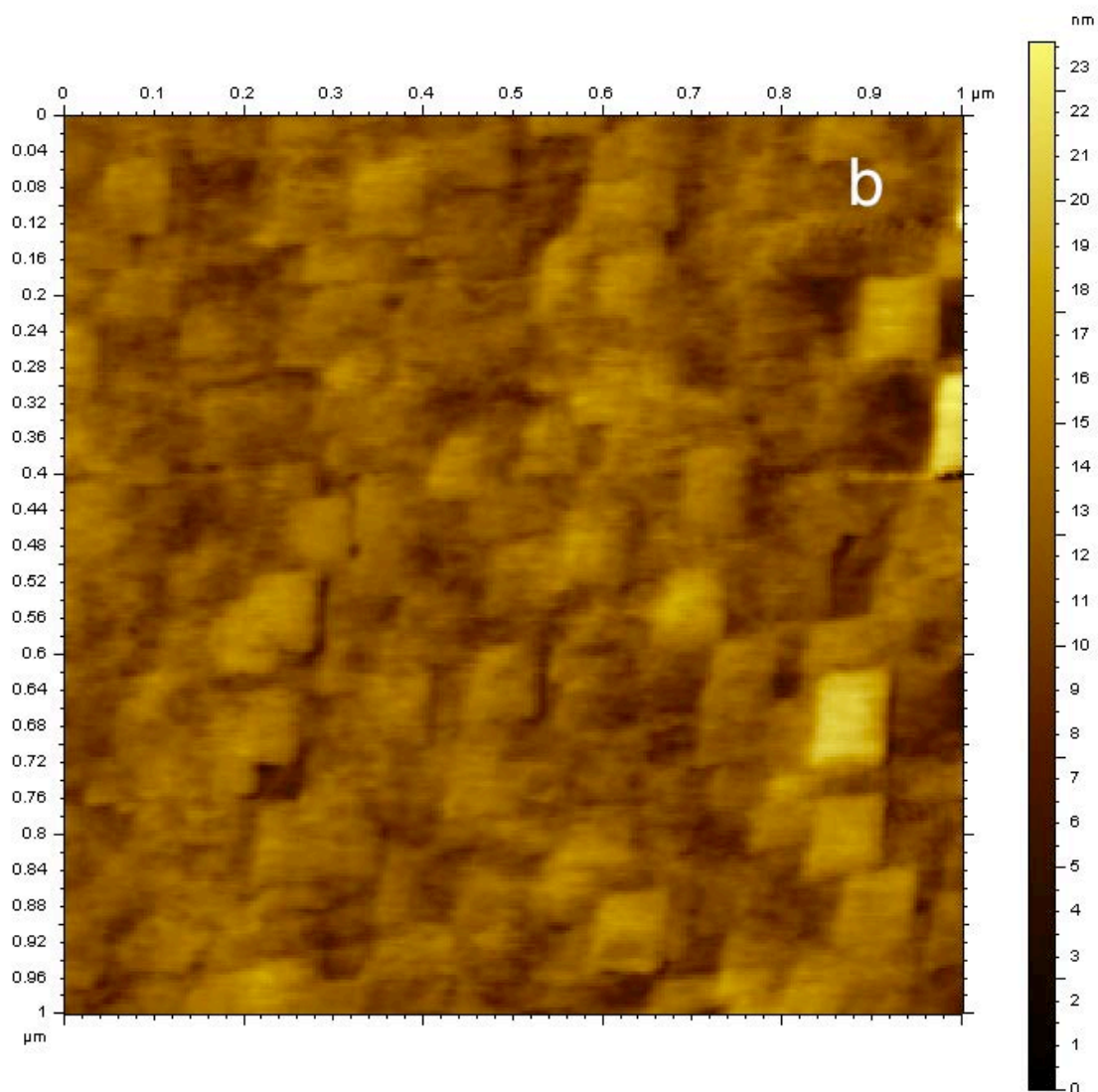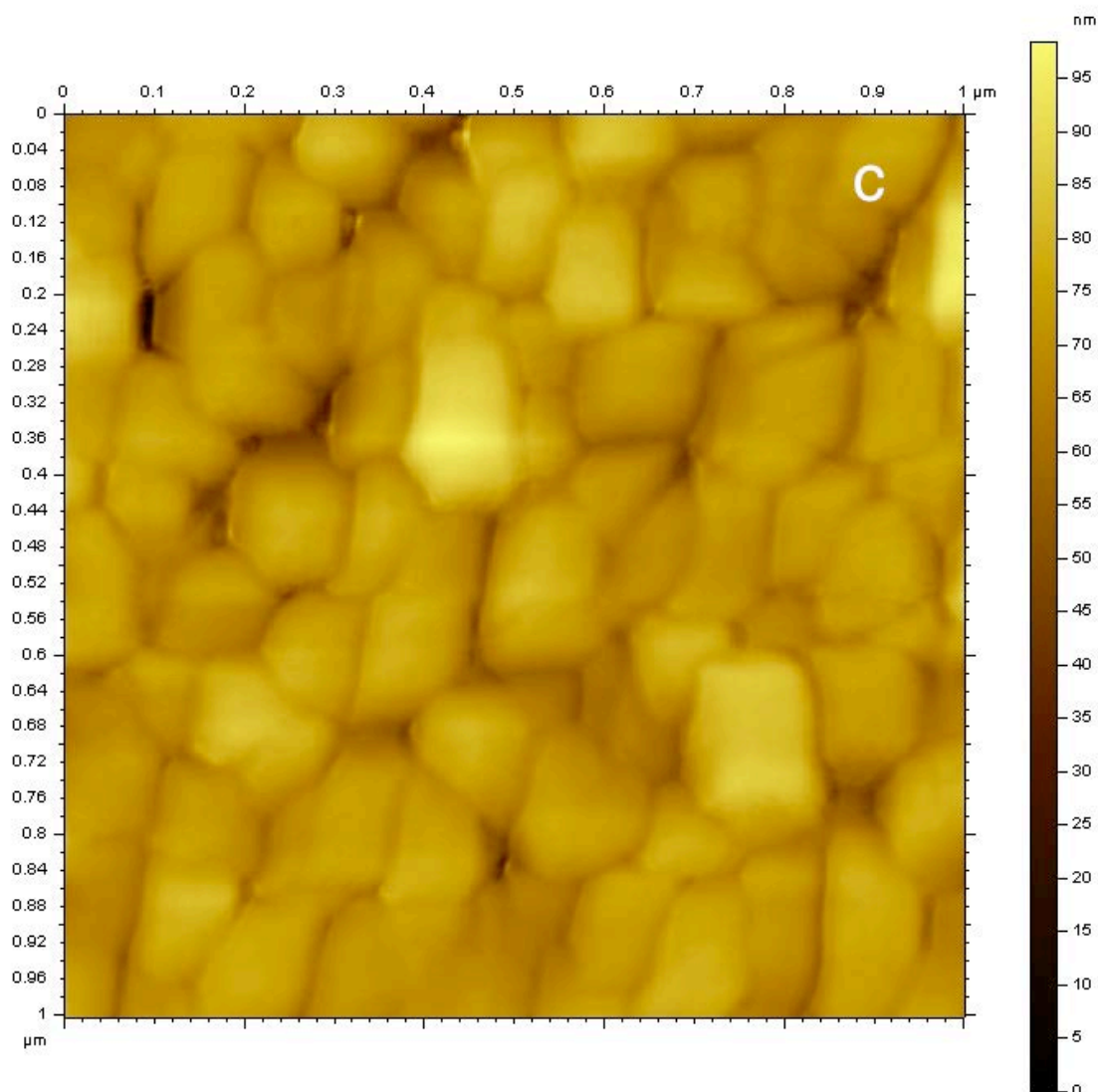
Figure 4.11 Height image of AFM scans (1 μm x 1 μm) of ALD ZnO films grown on reconstructed MgO(111)-(√3x√3)R30° substrates at 130°C for (a) 200 cycles, (b) 400 cycles, (c) 1000 cycles.

To find the effect of temperature on ZnO ALD growth on MgO(111), the growth temperature was changed from 130°C to 170°C. Figure 4.12 depicts surfaces after 1000 cycles of ZnO ALD growth at 170°C . For this ALD ZnO film growth, 3+5+3+5 sec ALD

cycle times were employed. At this higher temperature, smoother ALD ZnO films are formed.
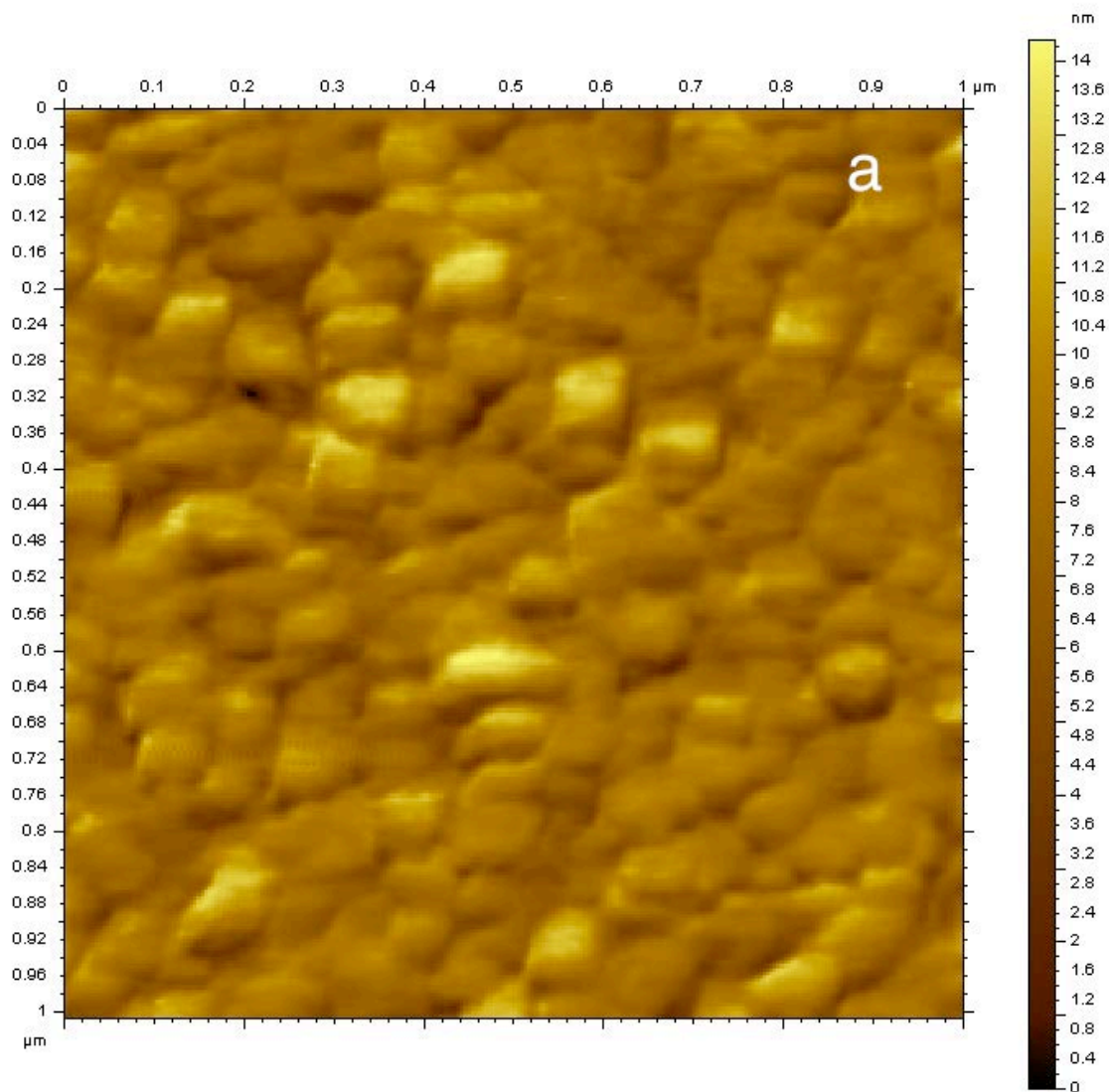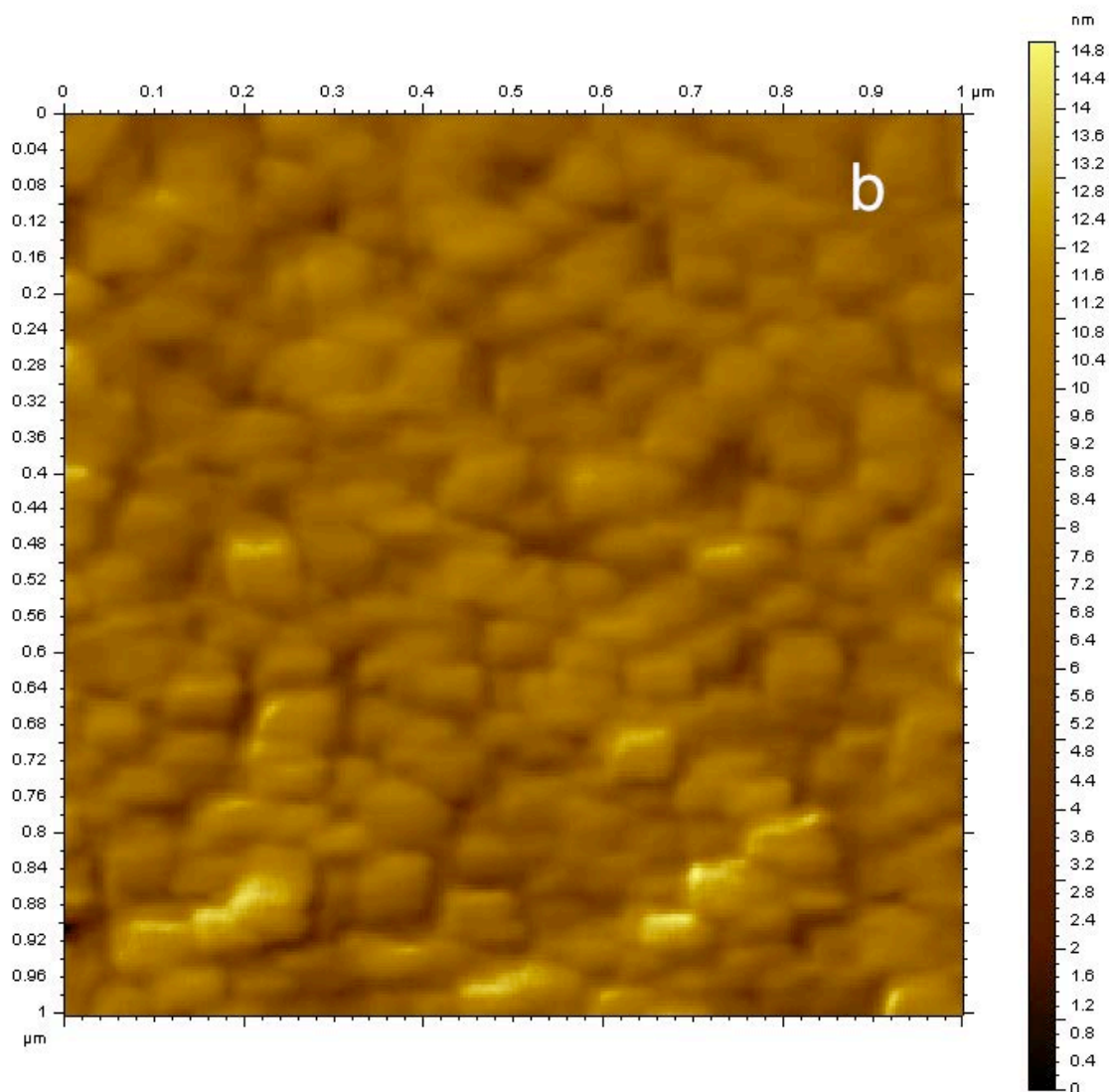
Figure 4.12 Height image of AFM scans (1 μm x 1 μm) of ALD ZnO films grown on reconstructed MgO(111) substrates for 1000 cycles at 170°C (a) on unreconstructed, and (b) reconstructed substrates.

The RMS roughness of the ALD films at 170°C for 1000 cycles was found to be ~ 1 nm. For all the films, RMS roughnesses were calculated and the results were plotted in Figure 4.13. The roughness increases with number of ALD cycles, and reconstructed MgO(111) - ($\sqrt{3}$x$\sqrt{3}$)R30° is a better surface for production of smooth films.
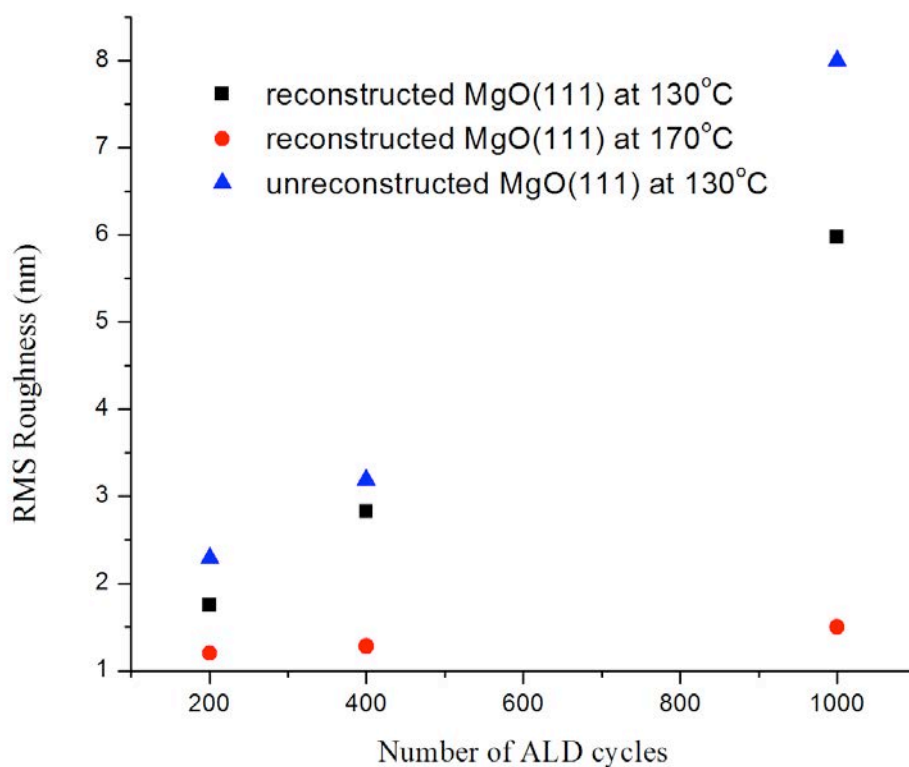
Figure 4.13 RMS roughness as function of number of ALD cycles on unreconstructed and reconstructed MgO(111) substrates.

The effect of annealing on surface morphology of ALD grown ZnO films was also investigated. On annealing the ZnO (1000 cycles) at 800°C for 4 hours in air, ZnO grains became larger in size, which is attributed to the recrystallization of ZnO. Figure

4.14 shows the AFM scan of a ZnO thin film after annealing. The RMS roughness is ~ 9 nm and the average grain size is 310 nm.
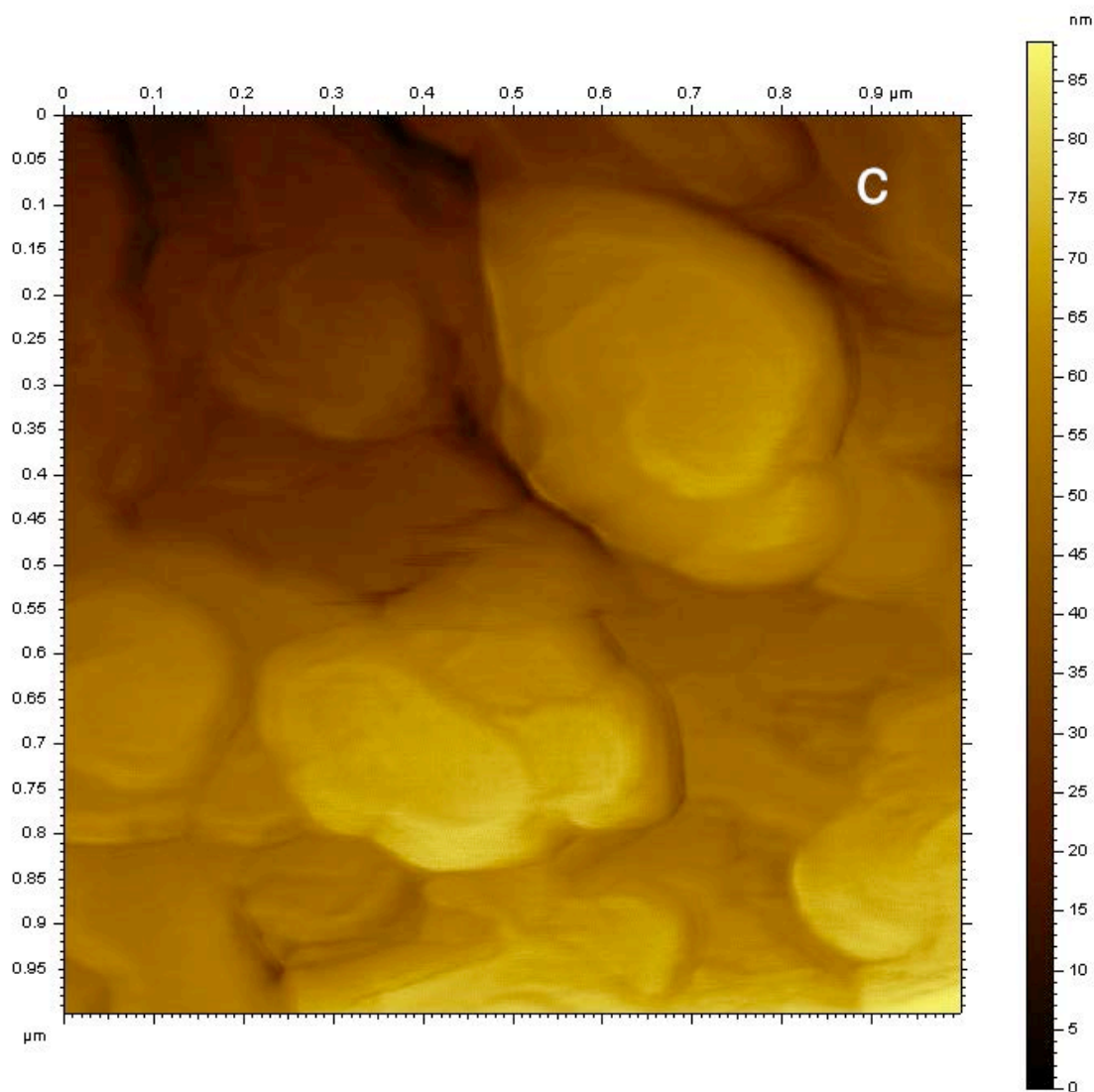
Figure 4.14 Height image of AFM scans (1 μm x 1 μm) of ALD ZnO films grown on reconstructed MgO(111) substrates for 1000 cycles at 170°C and annealed in air for 4 hours at 800°C.

4.6 XRD analysis of ZnO films

XRD analysis was done to find the structure of the ALD-grown ZnO films. Figure 4.15 illustrates the radial scan (θ-2θ) along the normal to the surface of the ZnO films after 1000 ALD cycles at 130°C on MgO(111)-(1x1) and reconstructed MgO(111)-(√3x√3)R30°. The XRD patterns show that the ZnO thin films are polycrystalline, having the wurtzite structure, with preferential growth along the *c*-axis. ZnO grown on MgO(111)-(√3x√3)R30° substrates show strong preferential growth along the (002) direction. In contrast, a small amount of growth along the (100) and (101) directions is also observed when grown on MgO(111)-(1x1) substrates for the same growth conditions. With increasing temperature, growth along the (002) direction becomes more prominent. The crystallite size was calculated using Scherrer's equation. The calculated crystallite size is in the direction perpendicular to the lattice planes.

The crystallite size measurements for 1000 ALD cycles ZnO films grown on both MgO(111)-(1x1) and MgO(111)-(√3x√3)R30° at 170°C are summarized in Table 4.1. For the same ALD growth temperature and thickness, the crystallite size for ZnO films grown on reconstructed MgO(111)-(√3x√3)R30° is larger than for unreconstructed MgO(111)-(1x1). Note that the average grain size estimated from AFM is in plane of the surface. When annealed in air at 800°C for 4 hours the crystallinity of the ZnO thin films was improved. The peak intensity of the ZnO (002) increased upon annealing.
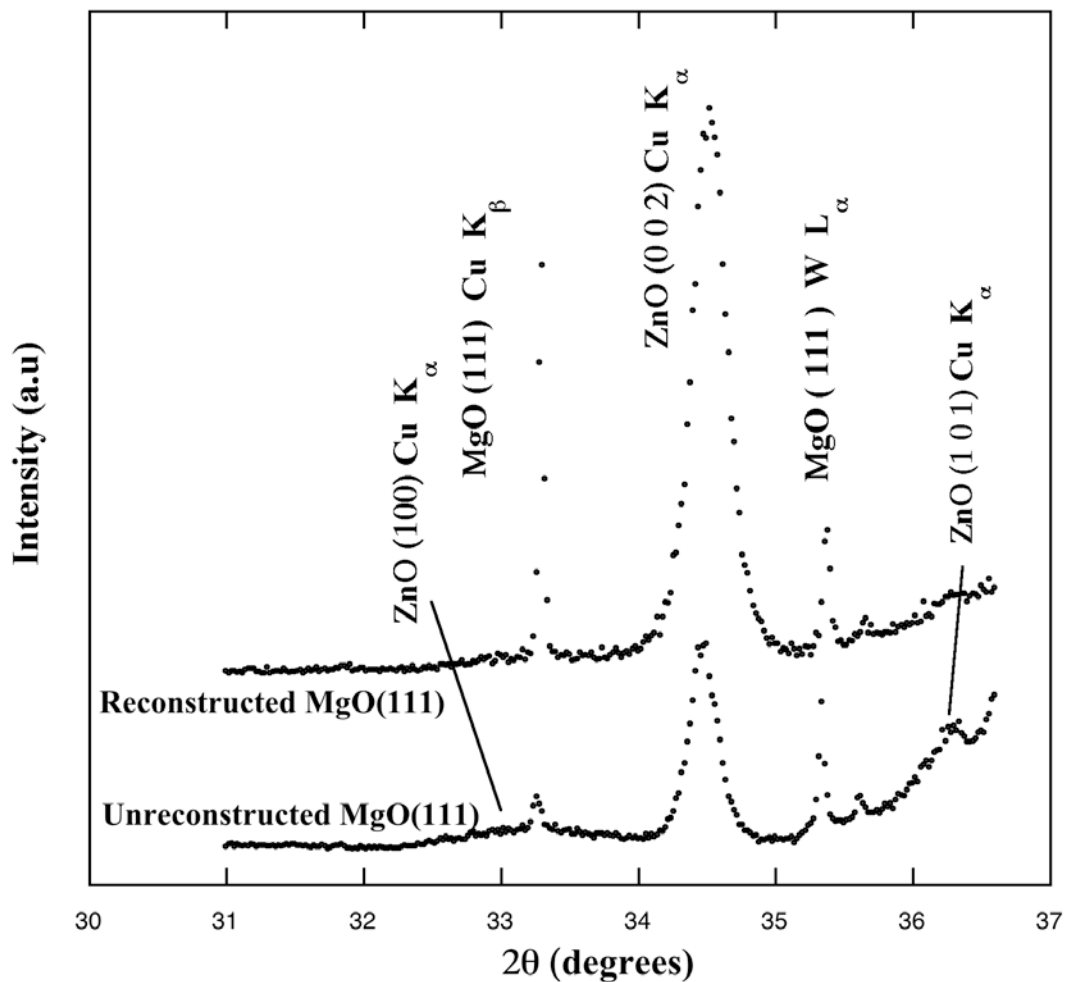
Figure 4.15 XRD patterns of 1000 cycles ALD ZnO grown at 130°C on reconstructed MgO(111)-($\sqrt{3}$x$\sqrt{3}$)R30° and unreconstructed MgO(111)-(1x1).(Scans offset for clarity.)

TABLE 4.1 Crystallite size estimation of 1000 ALD cycles ZnO from Scherrer's equation for (002) direction

Temperature	MgO(111)-($\sqrt{3}$x$\sqrt{3}$)R30° substrate (nm)	MgO(111)-(1x1) substrate (nm)
170°C	28.1	25.7
Anneal at 800°C	39.6	37.8

4.7 XPS analysis of ZnO films

Chemical state and purity of ALD-grown ZnO films were investigated using x-ray photoelectron spectroscopy (XPS). The ZnO films were sputtered *in-situ* with Ar^{2+} ion for 5 minutes to remove the surface contamination before performing XPS. The analysis of data was carried out using the XPS Peak software. Survey scans of 1000 cycles ZnO film grown on MgO(111)-(1x1) at 170°C is shown in Figure 4.16. Only Zn, O, Zn KLL, and LMM Auger peaks were observed, along with a very small C 1*s* peak. High-resolution XPS was performed on Zn 2$p_{3/2}$, O 1*s* and C 1*s* to find their chemical bonding states. All binding energies were referenced to the C1*s* peak, which was assumed to be at 284.8 eV. Figure 4.17 shows the Zn 2*p* peaks for 1000 cycles ALD-grown ZnO films at 170°C. The Zn 2$p_{3/2}$ was observed at 1022.3 eV and Zn 2$p_{1/2}$ was observed at 1045.3 eV. Figure 4.18 shows the O1*s* peak. The O1*s* spectrum consists of two peaks at

530.7 eV and at 531.9 eV. The shallower binding energy peak is from the Zn-O bond of the ZnO crystal. The deeper binding energy feature at 531.9 eV has been attributed to the chemisorbed oxygen species [34].
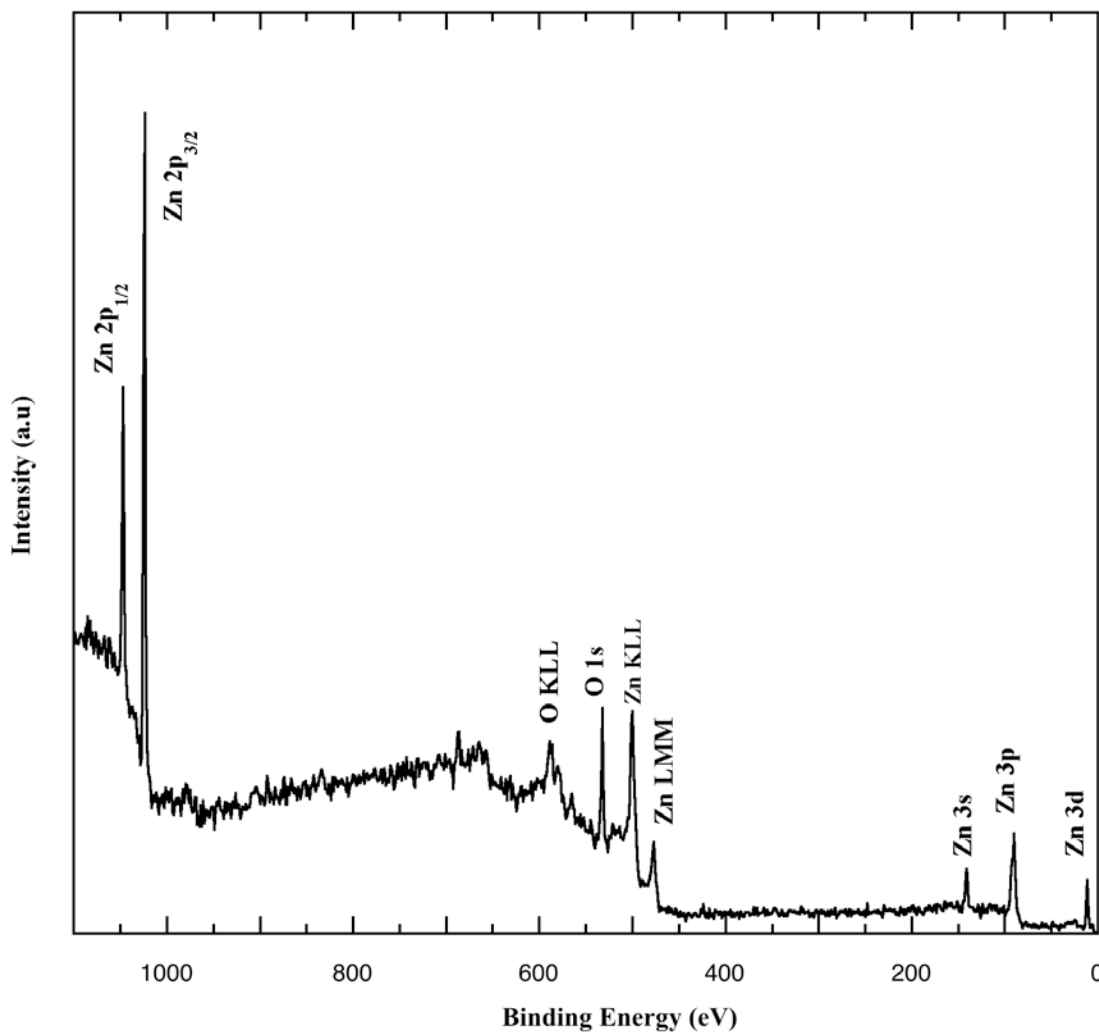
Figure 4.16 XPS spectrum of 1000 cycles ALD ZnO film after 5 minutes Ar^+ ion sputtering.
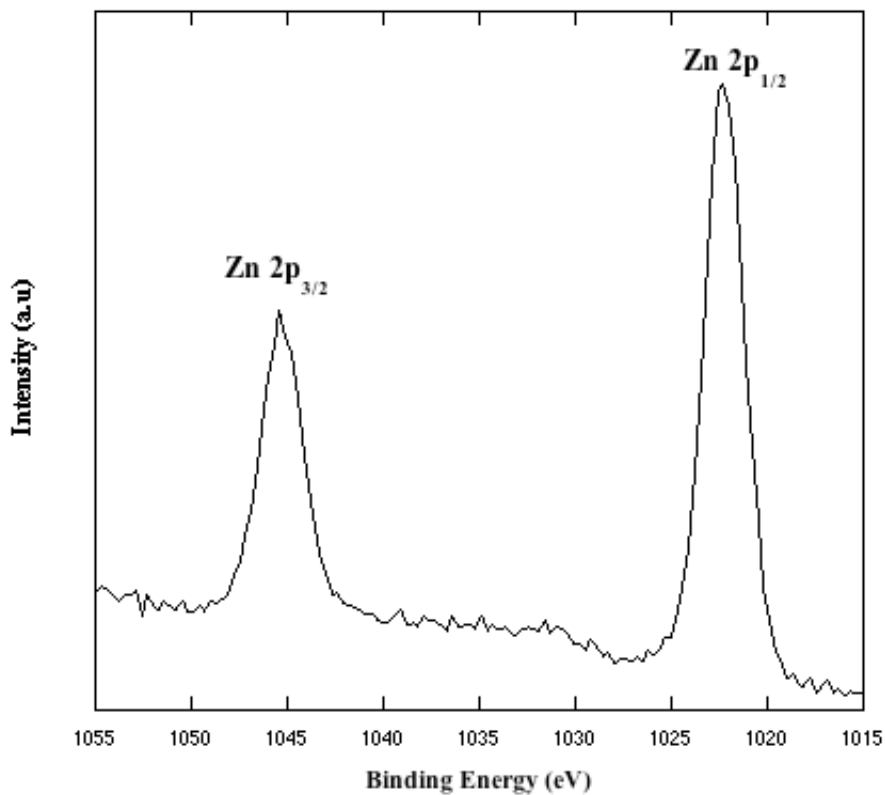
Figure 4.17 XPS Zn *2p* spectrum of 1000 cycles ALD ZnO film after 5 minutes Ar^{+} ion sputtering.
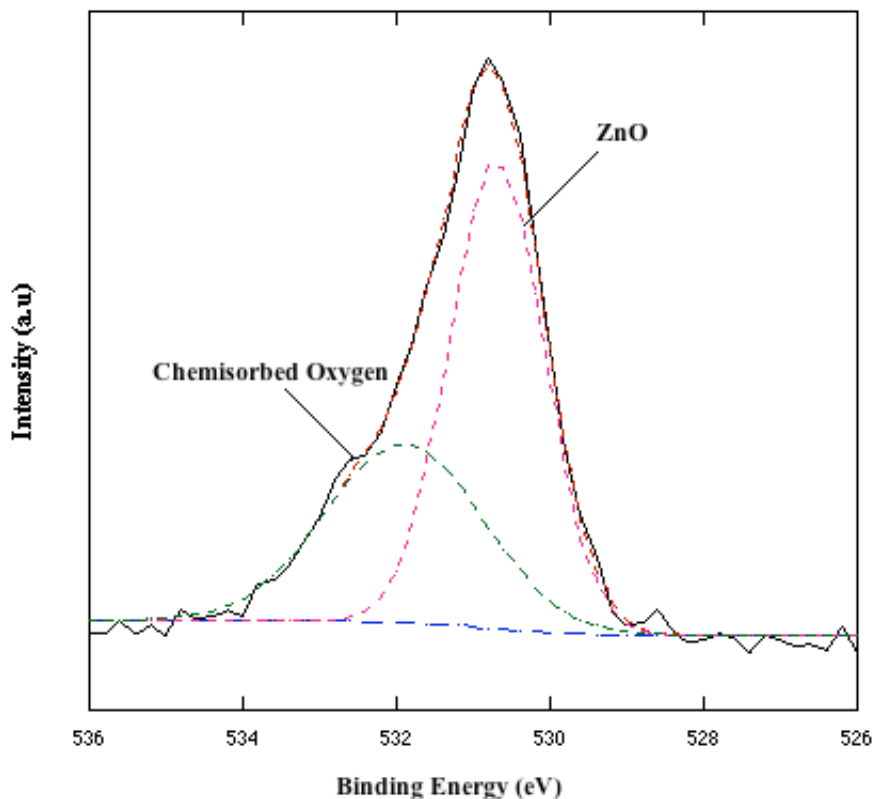
Figure 4.18 XPS O1*s* spectrum of 1000 cycles ALD ZnO films after 5 minutes Ar$^+$ ion sputtering.

The atomic percentages of Zn, O, and C estimated for ALD films grown at different temperatures are shown in Table 4.2. In order to examine the carbon contained in the film, we had to sputter the film, but sputtering the film may alter the stoichiometry in the selvage region. Sputtering was performed with Ar^{2+} ions for 5 minutes before taking the measurements. In our case we found that, for higher growth temperatures, less

carbon is present in the films. As shown in Table 4.2, we found that at 170°C the ALD-grown ZnO film is stoichiometric with very small carbon impurity. However, at 130°C the ZnO is found to be Zn rich and have a higher percentage of carbon impurities.

Table 4.3, shows the atomic percentage of Zn, O and C as a function of the number of ALD cycles. *In-situ* sputtering was not performed before taking these XPS measurements. A large contribution of carbon contamination, presumably from exposing the films to the atmosphere, was found in these films. For 200 ALD cycles ZnO films, the O/Zn ratio was found to be less than unity, whereas for 600 ALD cycles ZnO film it approaches unity. This indicates that the thicker films are stoichiometric. No Mg signal was observed in the XPS survey scans performed on the ZnO films grown for 200 ALD cycles at 130°C.

TABLE 4.2 Elemental composition in atomic percentage of the constituent elements of ZnO films grown at two different temperatures for 1000 ALD cycles after sputtering for 5 minutes.

Temperature	C1s	O1s	Zn2p3	O/Zn	O/Zn[a]
170°C	1.06	48.76	50.18	0.97	0.95
130°C	11.61	34.89	53.5	0.65	0.61

a O/Zn ratio using oxygen component from zinc oxide bonding

TABLE 4.3. Elemental composition in atomic percentage of the constituent elements of ZnO films grown at 130°C for two different cycle lengths without sputtering.

ALD cycles	C1s	O1s	Zn2p3	O/Zn	O/Zn[a]
200 cycles	15.99	37.00	47.01	0.79	0.71
600 cycles	20.56	38.07	41.37	0.92	0.89

a O/Zn ratio using oxygen component from zinc oxide bonding

4.8 Optical Characterization of ZnO films

To determine the optical transparency of the ALD-grown ZnO films, UV-Visible spectroscopy was performed. ZnO thin films grown at different temperatures and thicknesses show similar transmission spectra. Figure 4.19 shows the transmission curve for 1000 cycles ALD ZnO grown on MgO(111)-(1x1) at 130°C. An absorption edge around 380nm was observed. In the visible and ultraviolet region above 380 nm, the ALD-grown ZnO films were ~80% transparent, making such films promising for transparent conducting applications. Assuming the absorption co-efficient $\alpha \propto -\ln T$, we can plot $(\alpha h\nu)^2$ against hν (Tauc plot) to find the band gap of the thin films. From the Tauc plot (Figure 4.20), the bandgap E_g was estimated to be 3.27 eV, which agrees with various reported values for polycrystalline ZnO thin films [35-37].
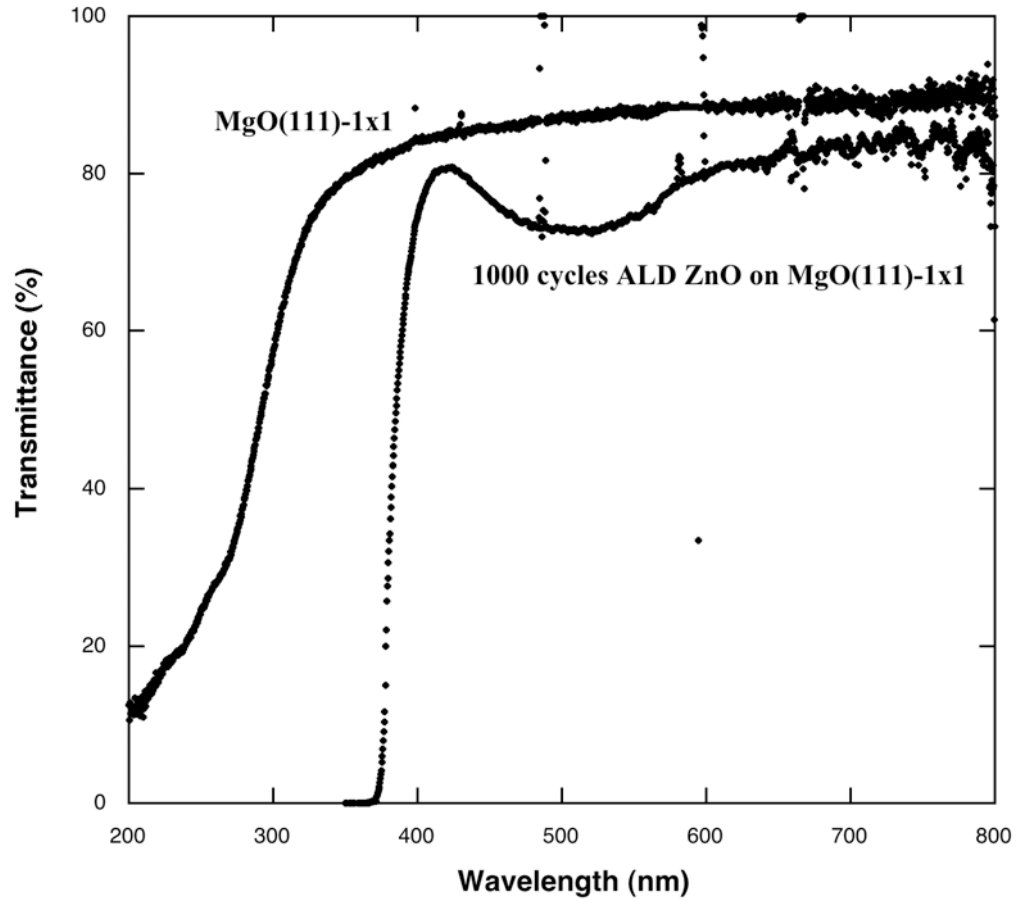
Figure 4.19 Transmission spectra of bare MgO(111) substrate and of 1000 cycles ALD ZnO film grown on MgO(111)-(1x1) at 130°C .
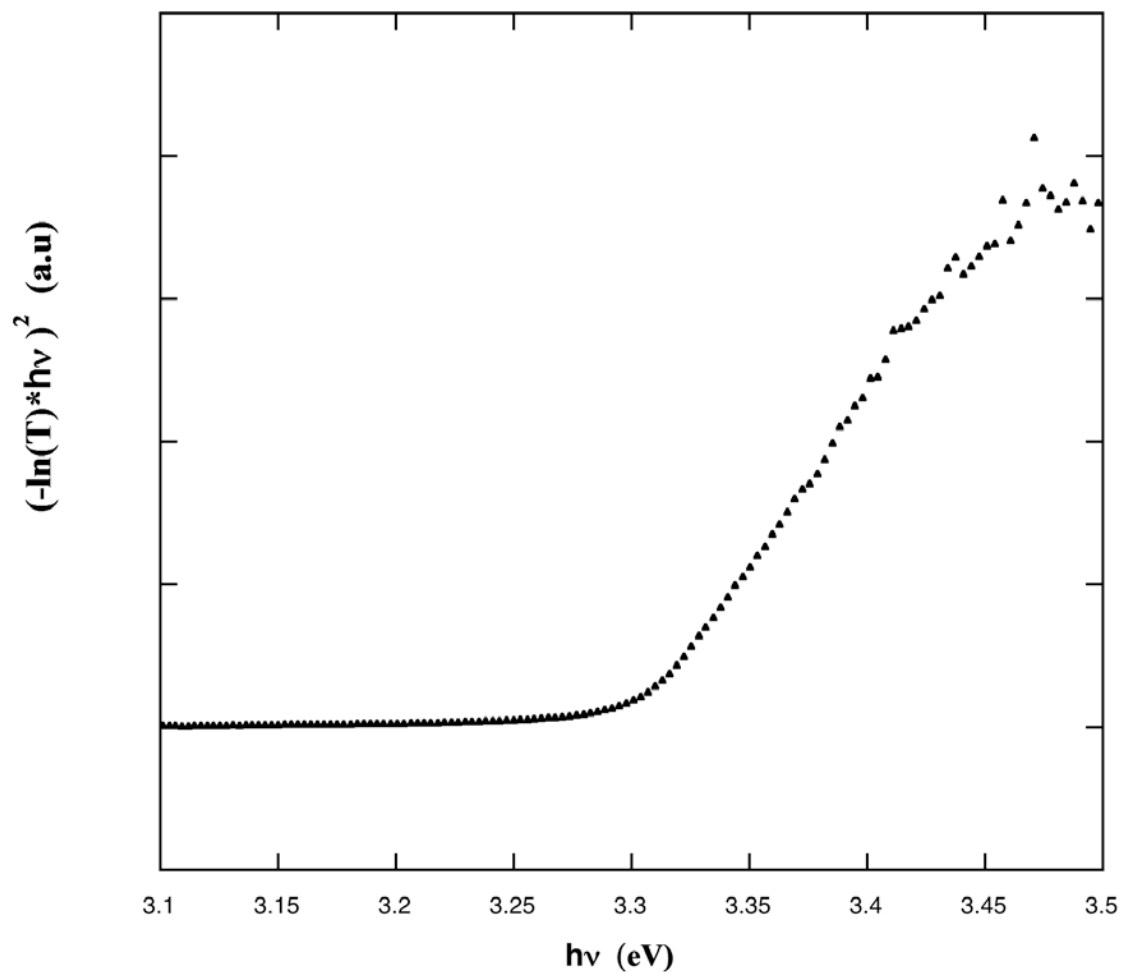
Figure 4.20 Bandgap E_g estimation from transmission spectrum of 1000 cycles ALD ZnO film grown on MgO(111)-(1x1) at 130°C using a Tauc plot.

4.9 Conclusions

ZnO films were grown on polar MgO(111)-($\sqrt{3}$x$\sqrt{3}$)R30° reconstructed and unreconstructed MgO(111)-(1x1) surfaces using a viscous-flow atomic layer deposition reactor. The ALD ZnO films grow as polycrystalline films having the hexagonal wurtzite structure, with highly *c*-axis oriented growth for MgO(111)-($\sqrt{3}$x$\sqrt{3}$)R30° substrates. In contrast, for MgO(111)-(1x1) substrates, (101) and (100)

orientations were also observed normal to the surface along with the dominant (002) direction for same growth condition. This result shows that the initial surface termination and surface symmetry play an important role in growth of ALD ZnO thin films. A lower growth rate of 1.7 Å /cycle for first ~100 cycles during ZnO ALD from QCM results suggested that the initial ZnO growth is initiated by nucleation and followed by layer-by-layer growth that averages 2.3 Å /cycle. AFM results demonstrate that with increasing number of ALD cycles the film roughness increases. Reconstructed MgO(111)-($\sqrt{3}$x$\sqrt{3}$)R30° serves as a better template for production of smoother films. At higher ALD growth temperature, the ZnO thin film roughness is considerably less compared growth at lower growth temperatures. XPS of grown ZnO films shows that thicker films (> 1200 Å) are stoichiometric. A bandgap of ~ 3.27 eV from UV-Visible spectroscopy was found for ALD grown ZnO.

4.10 Discussion

In this study, we tried to understand how the surface polarity and reconstruction affects the ZnO thin film growth over polar MgO(111) surfaces by atomic layer deposition. Surface polarity can have noteworthy effect on growth of thin films on polar oxide substrates. From a theoretical perspective, Density Functional Theory (DFT) calculations have shown that metals such as Cu and Pd absorb more strongly on polar MgO(111) surfaces than on non polar MgO(100) surfaces [38,39]. Gajdardziska-Josifovska and her coworkers have experimentally observed that MgO(111) surface polarity significantly influences the structure of epitaxially grown Fe_3O_4(111) polar film by formation of phase-segregated Fe and Fe_2O_4(100) nano-inclusions both in the film and

at the interface [40]. The reconstructed polar MgO(111) surfaces also have shown a strong effect on growth of thin films. Gajdardziska-Josifovska and her coworkers have experimentally demonstrated α-Fe$_2$O$_3$(0001) grows as a virtually pure phase on the unreconstructed MgO(111)-(1x1) surface and with a Fe$_3$O$_4$(111) interfacial band on the reconstructed MgO(111)-($\sqrt{3}$x$\sqrt{3}$)R30° surface [24]. Lazarov and his co-workers have grown Fe thin films on reconstructed MgO(111)-($\sqrt{3}$x$\sqrt{3}$)R30° and unreconstructed MgO(111)-(1x1) surfaces and found that the Fe films grown on the reconstructed MgO(111) surface show larger magnetic anisotropy compared to the films grown on the unreconstructed MgO(111) surface[41].

In our work we have seen that ALD ZnO grows more smoothly, and with high *c*-axis orientation on reconstructed MgO. In contrast, on unreconstructed MgO(111)-(1x1), ZnO was observed to grow along the (002), (100), and (101) directions under identical ALD growth conditions. This result demonstrates that by controlling the surface termination we can tune the growth directions. It is well established that when ALD ZnO are grown on Si substrates, (002) and (100) are the dominant growth directions. At low temperatures random or (001) directions are the favored, whereas with increase in temperature ALD ZnO films orient along the (002) direction. For ALD ZnO growth using DEZ and water, the orientation changes from (001) to (002) at around 200 °C [42]. Pung and his coworkers have studied the preferential growth of ALD ZnO films in detail [42]. According to them, the polar (002) direction stabilizes its surface by adsorbing the ethyl group or methyl group from premature dissociation of DEZ. This causes the suppression of growth along (002) directions at low temperatures. With the increase in the temperature these hydrocarbon groups desorb from the substrate surface. Therefore,

suppression of growth along (002) direction is no longer possible at these high temperatures. In addition, at higher temperature, Zn and O atoms might have enough energy to migrate to energetically favorable positions, i.e., in the (002) direction. However, our results of ALD ZnO growth on reconstructed MgO(111)-($\sqrt{3}$x$\sqrt{3}$)R30° at low temperatures have indicated that surface reconstruction has a substantial effect on preferential growth of ZnO. Further studies on the interfaces are necessary to understand the reason behind this observation.

The higher surface roughness of ZnO films on unreconstructed MgO(111) surfaces can be explained considering the fact that the nucleation process initiates the ALD ZnO growth. At low temperatures on unreconstructed MgO(111)-(1x1) surfaces (100), (101), and (002) directions of ZnO started to grow on the nucleation sites in the initial couple of cycles. On subsequent ALD cycles they can form crystal grains having different crystal orientations. With the increase in the film thickness these grains grow at different rates in different crystallographic directions. The (002) direction has the highest growth rate as (002) direction is thermodynamically favorable [42]. We speculate the different growth rate of the crystal grains of ZnO on unreconstructed MgO(111)-(1x1) is responsible for higher surface roughness in contrast to reconstructed MgO(111)-($\sqrt{3}$x$\sqrt{3}$)R30°. The ALD ZnO grows only in the (002) direction on MgO(111)-($\sqrt{3}$x$\sqrt{3}$)R30° reconstructed surface. In contrast, ALD ZnO grow in (100), (101), and (002) directions on unreconstructed MgO(111)-(1x1) surface. As the ZnO film growth rate in different crystallographic directions are different, that causes a higher surface roughness with increase in ALD film thickness for unreconstructed MgO(111)-(1x1) surface compared to reconstructed MgO(111)-($\sqrt{3}$x$\sqrt{3}$)R30°surface.

We used QCM to study the growth of ZnO by alternating water and DEZ exposures. The chemical reaction taking place on the surface is believed to be the following [16, 30]:

A) DEZ pulse:

$$S-OH(s)+Zn(CH_2CH_3)_2 \rightarrow S-O-Zn(CH_2CH_3)(s)+CH_3CH_3 \ , \qquad 4.1$$

B) Water pulse:

$$S-O-Zn(CH_2CH_3)(s)+H_2O \rightarrow S-O-ZnOH(s)+CH_3CH_3 \ , \qquad 4.2$$
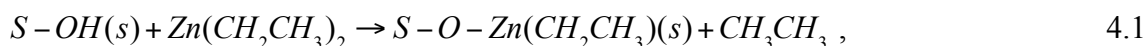
where S is the surface site. There would be a gain in mass of 93.4 g mol^{-1} during the DEZ pulse and loss in mass of 12 g mol^{-1} per cycle according to equation 4.1 and 4.2 in an ALD cycle. However our QCM results do not show any mass loss during the water pulse. This observation is consistent with results obtained by Yousfi and his coworkers [32]. According to them, a more complex reaction among adsorbed intermediate compounds is responsible for such results. Moreover the reactions outlined in Equation 4.1 and 4.2 presume ZnO grows only along (002) directions. One of the possible alternative reaction mechanisms may be:

A) DEZ pulse:

$$2[S-OH(s)]+Zn(CH_2CH_3)_2 \rightarrow (S-O-)_2Zn(s)+2CH_3CH_3 \ , \qquad 4.3$$

B) Water pulse:

$$(S-O-)_2Zn(s)+H_2O \rightarrow 2(S-O-Zn-OH)(s) \ , \qquad 4.4$$
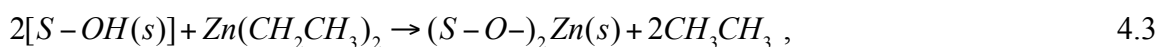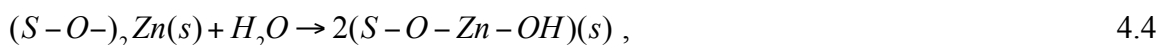
A similar reaction mechanism has been proposed to occur during ALD A_2O_3 by trimethylaluminium and water [43].

4.11 References

1. U. Ozgur, Y. I. Alivov, C. Liu, A. Teke, M. A. Reshchikov, S. Dogan, V. Avrutin, S. J. Cho, and H. Morkoc, J. Appl. Phys. **98**, 041301 (2005).

2. D. K. Hwang, M. S. Oh, J. H. Lim, Y. S. Choi, and S. J. Park, Appl. Phys. Lett. **91**, 121113 (2007).

3. X. Y. Ma, P. L. Chen, D. S. Li, Y. Y. Zhang, and D. Yang, Appl. Phys. Lett. **91**, 251109 (2007).

4. J. D. Ye, S. L. Gu, S. M. Zhu, W. Liu, S. M. Liu, R. Zhang, Y. Shi, and Y.

D. Zheng, Appl. Phys. Lett. **88**, 182112 (2006).

5. P. Chen, X. Ma, and D. Yang, J. Appl. Phys. **101**, 053103 (2007).

6. C.Yuen, S. F. Yu, S. P. Lau, Rusli, and T. P. Chen, Appl. Phys. Lett. **86**, 241111 (2005).

7. Y. I. Alivov, E. V. Kalinina, A. E. Cherenkov, D. C. Look, B. M. Ataev, A.

K. Omaev, M. V. Chukichev, and D. M. Bagnall, Appl. Phys. Lett. **83**, 4719 (2003).

8. T. Gruber, C. Kirchner, R. Kling, F. Reuss, and A. Waag, Appl. Phys. Lett. **84,** 5359 (2004).

9. K. Ogata, T. Kawanishi, K. Maejima, K. Sakurai, Sz. Fuijita, and Sg. Fugita, J. Crystal. Growth. **553,** 237 (2002).

10. S. H. Park, and Y. E. Lee, J. Mater. Sci. **39,** 2195 (2004).

11. D. J. Rogers, F. Hosseini Teherani, A. Yasan, K. Minder, P. Kung, and M. Razeghi, Appl. Phys. Lett. **88,** 141918 (2006).

12. S. J. Jiao, Z. Z. Zhang, Y. M. Lu, D. Z. Shen, B. Yao, M. Razeghi, J. Y. Zhang, B. H. Li, D. X. Zhao, X. W. Fan, and Z. K. Tang, Appl. Phys. Lett. **88,** 031911 (2006).

13. B. Wacogne, M. P. Roe, T. J. Pattinson, and C. N. Pannell, Appl. Phys. Lett. **67,** 1674 (1995).

14. F. Fenske, B. Selle, and M. Birkholz, Jpn, J. Appl. Phys. **44,** L662 (2005).

15. B. N. Illy, A. C. Cruickshank, S. Schumann, R. D. Campo, T. S. Jones, S. Heutz, M. A. McLachen, D. W. McComb, D. J. Riley, and M. P. Ryan, J. Mater. Chem. **21,** 12949 (2011).

16. A. Yamanda, B. S. Sang, and M. Kongai, Appl. Surf. Sci. **112,** 216 (1997).

17. S. J. Lim, S. Kwon, and H. Kim, Thin Solid Films. **516,** 1523 (2008).

18. Y. I. Alivov, E. V. Kalinina, A. E. Cherenkov, D. C. Look, B. M. Ataev, A. K. Omaev, M. V. Chukichev, and D. M. Bagnall, Appl. Phys. Lett. **83,** 4719 (2003).

19. J. W. Elam, D. Routkevitch, and S. M. George, J. Electrochem. Soc. **150,** (6) G339 (2003).

20. M. Ritala, and M. Leskela, Nanotechnology, **10,** 19 (1999).

21. M. W. Cho, A. Setiawan, H. J. Ko, S. K. Hong, and T. Yao, Semicond. Sci. Technol. **20,** S13 (2005).

22. H. Makino, S. Kishimoto, T. Yamada, A. Miyake, N. Yamamoto, T. Yamamoto, Phys. Stat. Sol. (a) **205**, No. 8, 1971 (2008).

23. M. Gajdardziska-Josifovska, R. Plass, M. A. Schofield, D. R. Giese, and R. Sharma, J. Electron Microsc. **51,** S13 (2002).

24. S. H. Cheung, A. Celik-Aktas, P. Dey, K. Pande, M. Weinert, B. Kabius, D. J. Keavney, V. K. Lazarov, S. A. Chambers, and M. Gajdardziska-Josifovska, Phys. Rev. B. **85,** 045405 (2012).

25. V. K. Lazarov, M. Weinert, S. A. Chambers, and M. Gajdardziska-Josifovska, Phys. Rev. B. **72,** 195401 (2005).

26. V. K. Lazarov, J. Zimmerman, S. H. Cheung, L. Li, M. Weinert, and M. Gajdardziska-Josifovska, Phys. Rev. Lett. **94,** 216101 (2005).

27. A. Subramanian, L. D. Marks, O. Warschkow, and D. E. Ellis, Phys. Rev. Lett. **92**, 026101 (2004)..

28. H. C. Poon, X. F. Hu, S. E. Chamberlin, D. K. Saldin, and C. J. Hirschmugl. Surf. Sci. **600,** 2505 (2006).

29. R. Plass, J. Feller, and M. Gajdardziska-Josifovska, Surf. Sci. **414,** 26 (1998).

30. J. W. Elam, and S. M. George, Chem. Mat. **15,** 1020 (2003).

31. M. Schuisky, J. W. Elam, and S. M. George, Appl. Phys. Lett. **81,** 180 (2002).

32. E. B. Yousfi, J. Fouache, and D. Lincot, Appl. Surf. Sci. **153,** 223 (2000).

33. V. Lujala, J. Skarp, M. Tammenmaa, and T. Suntola. Appl. Surf. Sci. **82,** 34 (1994).

34. T. Dhakal, D. Vanhart, R. Chirstian, A. Nandur, A. Sharma, and C. R. Westgate. J. Vac. Sci. Technol. A **30,** 021202 (2012).

35. F. K. Shan, and Y. S. Yu, Thin Solid Films **435,** 174 (2003).

36. V. Craciun, J. Elders, J.G. E. Gardeniers, and I. W. Boyd, Appl. Phys. Lett. **65,** 2963 (1994).

37. C. X. Shan, J. Y. Zhang, B. Yao, D. Z. Shan, X. W. Fan, and K. L. Choy. J. Vac. Sci. Technol. B **27(3),** 1765 (2009).

38. J. Goniakowski, and C. Noguera, Phys. Rev. B **60**, 16120 (1999).

39. R. Benedek, M. Minkoff, and L. H. Yang, Phys. Rev. B **54**, 7697 (1996).

40. V. K. Lazarov, S. Chambers, and M. Gajdardziska-Josifovska, Phys. Rev. Lett. **90**, 216108 (2003).

41. V.K. Lazarov, A. Kohn, S.H. Cheung, S.A. Chambers, and M. Gajdardziska-Josifovska, Microscopy and Microanalysis **13**,1044 (2007).

42. S.-Y. Pung, K.-L. Choy, X. Hou, and C. Shan, Nanotechnology **19**, 435609 (2008).

43. A. Rahtu, T. Alaranta, M. Ritala, Langmuir **17**, 6506 (2001).

Chapter 5

Growth of ZnO thin films on non-polar MgO(100), α-Al$_2$O$_3$(0001) and polar 6H-SiC (0001) surfaces by atomic layer deposition

Abstract

This chapter describes the growth of ZnO thin films on non-polar MgO(100) and α-Al$_2$O$_3$(0001) surfaces using the viscous-flow atomic layer deposition reactor, which is described in Chapter 3. This chapter also describes the growth of ZnO on polar substrates other than MgO(111), viz. 6H-SiC(0001) surfaces.

5.1 Introduction

In Chapter 4, I have discussed the growth of ZnO on polar MgO(111) surfaces using ALD. In order to find any difference of ZnO growth on polar surface and non-polar surfaces, we have grown ALD ZnO on non-polar MgO(100) surface. Growth of ZnO on polar surfaces and non-polar surfaces can be different. It has been reported that using laser molecular beam epitaxy, ZnO grows along non-polar direction (110) on $SrTiO_3$(001); in contrast growth along the (002) direction is observed on $SrTiO_3$(111) surfaces [1]. However, the growth direction of ZnO is also dependent on the growth technique and growth temperature.

MgO(100) is a non-polar surface having zero net charge on each unit layer and zero net dipole moment normal to the surface. Figure 5.1 shows the atomic structure of the MgO(100) surface. Efforts had been made to grow epitaxial ZnO thin films on MgO(100) using plasma-assisted molecular beam epitaxy, pulsed laser deposition, and rf-magnetron sputtering [2-4]. To our knowledge, no previous effort has been made to grow ZnO on MgO(100) surfaces using atomic layer deposition.

We have also grown ALD ZnO on other substrates viz. SiO_2, α-Al_2O_3(0001), and 6H-SiC(0001). We are interested to know whether ZnO can be grown epitaxially at low temperature on these substrates. Low-temperature ALD ZnO growth is preferable for flexible optoelectronic applications, where the substrates cannot withstand higher growth temperatures.

Table 5.1 shows the different lattice parameters of ZnO, Al_2O_3, and SiC. The SiC substrate has the lowest lattice mismatch ~5.4 % with ZnO, whereas the Al_2O_3(0001) has a much larger in-plane lattice mismatch, ~ 18%.

Table 5.1 Lattice constants and crystal symmetry of different substrates for ZnO thin films.

Crystal	Space Group	Crystal structure	Lattice constants (Å) a	Lattice constants (Å) c
ZnO	P6$_3$mc	Hexagonal	3.251	5.213
MgO	Fm$\bar{3}$m	Cubic	4.212	-
α-Al$_2$O$_3$	R$\bar{3}$c	Hexagonal	4.757	12.983
6H-SiC	P6$_3$mc	Hexagonal	3.246	25.195

Sapphire or α-Al$_2$O$_3$ is rhombohedral in structure and has the space group R$\bar{3}$c. Figure 5.2 shows the crystal structure of the α-Al$_2$O$_3$ (0001) surface. Figure 5.3 shows the different crystallographic planes of α-Al$_2$O$_3$. The c-plane (0001), r-plane and a-plane Al$_2$O$_3$ are most widely used as a substrate to grow ZnO , because the oxygen sublattice has a hexagonal symmetry [6, 7]. However, because of large lattice mismatch, the ZnO thin films over Al$_2$O$_3$ have poor crystalline quality with high threading dislocation [8]. This makes the optoelectronic application of ZnO thin films grown over Al$_2$O$_3$(0001) very challenging. GaN and MgO are used as buffer layers to improve the crystalline quality or grow epitaxial ZnO using plasma-assisted molecular beam epitaxy [8-11]. In recent years, efforts have been made to grow epitaxial ZnO on α-Al$_2$O$_3$ using ALD. However, in most cases, the growth temperatures were above 180 °C [12-15]. Here we have grown ALD ZnO on α-Al$_2$O$_3$ at growth temperatures as low as 140 °C.
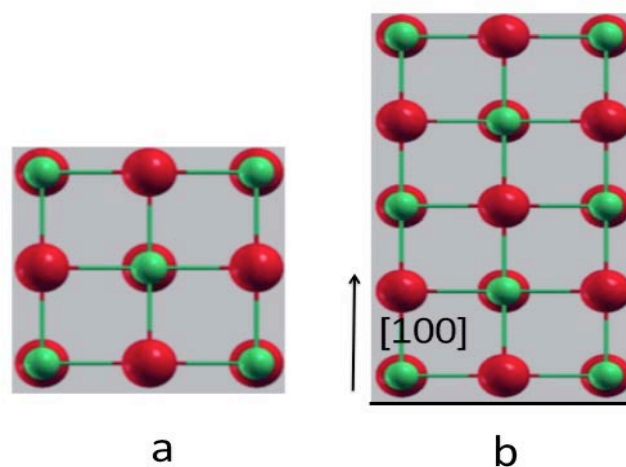
Figure 5.1 (a) Top view and (b) side view of MgO(100) surface , where red balls represent the oxygen atoms and greens balls represent Mg atoms.
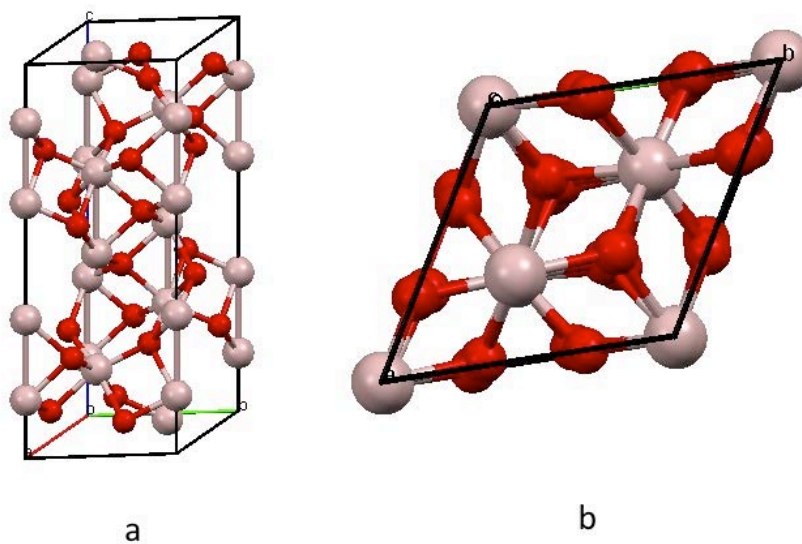
Figure 5.2 (a) Hexagonal (2x2x1) unit cell of α-Al$_2$O$_3$. Here red balls represent the oxygen atoms and light pink represent Al atoms. (b) α-Al$_2$O$_3$(0001) plane viewed from the top.
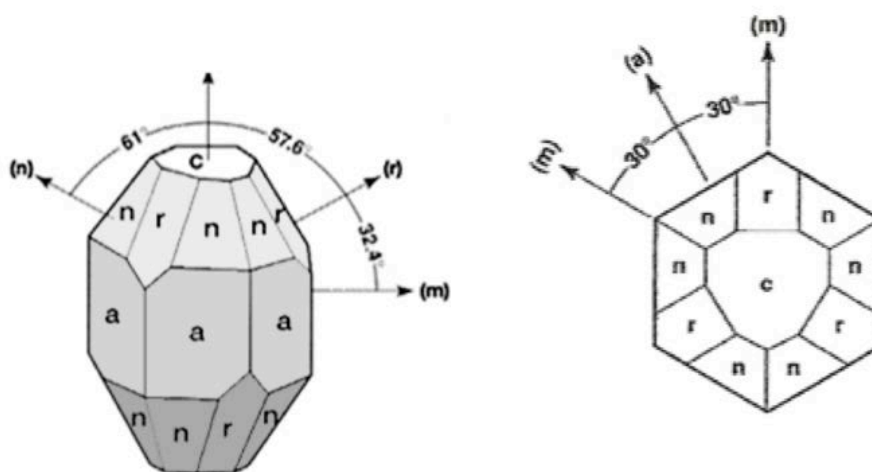
Figure 5.3 Rhombohedral structure and surface planes of sapphire [5].

The α-Al(0001) surface is non-polar and believed to be Al-terminated and unreconstructed in UHV condition [16]. However, upon annealing 1500 °C in UHV, it produces Al-rich polar ($\sqrt{3}$x$\sqrt{3}$) R30° reconstructed surfaces [17]. Upon annealing at various other temperatures, other different Al-rich polar reconstructed surfaces such as ($2\sqrt{3}$x$2\sqrt{3}$) R30° at 1100 °C, ($3\sqrt{3}$x$3\sqrt{3}$) R30° at 1150 °C, ($\sqrt{31}$x$\sqrt{31}$) R9° at 1350 °C, can be formed [17-19].

However, in the presence of water vapor, the α-Al$_2$O$_3$(0001) surface is OH-terminated [20]. This OH-terminated surface is an excellent template to grow ALD ZnO, as OH-terminated surface is required to initiate the ALD ZnO growth.

SiC is a wide-bandgap semiconductor, used extensively in high-power electronic devices. A hexagonal bilayer of Si and C atoms forms the building block of the SiC

structure. Depending on the arrangements of these atoms, it can have the wurtzite or zinc-blende crystal structure. SiC exists in ~170 polytypes, depending on the bilayer stacking. We have used the surface of the 6H-SiC (0001) polytype to grow ALD ZnO. The H in 6H-SiC stands for hexagonal and its unit cell consists of six bilayers. The 6H-SiC has ABCACB(ABCACB)… stacking arrangements. Figure 5.4 shows such a stacking arrangement.

Due to strong asymmetric valence charge distribution in carbon/silicon bonds in SiC, most of the valence charge is located near carbon atom. This makes the 6H-SiC (0001) surface polar. The clean 6H-SiC(0001) surface exhibits a number of surface reconstructions as the stoichiometry of the surface changes. For Si rich conditions, annealing around 850 °C gives a (3x3) reconstruction [20]. Further annealing at 1050 °C gives a ($\sqrt{3}$x$\sqrt{3}$)R30° reconstruction [22].
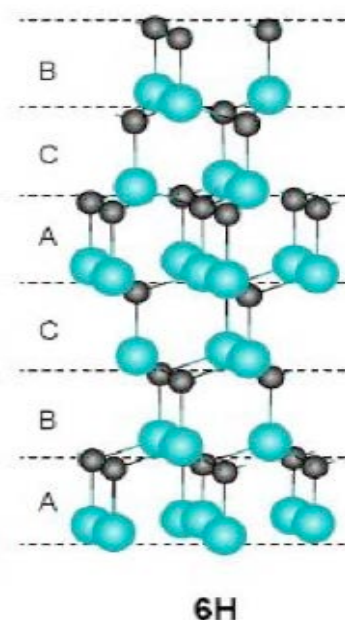
Figure 5.4 Atomic structures of 6H-SiC. Black balls represent carbon atoms and blue balls represent Si atoms [From Ref. [23]].

In recent years, limited efforts have been made to grow ZnO on 6H-SiC using ALD [24, 25]. However, the ALD growth temperatures were kept above 180 °C in an attempt to achieve epitaxial ZnO growth. To our knowledge, no epitaxial growth of ZnO has been reported yet on 6H-SiC surfaces by ALD.

5.2 Growth of ALD ZnO films on the nonpolar MgO(100) surface

Structural studies revealed that the MgO(100) surface is a nearly ideal truncation of the bulk structure. The best experimentally fitted model corresponds to an inward relaxation for surface planes of MgO(100) of 2% [26]. We have grown ALD ZnO on such surfaces using diethyl zinc (DEZ) and water.

5.2.1 Substrate preparation and annealing studies of the MgO(100) surface

To produce a smooth surface, the MgO(100) sample was annealed at 1100 °C for 20 hours. 10 mm x 10mm x 0.5 mm MgO(100) single-side polished samples from MTI Inc., with purity 99.99 %, were cleaned sonically for 10 minutes in a bath of acetone, then rinsed with methanol. Following the methanol rinse, they were cleaned sonically again in a bath of methanol for 10 minutes, and then dried by flowing nitrogen. The polished surfaces of the two samples were placed face to face and inserted in alumina crucible, which then placed in a tube furnace. Then the samples annealed at 1100 °C in air. Figure 5.5 depicts the morphological change of the MgO(100) surface at different times during the annealing.
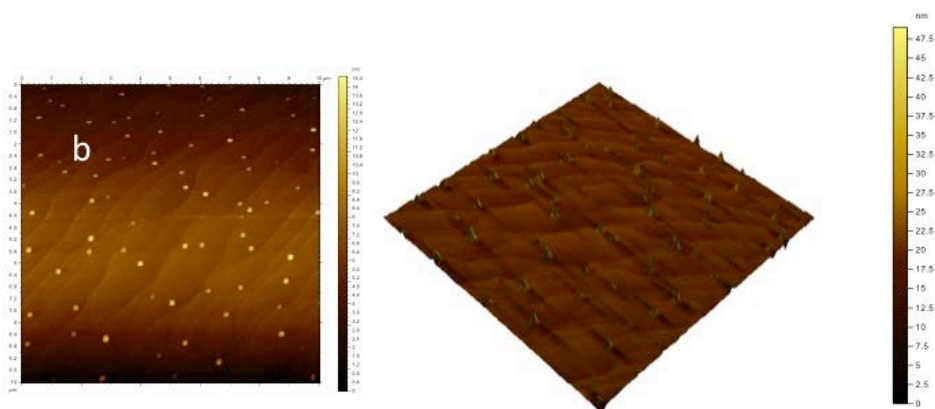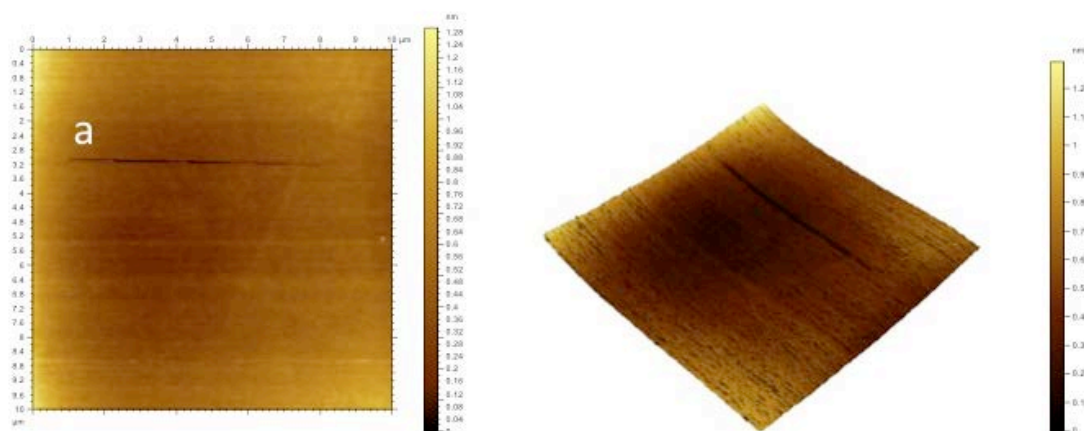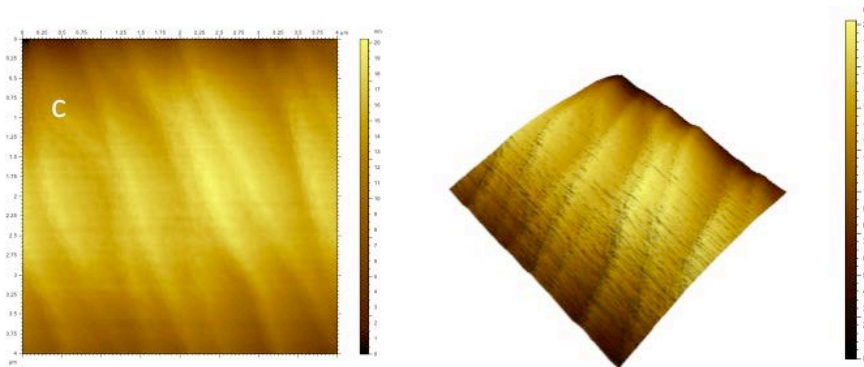
Figure 5.5 Height image of AFM (10x10 μm^2) scan of MgO(100) surface after annealing at 1100 °C (a) As-received (b) after 20 h (c) after 48h.

Figure 5.5 (a) shows the as-received surface with RMS roughness of 2 nm. After annealing at 1100 °C for 20 hours, the MgO (100) surface become smoother, with RMS roughness of 1.6 nm. Upon annealing for 48 hours, the surface tends to become rough with RMS roughness of 5.4 nm.

5.2.2 Growth and morphology of ALD ZnO films on the MgO(100) surface

Once the MgO substrates were prepared, they were loaded to the viscous-flow ALD rector for ZnO growth. ALD ZnO films were deposited over MgO(100) surfaces at

140 °C using 200 ALD ZnO cycles. ALD cycle times of 3-5-3-5 s were employed during the growth.
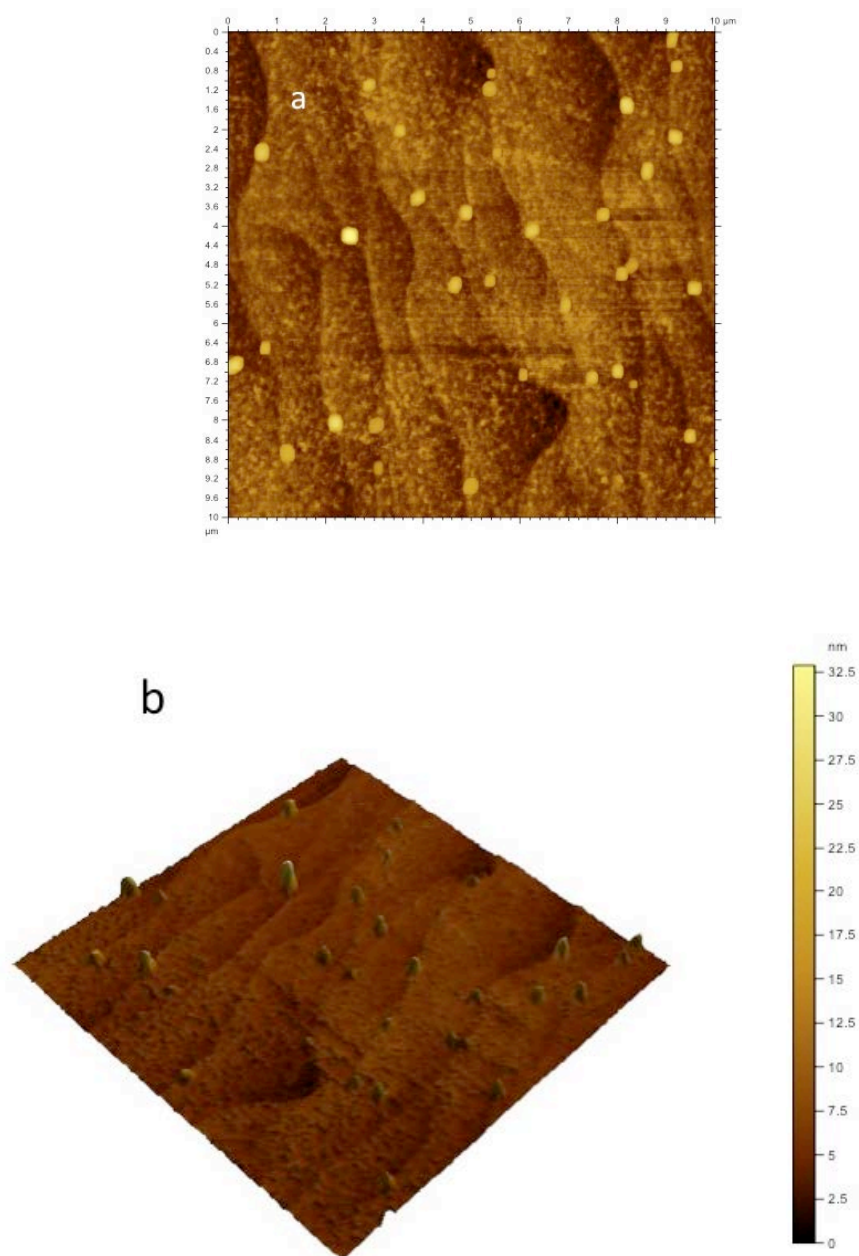
Figure 5.6 AFM scans (10x10 μm^2) of 200 cycles ALD ZnO films grown on MgO(100) at 140 °C.(a) Height (b) Three dimensional image.

AFM in contact mode was used to measure the surface morphology of ALD ZnO films grown on MgO(100) surfaces. Figure 5.6 shows the AFM images of 200-cycle ALD ZnO films. The ALD ZnO thin films grow very smoothly on the MgO(100) surface. The RMS roughness was calculated to be ~ 1.4 nm.

5.2.3 XRD studies of ALD ZnO films on the MgO(100) surface

XRD was performed on a 1000-cycle ALD ZnO film grown on MgO(100) at 140 °C.
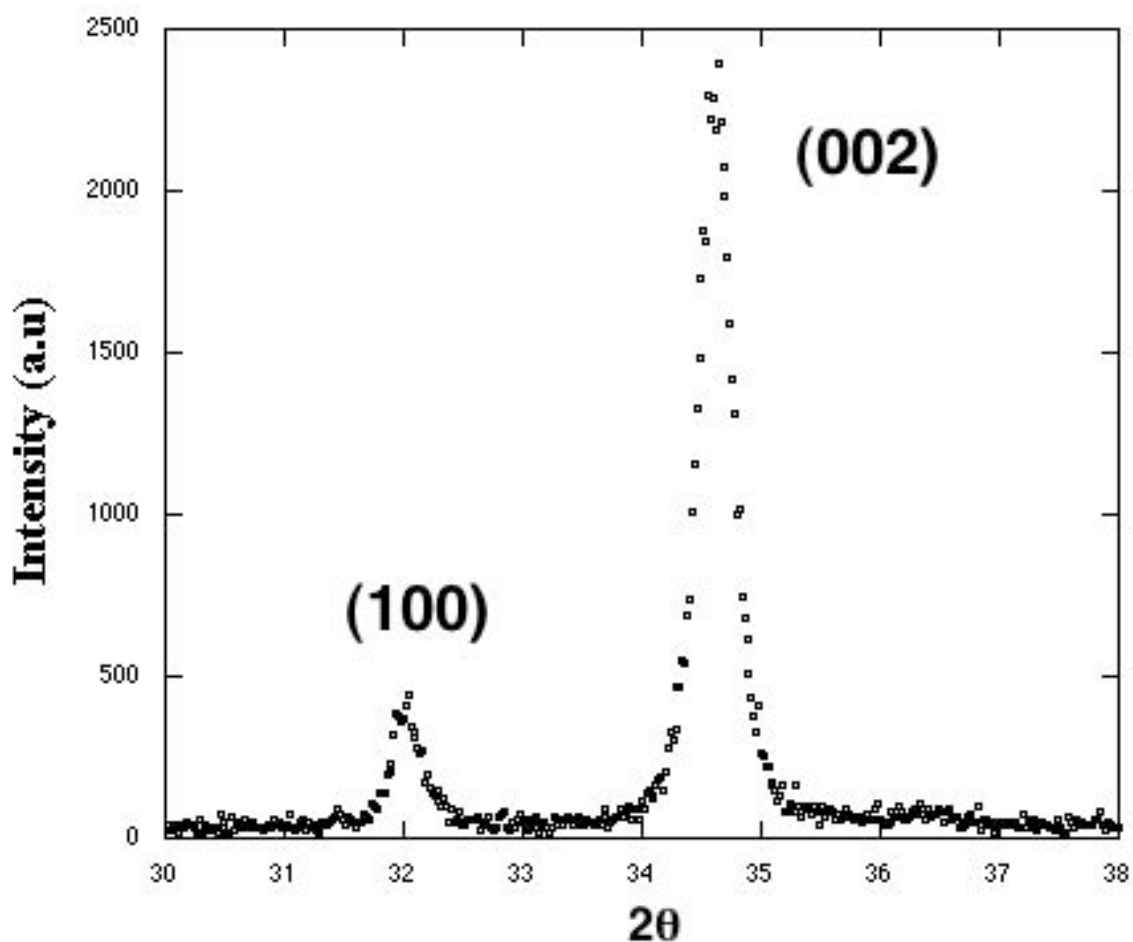
Figure 5.7 XRD (θ-2θ) pattern of 1000-cycle ALD ZnO grown at 140 °C on MgO(100).

Figure 5.7 shows X-ray diffraction pattern of ZnO/MgO(100) heterostructure. The ALD ZnO grown on MgO(100) shows strong preferential growth along the polar (002) direction. However growth along the (100) direction is also observed.

5.3 Growth of ALD ZnO film on nonpolar α-Al$_2$O$_3$ (0001) surfaces

Before growing the ALD ZnO films on α-Al$_2$O$_3$(0001) surfaces, 5 mm x 5 mm x 0.5 mm α-Al$_2$O$_3$(0001) single-side polished samples from MTI Inc., with purity 99.99 %, were cleaned sonically with acetone and methanol, as described for MgO(100). After cleaning, a substrate was loaded into the ALD reactor. 500-cycle ALD ZnO films were grown on the α-Al$_2$O$_3$(0001) surface at 140 °C. The ALD cycle time 3-5-3-5 s was employed during the growth.

5.3.1 Surface morphology of ALD ZnO films on α-Al$_2$O$_3$ (0001) surfaces.

AFM analysis in contact mode was performed over the 500-cycle ZnO thin film grown on α-Al$_2$O$_3$(0001). Figure 5.8(a) shows the AFM image of an as-received α-Al$_2$O$_3$(0001) substrate. The RMS roughness of such surfaces was ~ 2.4 nm. Figure 5.8(b) shows the AFM image of ZnO films grown on α-Al$_2$O$_3$(0001) substrates. Rectangular grains of ZnO were observed in the AFM scans. This might occur due to columnar growth along the (002) direction of ZnO. The RMS roughness of the surface is ~ 4.5 nm.

a

b
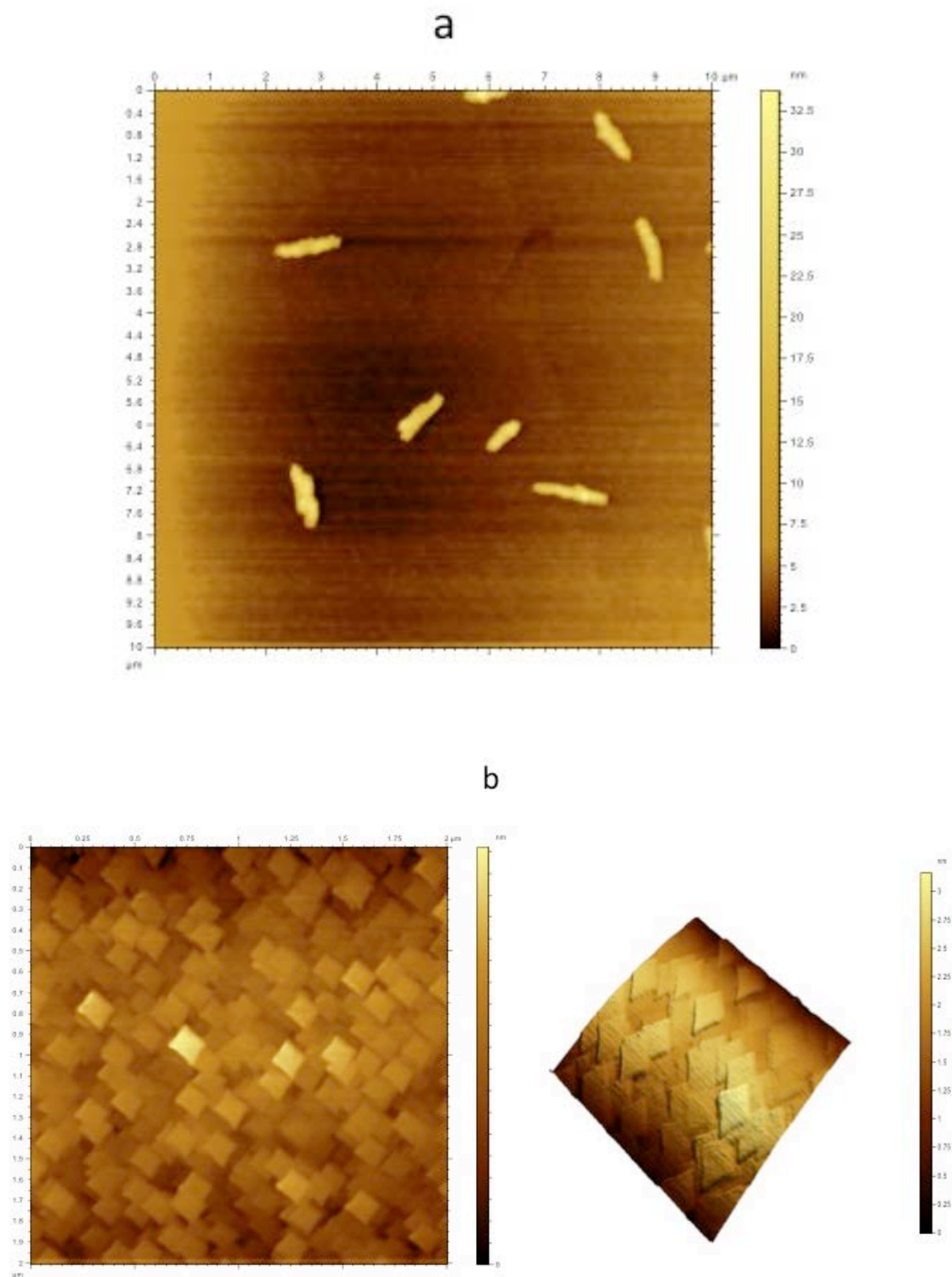
Figure 5.8 Height image of AFM scans (a) (10x10 μm^2) as received (b) (2x2 μm^2) 500-cycle ALD ZnO on α-Al$_2$O$_3$(0001) surfaces at 140 °C.

5.3.2 XRD studies of ALD ZnO films on α-Al₂O₃ (0001) surfaces

XRD was performed on 500-cycle ALD ZnO films grown on α-Al₂O₃(0001) surfaces at 140 °C.
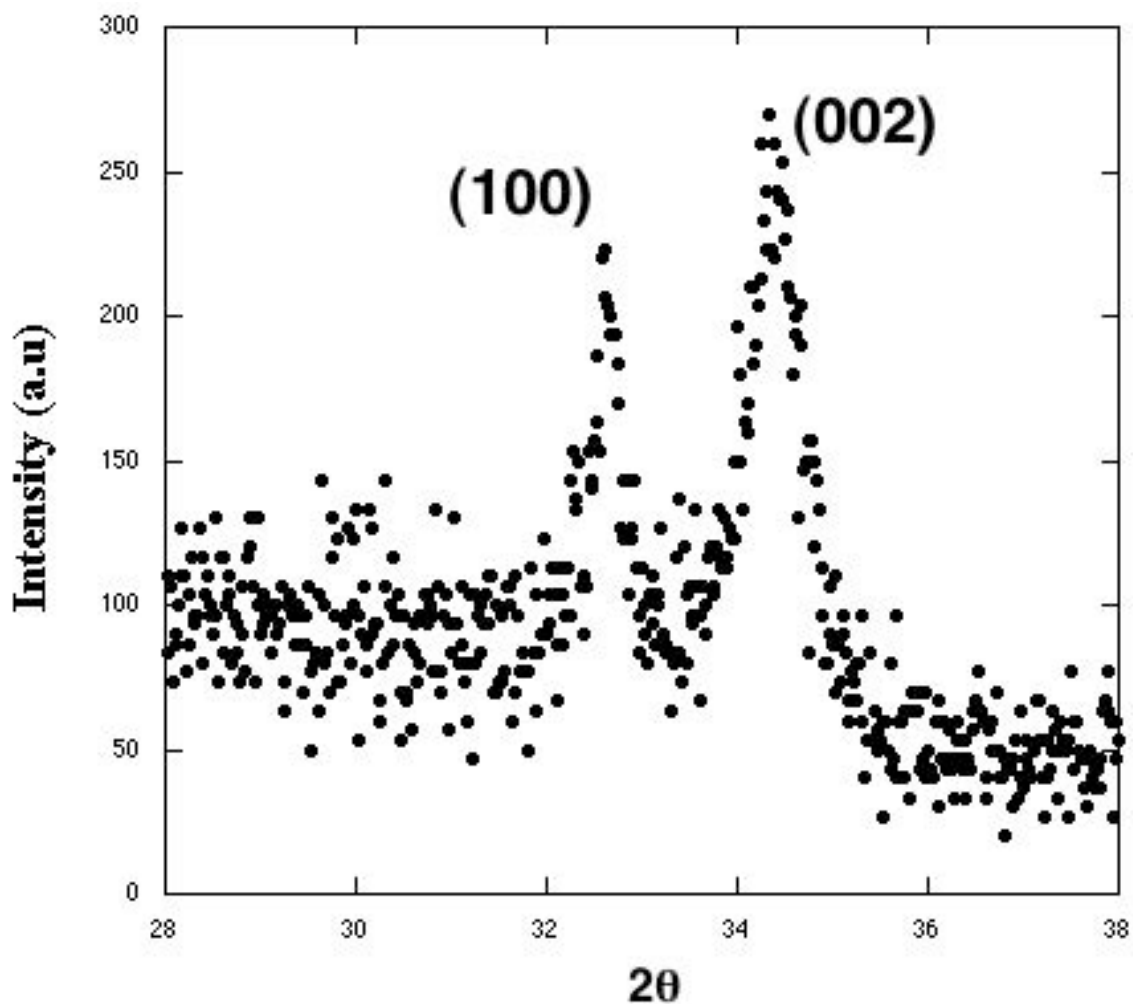
Figure 5.9 XRD (θ-2θ) pattern of 500-cycle ALD ZnO grown at 140 °C on α-Al₂O₃(0001).

Figure 5.9 illustrates the radial scan (θ-2θ) along the normal to the surface of the ZnO films. XRD revealed both (002) and (100) grains of hexagonal wurtzite structure present

in the ZnO thin films. The ZnO thin films are polycrystalline and oriented in both (002) and (100) crystallographic planes.

5.4 Growth of ALD ZnO film on nonpolar oxidized Si surfaces

We have also grown ALD ZnO over oxidized Si (100) wafers. These surfaces are expected to be amorphous. The substrates were cleaned in acetone and methanol before loading into the ALD reactor. The ZnO thin films were grown at 145 °C with 2-5-2-5 s ALD cycle times.

5.4.1 Surface morphology of ALD ZnO films on oxidized Si surfaces

AFM was performed on 300-cycle ALD ZnO films. Figure 5.10 shows the AFM image of one such surface. RMS roughness was found to be 1.5 nm.

Figure 5.10 Height image of AFM scan (1x1 μm^2) of 300-cycle ALD ZnO films grown on oxidized Si(100) at 145 °C.

5.4.2 XRD studies of ALD ZnO films on oxidized Si(100) surfaces

XRD was performed on a 1000-cycle ALD ZnO film grown on an oxidized Si(100) surface at 145 °C. Figure 5.11 illustrates the radial scan (θ-2θ) along the normal to the surface of the ZnO film on oxidized Si(100).
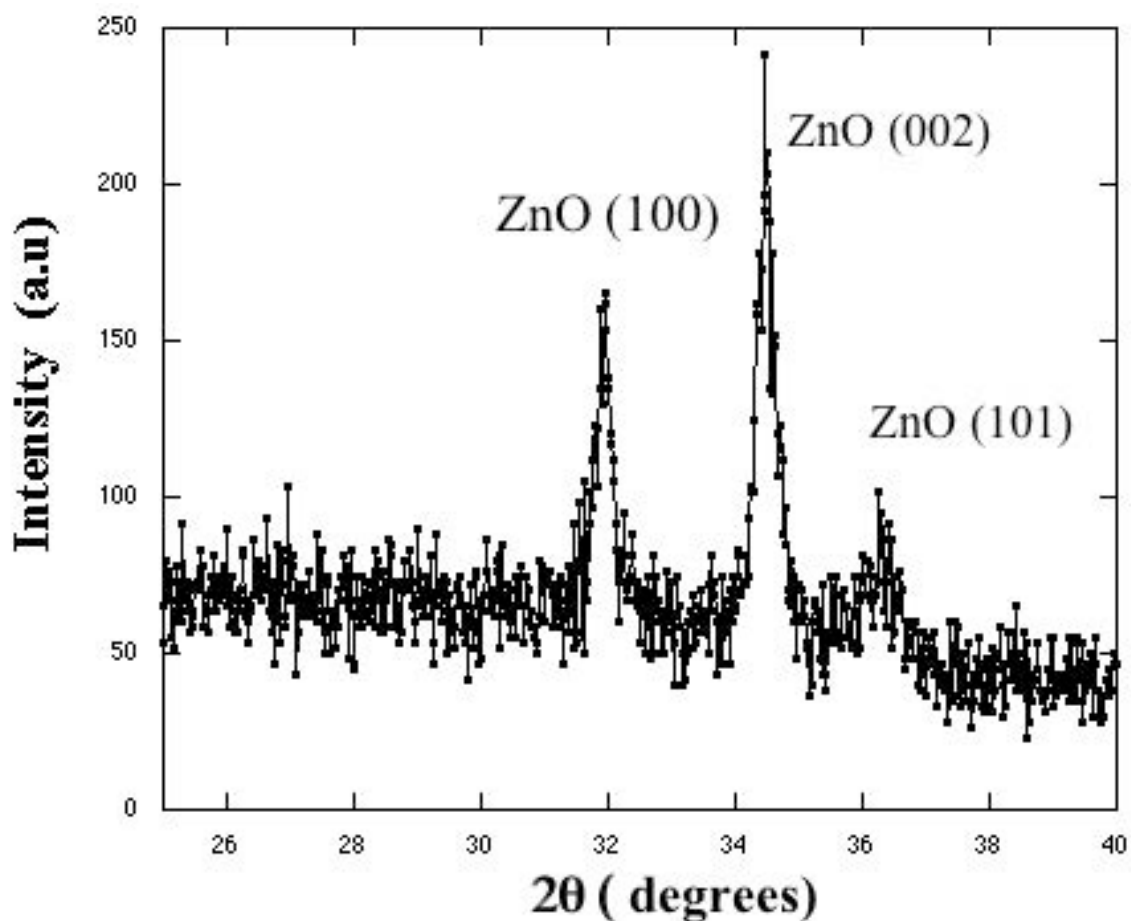
Figure 5.11 XRD (θ-2θ) pattern of 1000-cycle ALD ZnO grown at 145 °C on oxidized Si(100).

The XRD pattern shows that the ZnO thin films are polycrystalline, having wurtzite structure. It has preferential growth along *c*-axis., but also shows substantial growth in other directions. The relative peak intensity of (002) peak [$I_{002}/(I_{001}+I_{002}+I_{101})$] is 0.49, whereas the relative peak intensities of (100) and (101) peaks are 0.32 and 0.19 respectively.

5.5 Growth of ALD ZnO film on polar 6H-SiC(0001) surfaces

We have also grown ALD ZnO films on 6H-SiC(0001) surfaces using DEZ and water at 140 °C. The 5 mm x 5 mm x 0.5 mm 6H-SiC(0001) single-side-polished samples from MTI Inc. with purity 99.99 %, were cleaned sonically with acetone and methanol, as described for MgO(100). After cleaning, the sample was loaded in the ALD reactor. 500-cycle ALD ZnO thin films were grown on 6H-SiC(0001) at 140 °C. The ALD cycle time 3-5-3-5 s was employed during the growth.

5.5.1 Surface morphology of ALD ZnO films on 6H-SiC(0001) surfaces

AFM was performed on 500-cycle ALD ZnO films. Figure 5.12 shows the AFM image of one such surface. RMS roughness was found to be as low as 1.1 nm. As-received 6H-SiC substrates have RMS roughness ~ 5 nm.

a

b
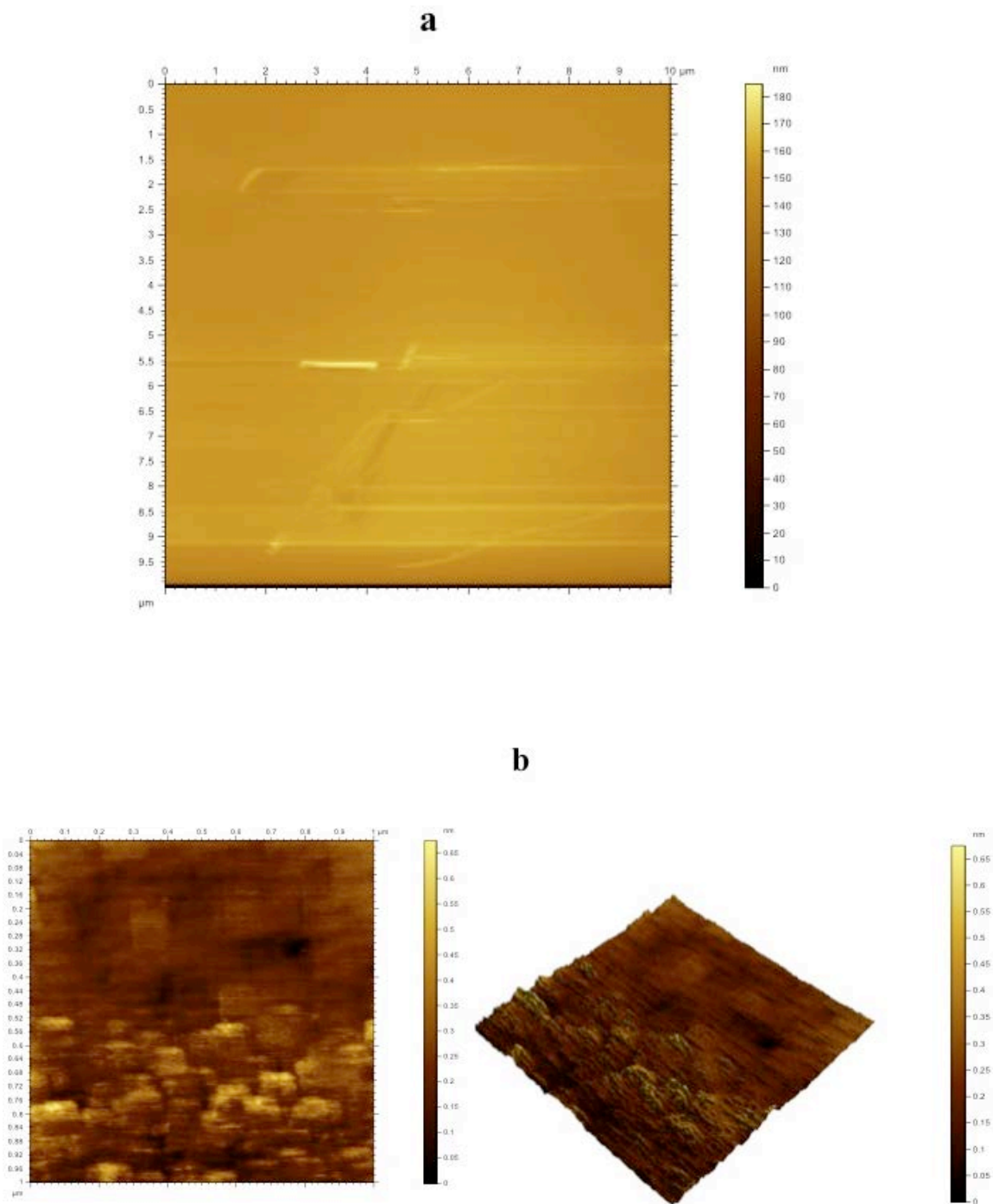
Figure 5.12 Height image of AFM scan (a) As received (10x10 μm^2) (b) 500-cycle ALD

ZnO films grown on 6H-SiC(0001) at 150 °C (1x1 μm^2).

5.5.2 XRD studies of ALD ZnO films on 6H-SiC (0001) surfaces

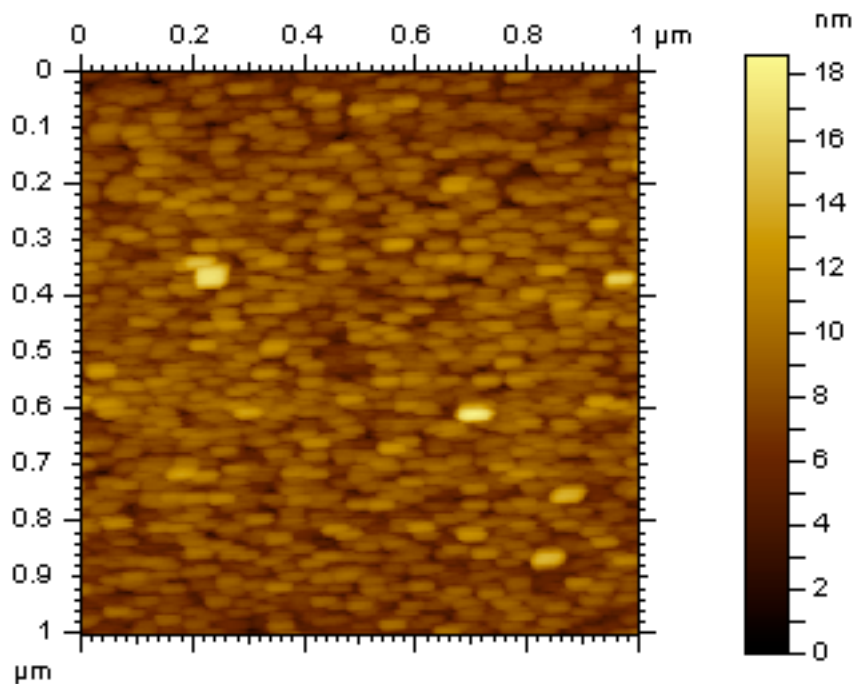XRD was performed on 500 cycle ALD ZnO film grown on 6H-SiC surfaces at 140 °C. Figure 5.13 shows the radial scan (θ-2θ) along the normal of the surface of ZnO. Only the ZnO (002) plane of the hexagonal wurtzite structure was observed in the XRD pattern. This implies that the ZnO films were grown only along the *c*-axis on 6H-SiC substrates with wurtzite structure. We believe the small lattice mismatch is the reason for such a growth even at this low growth temperature.
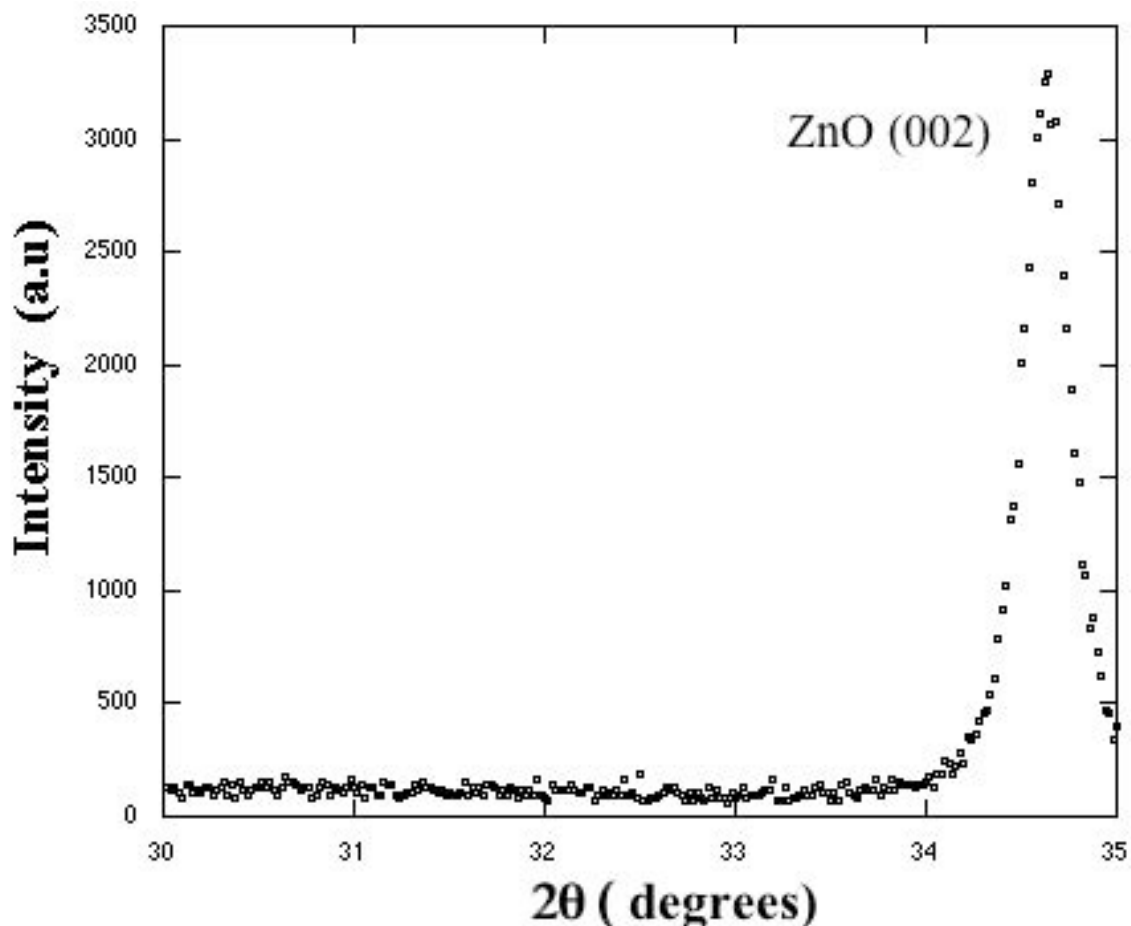
Figure 5.13 XRD (θ-2θ) pattern of 500 cycles ALD ZnO grown at 140 °C over 6H-SiC(0001).

5.6 Conclusions

We have grown ALD ZnO on non-polar MgO(100), α-Al$_2$O$_3$, and oxidized Si(100) surfaces. The ZnO grows with wurtzite structure with preferential growth along *c*-axis. However a small growth along (100) direction is also observed for non-polar MgO(100) and α-Al$_2$O$_3$. In the case of oxidized Si(100), growth along both (101) and (100) direction are observed along with (002) direction. When small lattice mismatched 6H-SiC(0001) substrates were used to grow ALD ZnO, highly *c*-axis oriented ZnO films were obtained. From the results we conclude, that lattice matched substrates are essential for epitaxial ALD ZnO growth.

5.7 References

1. X. H. Wei, Y. R. Li, J. Zhu, W. Huang, Y. Zhang, W. B. Luo, and H. Ji, Appl. Phys. Lett. **90**, 151918 (20027).

2. C. Y. J. Lu, L. Chang, K. H. Ploog, and M. M. C. Chou, J. Cryst. Growth (2013). (Accepted for publication, vol. and page no. still not available)

3. F. K. Shan, G. X. Liu, W. J. Lee & B.C. Shin, Integrated Ferroelectrics: An International Journal, **78:1**, 181 (2006).

4. M. Peres, S. Magalhães, M. R. Soares, M. J. Soares, L. Rino, E. Alves, K. Lorenz, M. R. Correia, A. C. Lourenco, and T. Monteiro, Phys. Status Solidi C **10**, 662 (2013).

5. < www.netmarkscom.com/crystalsystems>

6. M. Khalid, M. Ziese, A. Setzer, P. Esquinazi, M. Lorenz, H. Hochmuth, M. Grundmann, D. Spemann, T. Butz, G. Brauer, W. Anwand, G. Fischer, W. A. Adeagbo, W. Hergert, and A. Ernst, Phys. Rev. B **80**, 035331 (2009).

7. J. Y. Park, J. H. Je, S. S. Kim, J. Cryst. Growth **312**, 3588 (2010).

8. A. Bakin , J. Kioseoglou , B. Pecz , A. E. Shaer , A. C. Mofor , J. Stoemenos , and A. Waag, J. Cryst. Growth **308**, 314 (2007).

9. B. Pecz, A. E. Shaer, A. Bakin, A. C. Mofor, A. Waag, and J. Stoemenos, J. Appl. Phys. **100**, 103506 (2006).

10. X. Q. Wang, H. P. Sun, and X. Q. Pan, Appl. Phys. Lett. **97**, 151908 (2010).

11. Y. Chen, H. J. Ko, S. K. Hong, and T. Yao, Appl. Phys. Lett. **76**, 559 (2000).

12. K. Kim, K. Sun, and S. Lee, Journal of Ceramic Processing Research. **13**, s294 (2012).

13. S. Yang, C. C. Kuo, W. R. Liu, B. H. Lin, H. C. Hsu, C. H. Hsu, and W. F. Hsieh, Appl. Phys. Lett **100**, 101907 (2012).

14. K. Liu, K. Yen, P. Lin, and J. Gonga, K. Wu, and W. Chen, J. Vac. Sci. Technol. A **29**, 03A101 (2011).

15. Y. Lin, P. Chung, H. Lai, H. Su, D. Lyu, K. Yen, T. Lin, C. Kung, and J. Gong, Appl. Surf. Sci. **256**, 819 (2009).

16. P. Guenard, G. Renaud, A. Barbier, and M. Gautier-Soyer, Surf. Rev. Lett. **5**, 321 (1998).

17. C. C. Chang, J. Appl. Phys. **39**, 5570 (1968).

18. M. Gautier, L. PhamVan, M. J. Guittet, and J. P. Duraud, Surf. Sci. **250**, 71 (1991).

19. M. Gautier, G. Renaud, L. Pham Van, B. Villette, M. Pollak, N. Thromat, F. Jollet,

and J. P. Duraud, J. Am. Ceram. Soc. **77,** 323 (1994).

20. P. J. Eng, T. P. Trainor, G. E. Brown, G. A. Waychunas, M. Newville, S. R. Sutton, M. L. Rivers, Science **288**, 1029 (2000).

21. P. J. Fisher, Luxmi, N. Srivastava, S. Nie, and R. M. Feenstra, J. Vac. Sci. Technol. A **28**, 958 (2010).

22. A. Coati, M. Sauvage-Simkin, Y. Garreau, R. Pinchaux, T. Argunova, K. A˙id, Phys. Rev. B **59**, 12224 (1999).

23. < www.nanoclub.tw>

24. M. C. Lin, M. K. Wu, K. Y. Yuan, M. J. Chen, J. R Yang, and M. Shiojirib, J. Electrochem. Soc. **158**, H1213 (2011).

25. K. P. Liu, K. Y. Yen, P. Y. Lin, and J. R. K. Wu, and W. L Chen, J. Vac. Sci. Technol. A **29**, 03A101 (2011).

26 T. Urano, T. Kanaji, and M. Kaburagi, Surf. Sci. **134**, 109 (1983).

Chapter 6

Growth of ZnO thin films on polar (√3×√3)R30° reconstructed and unreconstructed MgO(111) surfaces by pulsed-laser deposition

Abstract

This chapter outlines growth of ZnO thin films on polar (√3×√3)R30° reconstructed and unreconstructed MgO(111)-(1x1) surfaces using pulsed laser deposition. Surface morphology studies using AFM and structure studies using XRD are discussed.

6.1 Introduction

In Chapter 4, the growth of ZnO on polar $(\sqrt{3}\times\sqrt{3})R30°$ reconstructed and unreconstructed MgO(111) surfaces using ALD was discussed in detail. In this chapter, I discuss the growth of ZnO on polar $(\sqrt{3}\times\sqrt{3})R30°$ reconstructed and unreconstructed MgO(111) surfaces, using pulsed laser deposition (PLD). We are interested to know if ZnO grows differently on polar MgO(111) surfaces using PLD than it does using ALD. F. Friedrich and co-workers have tried to grow ZnO on unreconstructed MgO(111) and MgO(100) using PLD [1]. They successfully grew high quality *c*-axis oriented ZnO thin films at 800 °C on MgO(111). In contrast, for the MgO(100) surface, both (002) and (101) phases were observed for PLD ZnO thin films.

6.2 Experimental Details

The $(\sqrt{3}\times\sqrt{3})R30°$ reconstructed and unreconstructed MgO(111) surfaces were prepared in the same method as described in Chapter 4. Upon preparation they, were loaded in to a PLD chamber. ZnO thin films of thickness 30 nm were grown simultaneously on both reconstructed and unreconstructed MgO(111) substrates at 10 mTorr oxygen pressure and 550 °C substrate temperature.

6.3 AFM analysis of ZnO films grown on polar MgO(111) substrates by Pulsed-Laser Deposition

The AFM analysis was performed using contact mode to find the surface morphology of ZnO films grown on polar $(\sqrt{3}\times\sqrt{3})R30°$ reconstructed and

unreconstructed MgO(111) surfaces by PLD. Figure 6.1 shows the typical AFM images of 30 nm thick ZnO thin films on unreconstructed MgO(111)-(1x1) substrates. The RMS surface roughness of such surface was ~ 4.3 nm and the average grain size was ~ 80 nm.

a

b
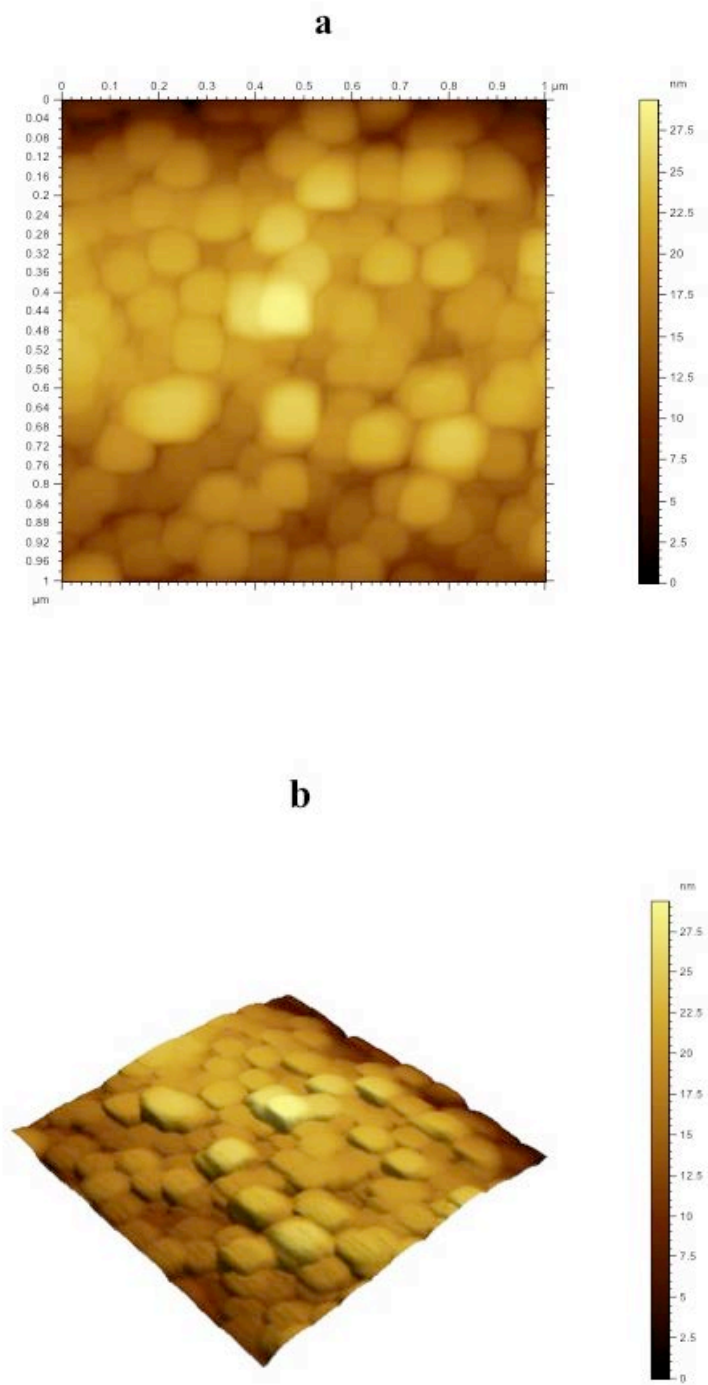
Figure 6.1 (a) Height image (b) three dimensional image of AFM scans (1x1μm^2) of PLD ZnO film of thickness 30 nm on unreconstructed MgO(111) surface.

Figure 6.2 shows the AFM scan of ZnO films of thickness 30 nm over reconstructed MgO(111). The RMS surface roughness was ~ 2.8 nm. The average grain size was ~ 87 nm.
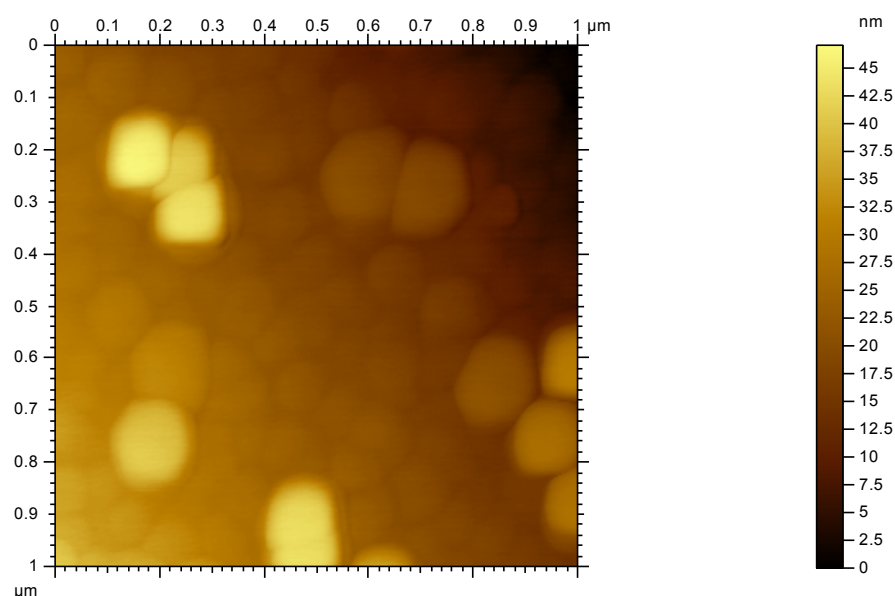
Figure 6.2 Height image of AFM scans (1x1μm^2) of PLD ZnO films of thickness 30 nm on (√3×√3)R30° reconstructed MgO(111) surface.

AFM analysis revealed that ZnO growth on MgO(111) is smoother on the reconstructed surface than on the unreconstructed surface, for the same growth conditions.

6.4 XRD analysis of ZnO films grown on polar MgO(111) substrates by Pulsed-Laser Deposition

Thin-film crystallinity and orientation were assessed with (θ-2θ) radial scan along the normal of the ZnO films.
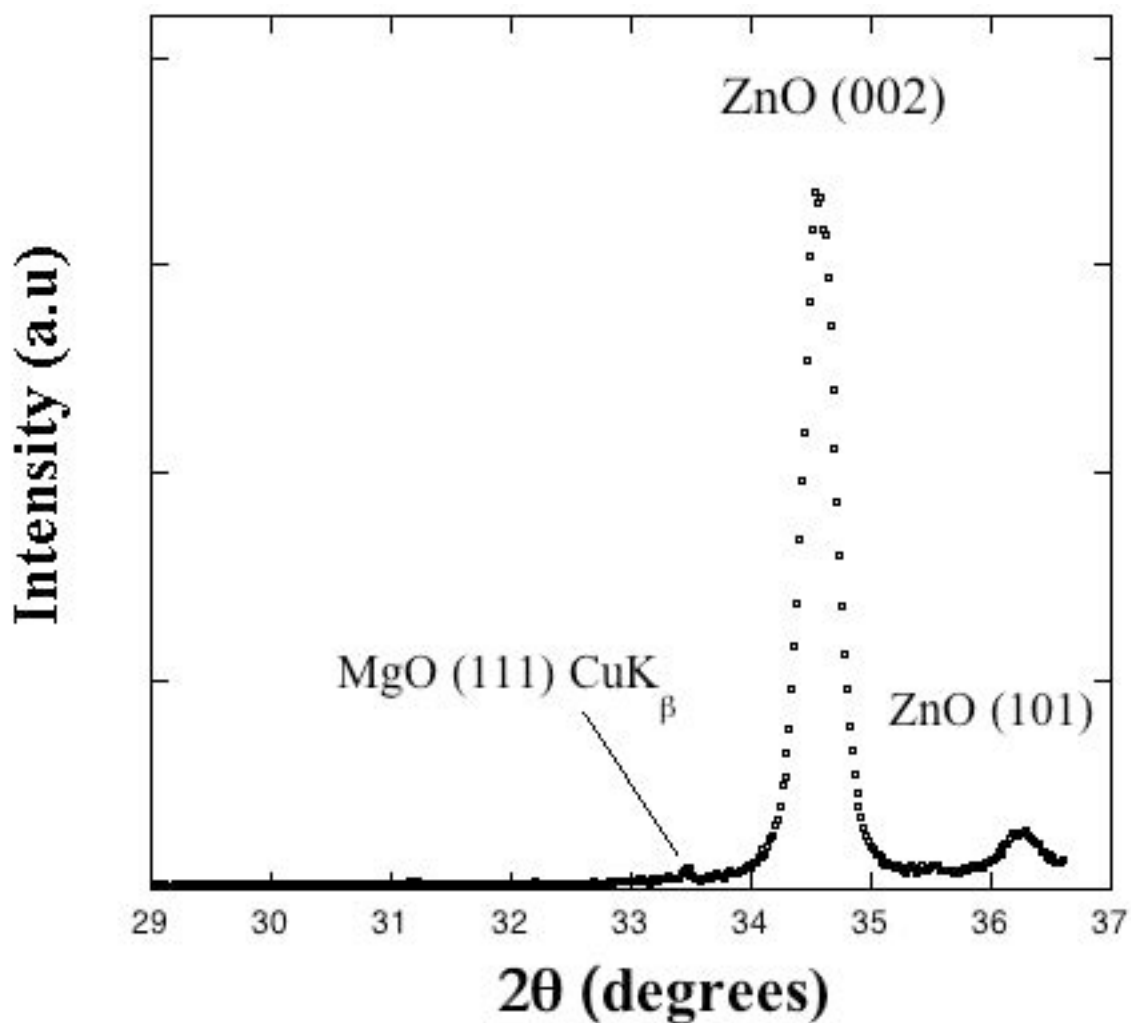
Figure 6.3 XRD (θ-2θ) patterns of PLD ZnO of thickness 30 nm grown at 550 °C on MgO(111)-(1x1).

Figure 6.3 shows the XRD (θ-2θ) patterns of PLD ZnO of thickness 30 nm grown at 550 °C on MgO(111)-(1x1). The XRD characterization reveals that ZnO has very strong

preferred (002) direction. However, a small growth along (101) direction is also observed.
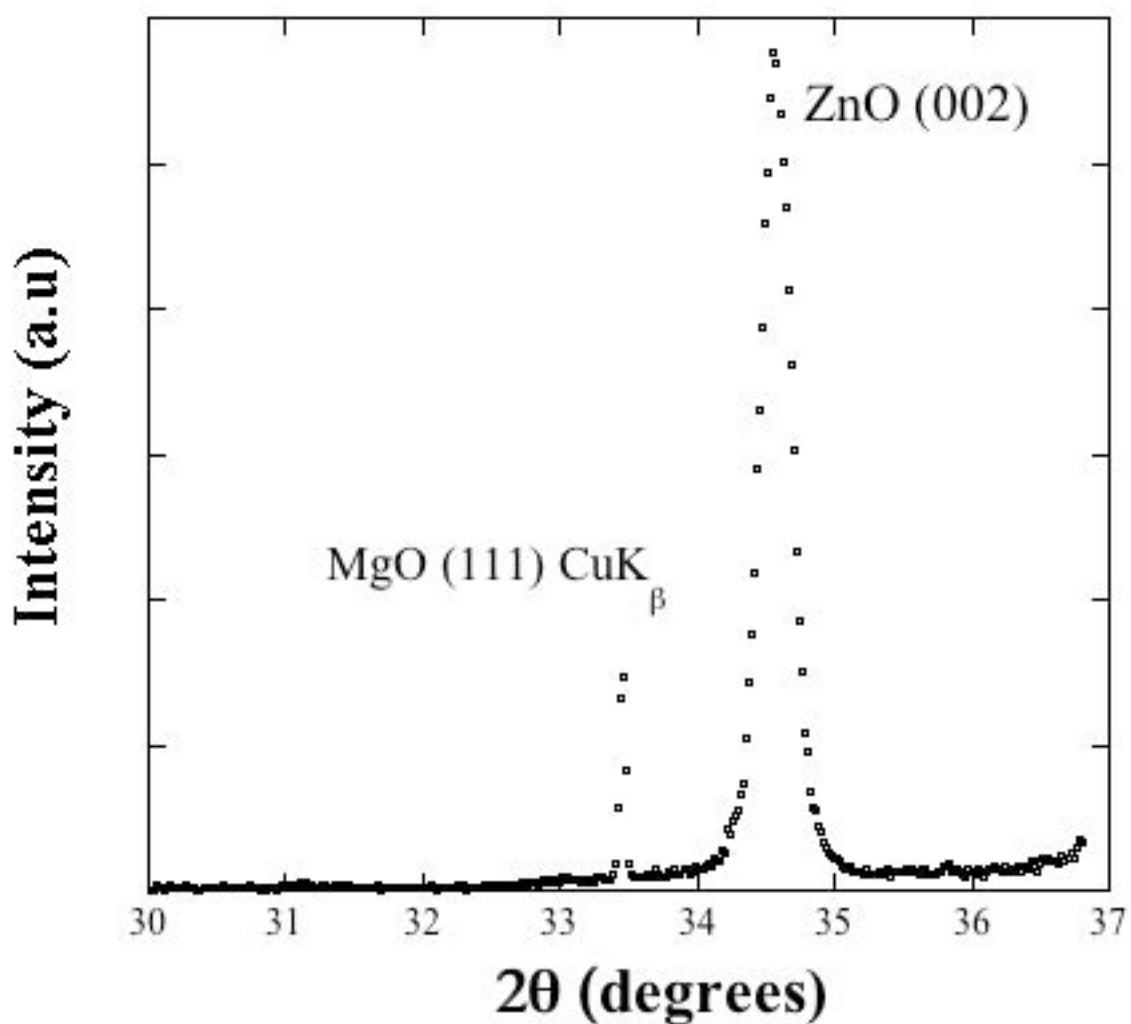
Figure 6.4 XRD (θ-2θ) pattern of PLD ZnO of thickness 30 nm grown at 550 °C on MgO(111)-(√3×√3)R30°.

Figure 6.4 shows the XRD (θ-2θ) pattern of PLD ZnO of thickness 30 nm grown at 550 °C on MgO(111)-(√3×√3)R30°. XRD result showed highly *c*-axis-oriented ZnO (002)

diffraction corresponding to the wurtzite phase. No other diffraction peaks other than (002) were observed.

6.5 Conclusions

ZnO films were grown on polar MgO(111)-($\sqrt{3}\times\sqrt{3}$)R30° and unreconstructed MgO(111)-(1x1) surfaces using PLD. The ZnO films are polycrystalline wurtzite structure and are highly *c*-axis oriented for MgO(111)-($\sqrt{3}\times\sqrt{3}$)R30° substrates. In contrast, for MgO(111)-(1x1) small amounts of the (101) phase were also observed along with the dominant (002) phase for the same growth conditions. This result is very much like ALD ZnO growth on reconstructed and unreconstructed MgO(111) substrates. From this we can conclude that MgO(111)-($\sqrt{3}\times\sqrt{3}$)R30° surfaces are better templates than unreconstructed MgO(111) for epitaxial ZnO growth.

6.6 References

1. F. Friedrich, I. Sieber, M. Klaus, Ch. Genzel, and N. H. Nickel, Phys. Stat. Sol. (c) **5 (10)**, 3288 (2008).

Chapter 7

Conclusions and future outlook

7.1 Conclusions

The dissertation reports design and construction of a novel UHV-interfaced viscous-flow atomic layer deposition reactor with *in-situ* quartz crystal microbalance. Using this viscous-flow ALD reactor we were able to grow ZnO thin films successfully. We studied the ALD ZnO growth using di-ethyl zinc (DEZ) as the zinc precursor and water as the oxygen precursor.

Our in-situ QCM studies revealed an ALD temperature window of 130 to 170 °C where good, self-limiting ZnO growth may take place. In this temperature window the ALD ZnO growth rate was found to be ~ 2.3 Å/cycle. Using in-situ QCM we have observed linear step-like growth, which is consistent with earlier published work. We also observed that almost all the mass is deposited during the DEZ dose in each ALD cycle.

In order to study the growth of ZnO on polar oxide surfaces, we deposited ALD ZnO thin films on polar reconstructed MgO(111)-($\sqrt{3}\times\sqrt{3}$)R30° and unreconstructed MgO(111)-(1x1) surfaces. These films were characterized using x-ray diffraction (XRD), atomic force microscope (AFM), x-ray photoelectron spectroscopy (XPS), and UV-visible spectroscopy.

The XRD study revealed that the ALD ZnO films grow polycrystalline, in the hexagonal wurtzite structure with highly *c*-axis-oriented growth for polar MgO(111)-($\sqrt{3}\times\sqrt{3}$)R30° reconstructed substrates. In contrast, for polar unreconstructed MgO(111)-(1x1) substrates, (101) and (100) phases were also present along with the dominant (002) phase for same growth conditions. The AFM measurements revealed that ZnO films on reconstructed MgO(111)-($\sqrt{3}\times\sqrt{3}$)R30° are smoother than those on unreconstructed MgO(111)-(1x1). AFM results also suggested formation of polycrystalline ZnO films is accompanied by surface roughening which increases with increasing film thickness. At higher growth temperatures, the ZnO thin film roughness is considerably less compared to lower growth temperatures. XPS measurements indicate that thicker films (> 1200 Å) are stoichiometric. UV-visible spectroscopy was used to find the bandgap of 3.2 eV and sharp ultraviolet cutoff of 380 nm for ALD-grown ZnO thin films. The optical transmission was found to be more than 80% in the visible region.

In the second part of the investigation, we have used non-polar substrates of MgO(100), oxidized Si(100), α-Al$_2$O$_3$(0001) and polar 6H-SiC substrates which have a small lattice mismatch with ZnO to grow ALD ZnO films at similar growth conditions. We have examined the thin-film crystallinity of ALD-grown ZnO films on these substrates using XRD and surface morphology using AFM.

The ALD ZnO films on non-polar MgO and α-Al$_2$O$_3$(0001) are polycrystalline, having the wurtzite structure, with (002) and (100) orientation. In contrast, on oxidized Si(100), the (101) phase was also observed along with (002) and (100) orientation. However, for polar 6H-SiC substrates we were able to grow highly *c*-axis oriented wurtzite ZnO thin films of good quality.

Finally we have grown ZnO thin films on polar reconstructed MgO(111)-($\sqrt{3}\times\sqrt{3}$)R30° and unreconstructed MgO(111)-(1x1) surfaces using PLD to investigate the growth of ZnO on polar substrates using growth techniques other than ALD. PLD-grown ZnO thin films were characterized using XRD and AFM.

Our XRD studies revealed results very similar to that observed in case of ALD ZnO thin films on polar reconstructed MgO(111)-($\sqrt{3}\times\sqrt{3}$)R30° and unreconstructed MgO(111)-(1x1) surfaces. PLD ZnO thin films on polar reconstructed MgO(111)-($\sqrt{3}\times\sqrt{3}$)R30° were highly *c*-axis oriented, whereas a (101) phase along with the dominant (002) was also present in case of PLD ZnO films on polar unreconstructed MgO(111)-(1x1) surfaces.

In conclusion, we discovered for the first time that surface reconstruction and surface symmetry plays an important role in growth of ALD ZnO thin films. Also the orientation of the crystallites in the films can be modified using polar or non-polar substrates in ZnO growth using ALD. PLD results suggest strongly that surface reconstruction and initial surface termination have strong effects on the crystallinilty of ZnO growth irrespective of the growth technique.

7.2 Future Outlook

The motivation of this work is to grow high quality metastable $Zn_{1-x}Mg_xO$ alloys on MgO or ZnO substrates using ALD for transparent conducting application. This kind of alloy also has the potential to increase solar-cell efficiency and produce Cd-free $Cu(In,Ga)Se_2$ solar cells by replacing the CdS buffer layer in $Cu(In,Ga)Se_2$ (CIGS) solar cells [1]. There is large interest in $Zn_{1-x}Mg_xO$ alloys and multilayers for UV-light

emitting diode applications [2]. PLD, and MBE methods are widely used to grow such materials. Using MBE, Koike and co-workers were able to produce single-phase wurtzite films of $Zn_{1-x}Mg_xO$ alloys with bandgap 4.1 eV on sapphire [3]. However, ALD has gained more interest in the industry because it offers the advantage of low growth temperature, and conformal and large-area deposition of uniform thin films. Investigation of making $Zn_{1-x}Mg_xO$ alloys using ALD still in a very early stage [1].

We are in the process of growing ALD MgO using bis(etheylcyclopentadienyl)magnesium $Mg(CpEt)_2$ and water. Once MgO ALD is established, the next logical step will be making multilayers of MgO and ZnO. No electrical measurements were done so far on any of the thin films grown by ALD. The effect of growth parameters, such as temperature and purge time, are of interest for optimizing the conductivity of ALD ZnO thin films. Electrical-property measurements, e.g. sheet resistance, using a four-point probe, and carrier concentration, using Hall-probe, are next in the scope of the investigation.

7.3 References

1. C. Platzer-Björkman, T. Törndahl, A. Hultqvist, J. Kessler, and M. Edoff,

Thin Solid Films, **515**, 6024 (2007).

2. U. Ozgur, Y. I. Alivov, C. Liu, A. Teke, M. A. Reshchikov, S. Dogan, V. Avrutin, S. J. Cho, H. Morkoc, J. Appl. Phys. **98**, 041301 (2005).

3.K. Koike, I. Nakashima, K. Hashimoto, S. Sasa, M. Inoue, M. Yano, Appl. Phys. Lett. **87**, 112106, (2005).

CURRICULAM VITAE

Kallol Pradhan

Education

2013	PhD, Physics
	University of Wisconsin- Milwaukee
2004	M.Sc., Physics
	Indian Institute of Technology (IIT)-Guwahati, India
2001	B.Sc., Physics (Honors), Chemistry, Mathematics
	University of Calcutta, India

Awards and Scholarships

David Lichtman Scholarship 2012, Physics Department, UWM

Chancellors Fellowship Award, UWM 2005-12,

Electrochemical Society (ECS) Travel award, 2011

Graduate Student Travel Award, UWM, 2011

AVS Hoffman Travel Award 2008

Indian Oil Corporation Meritorious Student Award 2004

Teaching Experience

2005-2013	University of Wisconsin-Milwaukee, Department of Physics
	Courses:
	Fall 2005 Physics 215 Calculus Lab Physics II
	Spring 2006 Physics 215 Calculus Lab Physics II
	Fall 2007 Physics 214 Calculus Lab Physics I

Spring 2008   Physics 214 Calculus Lab Physics I

Fall 2009   Physics 209 Calculus Physics I

Fall 2012   Physics 123 General Physics Lab II

Spring 2013   Physics 123 General Physics Lab II

Research Experience

2006-2013	Physics Department, University of Wisconsin-Milwaukee
	Advisor: Prof. Paul F. Lyman
2004-2005	Quantum Optics and Information Division, Physical Research Laboratory-India
	Advisor: Prof. Prasanta K. Panigrahi

Publications

"Parametrically controlling solitary wave dynamics in the modified Korteweg-de Vries equation" K. Pradhan and Prasanta K. Panigrahi, J. Phys. A: Math, Gen 39, L343 (2006).

"Observation of a ($\sqrt{3}\times\sqrt{3}$) R30° reconstruction on O-polar ZnO surfaces" S.T.King, S.S.Parihar, K.Pradhan, H.T. Johnson-Steigelman and P.F Lyman, Surf. Sci. Lett. 602, L131(2008).

"Study of atomic layer deposition of ZnO on a polar oxide substrate by in-situ quartz crystal microbalance" K. Pradhan and P. F. Lyman, ECS Trans., Volume 41(2), 247 (2011).

"Growth and structure of ZnO thin films on polar ($\sqrt{3}\times\sqrt{3}$) R30° reconstructed and unreconstructed MgO(111) surfaces by atomic layer deposition" K. Pradhan and P. F. Lyman, J. Vac. Sci. Technol. A. 31, 021504 (2013).

Presentations

"Growth of ZnO films on Polar MgO(111) surfaces using atomic layer deposition." K. Pradhan (Nottingham Prize contestant) and P.F. Lyman, Physical Electrical Conference, University of Texas Dallas (June 2012)

"Growth and Structure of Atomic Layer Deposition of ZnO on Polar Oxide Surfaces." K. Pradhan and P.F. Lyman, 2011 MRS Fall Meeting and Exhibit, Boston, MA (November 2011)

"Study of atomic layer deposition of ZnO on a polar oxide substrate by in-situ quartz crystal microbalance" K. Pradhan and P. F. Lyman, 220th ECS meeting and Electrochemical Energy Summit, Boston, MA (October 2011)

"Study of atomic layer deposition of ZnO by in-situ quartz crystal microbalance" K. Pradhan and P. F. Lyman, Physical Electronics Conference, UW- Milwaukee, WI (June 2010)

"UHV interfaced viscous flow ALD reactor for production of polar oxide material" K. Pradhan and P. F. Lyman, 9th International Conference on Atomic Layer Deposition, Monterey CA (July 2009)

"Integrated UHV/ALD reactor for growth of oxide material" K. Pradhan, A.E.Wierzbinski and P.F.Lyman, AVS 55th International Symposium & Exhibition, Boston, MA (October 2008)

"Viscous flow atomic layer deposition (ALD) reactor for production of polar oxide hetrostructure" K. Pradhan and P.F.Lyman, Laboratory of Surface Studies, Summer Symposium, UW-Milwaukee, WI (August 2008)